Chromospheric and coronal activity in solar-like stars

Dissertation
zur Erlangung des Doktorgrades
des Departments Physik
der Universität Hamburg

vorgelegt von

Christian Schröder

geboren in Hamburg

Hamburg
2008

Gutachter der Dissertation:	Prof. J.H.M.M. Schmitt Dr. Ansgar Reiners
Gutachter der Disputation:	Prof. J.H.M.M. Schmitt Prof. P.H. Hauschildt
Datum der Disputation:	18.07.2008
Vorsitzender des Prüfungsausschusses:	Prof. G. Wiedemann
Vorsitzender des Promotionsausschusses:	Prof. J. Bartels
Dekan der Fakultät für Mathematik, Informatik und Naturwissenschaften:	Prof. Dr. Arno Frühwald

Zusammenfassung

Der Begriff ”stellare Aktivität” fasst diverse Phänomene auf der Sternenoberfläche und in der Sternatmosphäre zusammen. Die Ursache für diese Phänomene sind Veränderungen in den Magnetfeldern der Sterne. Während es bei der Sonne möglich ist, die verschiedenen Formen der Aktivität direkt und detailliert zu beobachten, ist dies bei anderen Sternen nicht möglich. Durch eine genaue Analyse der Spektren von Sternen lassen sich dennoch Informationen über deren Aktivität gewinnen.

Die folgende Arbeit befasst sich mit zwei Arten der stellaren Aktivität: zum einen mit der Röntgenaktivität von Sternen des Spektraltyps A und ihrer potentiellen Ursache, zum zweiten mit der chromosphärischen Aktivität von Sternen im Bereich der späten A- bis späten K-Sterne. Da im Bereich der späten A- bis frühen F-Sterne der Dynamo, der für die Aktivität in sonnenähnlichen Sternen verantwortlich ist, entsteht, ist dieser Spektralbereich für das Verständnis der stellaren Aktivität von besonderer Bedeutung.

Zur Untersuchung der Röntgenaktivität von A-Sternen wurde nach Übereinstimmungen zwischen den optischen Positionen der A-Sterne, die im Bright Star Catalogue aufgelistet sind, und den Positionen der in den ROSAT-Katalogen aufgeführten Röntgenquellen gesucht. Als den für eine Korrelation maximal zulässigen Abstand wurden 90 Bodensekunden für die Daten des ROSAT All-Sky Survey festgelegt, sowie 36 Bodensekunden für die gezielten PSPC- Beobachtungen und 18 Bogensekunden für die HRI-Daten. Die sich daraus ergebende Liste von Sternen wurde nach möglichen Anzeichen für bisher unentdeckte, späte Begleitsterne untersucht. Dabei galten Schwankungen in der Radialgeschwindigkeit, der Eigenbewegung und der Lichtkurve der Sterne als Indizien für die Anwesenheit eines unentdeckten Begleiters. Die Korrelation der Kataloge ergab eine Liste von 312 A-Sternen, die mit einer Röntgenquelle assoziiert werden können. 84 dieser Sterne sind Einzel- oder räumlich aufgelöste Doppelsterne.

In einem weiteren Schritt wurden 13 der röntgenaktiven A-Sterne auf mögliche Magnetfelder untersucht. Dazu wurden die Spektren dieser Sterne auf die Anwesenheit von Merkmalen zirkularer Polarisation im Bereich der Balmerlinien des Wasserstoffs und in Kalziumlinien untersucht. Durch die Anwesenheit der nach Pieter Zeeman benannten Merkmale lässt sich die Stärke des longitudinalen Anteils des über die Sternoberfläche gemittelten Magnetfeldes messen. Die Beobachtungen ergaben für drei Sterne sichere Detektionen und bei neun weiteren Sternen mögliche Hinweise auf schwache Magnetfelder. Bei den Sternen mit sicherer Detektion wurde überprüft, ob die Röntgenhelligkeit mit den Vorhersagen des *magnetically confined wind shock models* übereinstimmt. Ein Zusammenhang zwischen der beobachteten Röntgenhelligkeit und der Stärke der Magnetfelder wurde nicht gefunden.

Die chromosphärische Aktivität von 481 späten A- bis zu späten K-Sternen wurde auf zwei Arten gemessen. Zum einen mit Hilfe der klassischen Mount-Wilson-Methode, die jedoch nur für langsam rotierende Sterne mit dem Farbindex B-V im Bereich von 0.44 bis 0.9 geeignet ist, zum anderen mit einer neu entwickelten Methode, die auch für schnell rotierende Sterne und für Sterne mit B-V < 0.44 geeignet ist. Bei dieser neuen Methode wird der zu vermessende Stern mit einem inaktiven Stern verglichen. Dazu muss dieser auf die Rotationsgeschwindigkeit des zu vermessenden Sterns und die damit verbundene Rotationsverbreiterung angepasst werden. Eine Analyse der Auswirkungen der Rotationsverbreiterung zeigt, dass bei schnell rotierenden, inaktiven Sternen die verbreiterten Linienflügel der Kalziumlinie die Messungen der klassischen Methode verfälschen, während die Ergebnisse der neuen Methode unbeeinflusst bleiben. Für langsam rotierende Sterne sind die Ergebnisse der neuen Methode mit denen der klassischen Mount-Wilson-Methode vergleichbar und erlauben die Beobachtung des Einsetzens der chromosphärischen Aktivität im Bereich der späten A- bis frühen F-Sterne.

Abstract

The term “stellar activity” summarizes a number of phenomena on the stellar surface and in the stellar atmosphere. The origin of many of these phenomena are changes in the structure of the stellar magnetic field. While it is possible to directly observe different forms of activity on the Sun in great detail, this remains impossible for other stars. However, by analyzing the spectra of these stars, information about their activity can be obtained.

This thesis addresses two aspects of activity: First, the X-ray emission from the positions of A-type stars and a possible mechanism to produce these X-rays and second, the chromospheric activity in the spectral range from late A- to late K-type stars. Since the dynamo, which is responsible for the activity of solar-like stars, emerges in the range of late A- to early F-type stars, this spectral range is of special interest for the understanding of the activity phenomena.

To study the X-ray activity of A-type stars, their optical positions as given in the Bright Star Catalogue were compared with the positions of the X-ray sources listed in the ROSAT catalogs. The matching criteria for the ROSAT All-Sky Survey data were 90 arcseconds, 36 arcseconds for the pointing observations with the PSPC and 18 arcseconds for HRI data. Those stars which could be associated with X-ray sources were tested for indications of hidden late-type companions. Variations in the radial velocity, the proper motion, and the light curve were interpreted as signs for binarity. The correlation of the catalogs yielded 312 stars with an associated X-ray source, of which 84 are bona fide single or resolved binary stars.

In a second step, 13 of the X-ray emitting A-type stars were observed in the optical to search for magnetic fields. To detect and quantify the magnetic fields, the spectra of the stars were searched for Zeeman features in the hydrogen Balmer and calcium lines, which are indicators for circular polarization. The analysis of the Zeeman features allows the determination of the strengths of the longitudinal field averaged over the whole stellar disk. In three out of 13 cases the observations revealed magnetic fields at a 3 σ significance level. Indications for weak magnetic fields were found in nine additional stars. For the three stars with certain detections the X-ray luminosity was compared to the predictions of the magnetically confined wind-shock model. A direct correlation between the magnetic field strength and the X-ray luminosity was not found.

The chromospheric activity of 481 late A- to late K-type stars was measured with two methods. First, with the classical Mount Wilson method, which can be applied to slowly rotating main-sequence stars in the range from $0.44 < B-V < 0.9$ and second with a new template method. This new method allows to measure the chromospheric activity in rapidly rotating stars and stars with $B - V < 0.44$. To determine the activity level of a star applying the new technique, one compares the spectrum of the target star with the spectrum of a slowly rotating inactive star. To fit the template spectrum to the spectrum of the stars, it has to be artificially broadened according to the rotational velocity of the target star. A study of the effects of the rotational broadening showed a strong influence on the classical measurement for rapidly rotating inactive stars, while the new template method is unaffected by rotational broadening. The results of the new method are consistent with those of the classical method and allow to observe the onset of the chromospheric activity in the late A- to early F-type stars.

Contents

Chapter 1

Introduction

Stellar activity describes a large variety of atmospheric phenomena in the atmosphere of stars. Signs of activity can be found on the Sun and almost all stars with a surface temperature of less than 7500 K down to the borderline between stars and brown dwarfs at around 2000 K. Indicators for activity are for example spots, prominences, X-ray flares, mottles and spiculae. Spatially resolved observations of many of these activity phenomena require special observational efforts or are only possible for the Sun. Therefore, the knowledge about the existence of activity in other stars than the Sun is based on detailed studies of the light emitted by the whole star. These studies include highly sensitive observations of photometric variations and the analysis of spectral features. Even with the great progress made in the observational methods and instrumentation in the last decades, the details of the activity-driving mechanism are only basically understood.

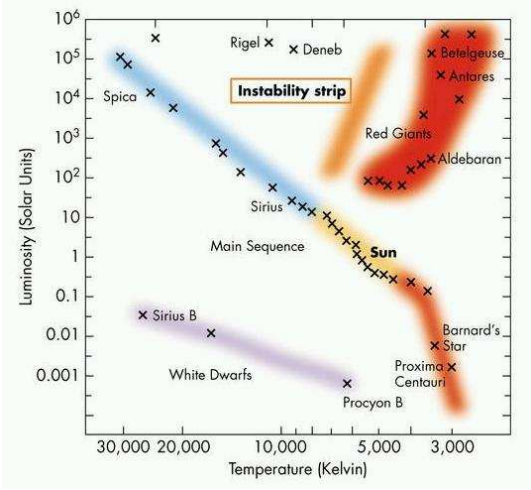

Figure 1.1: The Hertzsprung-Russell diagram shows the temperature-luminosity relation of the different evolutionary stages of stars. (http://www.oswego.edu/kanbur/a100/lecture13.html)

In today's standard of knowledge, all activity phenomena are related to the presence of magnetic fields (Hale 1908; Biermann 1941). Since the magnetic fields are strongly connected to convection, activity can be found only in stars with a substantial outer convection zone. These so-called late-type stars are located in the yellow and brown colored area of the main-sequence in the Hertzsprung-Russel diagram (see Figure 1.1). Their spectral types are called F, G, K, and M, according to their effective temperature. M dwarfs represent the coolest stars on the main-sequence. Cooler objects, which are not able to maintain hydrogen burning, are called L and T dwarfs. If an individual object belongs to the group of stars with hydrogen burning or to the brown dwarfs without a long-term fusion process in their core, is difficult to determine. This is due to the fact that brown dwarfs may appear as late M stars, depending on their age. The hottest of the late-type stars are late A- to early F-type stars. In this spectral range the formation of an outer convection zone begins. Accordingly, the onset of the magnetic activity can be observed in these stars. The most massive stars are the O- and B-type stars, which are located on the left side of the main-sequence in Figure 1.1, with effective temperatures of 30 000 to 60 000 K. These stars posses a convective core and an outer radiative zone.

Stars of the same spectral type may show different levels of activity, based on their age and rotational velocity. Additionally, many stars show cyclic variations over the period of several years, like the Sun's 22 year magnetic cycle (Hale &

Nicholson 1925; Babcock 1961). Accordingly, many different levels of activity can be studied in the different stars, which may help to better understand the activity driving mechanisms. Hence, we are able to study the possible development of the Sun's activity through observations of solar-like stars at different stages of their evolution. Since the solar activity level is believed to influence the climate on Earth, observations of stellar activity are not only of astrophysical interest. Possible impacts on the climate might be caused by high energy particles from the Sun, which could change the heating and cooling of the Earth's atmosphere. Another (still controversial) theory is the modulation of the Earth's cloud cover due to variations of the galactic cosmic ray flux, which are inverse to the variations of the solar activity. There is continuing debate whether the observed global warming is connected to the increase of solar activity over the last decades. A striking coincidence is the fact that the so called Maunder Minimum, which is a phase of strongly decreased activity from 1645 to 1715, is roughly correlated with the 'little ice age' (Eddy 1976). On the other hand, the recent report of the Intergovernmental Panel on Climate Change (IPCC) estimates the impact of the changes in the solar activity of less than 5 %. Better understanding solar and stellar activity phenomena might therefore provide valuable contributions to the understanding of the cause of the climate change.

In this thesis the chromospheric and X-ray activity of late-type stars are studied. The analyses are based on X-ray observations of A-type stars, the search for magnetic fields in those stars and a new method to measure the chromospheric activity in rapidly rotating F to K stars.

1.1 Solar and stellar activity

In the following subsections a brief overview over the different forms of activity on the stellar surface and in the stellar atmosphere is given. Subsection 1.1.1 describes the photosphere, where sunspots are the most prominent signs of activity, followed by an introduction of the chromospheric and coronal activity phenomena in the Subsections 1.1.2 and 1.1.3. A presentation of the current picture of the cause of the activity phenomena, the dynamo theory, is given in Subsection 1.1.4 and followed by an explanation why this model can not be applied to the A-type stars in Subsection 1.1.5. X-ray emission from O- and B-type stars are discussed in Subsection 1.1.6.

1.1.1 Photospheric activity

Among the most prominent activity phenomena connected with solar (and stellar) activity are spots. On the Sun's surface these dark regions were first mentioned by Chinese astronomers, nearly 2000 years ago. Further historic references are a large sunspot at Charlemagne's death in 813 A.D. and a description of sunspot activity by the astronomer John of Worcester in 1129. The nature of these spots, however, was misinterpreted as atmospheric clouds until Galileo found that the spots are on the surface of the Sun in 1612.

We now know that a typical sunspot consists of a central dark region called the umbra, which is surrounded by a slightly brighter region, called the penumbra (see Figure 1.2). The size of the umbra is, depending on the individual sunspot, about the order of 1/100 of the solar radius and the size of the penumbra may reach values of more than 2.5 times the umbral radii. Smaller sunspots without an umbra are called pores. Sunspots are irregular in shape and their contours vary during their evolution. Large sunspots emerge in pairs roughly aligned along solar latitude. Due to their opposing magnetic fields, they are called bipolar spots.

The details about sunspot formation and variation are still subject of research. Their existence and the evolution are directly connected to the evolution of magnetic fields. When the strength of the magnetic field at the borderline between the radiative core and the convective zone reaches a critical value, the magnetic flux tubes are pushed to upper layers of the stellar interior. In the curved flux tubes, the plasma falls back to the deeper regions. This material cannot be replaced with plasma from outside the flux tube, hence the density in the tube decreases. This leads to a buoyancy force on the flux tube, which could rise through the convection zone into the photosphere and beyond. Where the flux tubes penetrate the photosphere, the convection below the surface is suppressed. The absence of convection leads to the cooling of the restrained

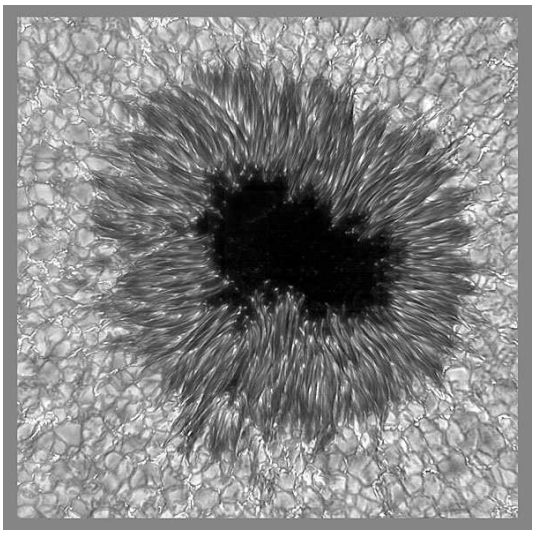

Figure 1.2: High resolution image of a sunspot. Image credit: Friedrich Woeger, KIS, and Chris Berst and Mark Komsa, MSO/AURA/NSF

plasma and creates dark spots on the solar surface (Gough 1990).

For the Sun, the plasma in the sunspots is about 2000 K cooler than for the surrounding photosphere. Measuring the temperature of a *star*spot is a difficult task, owing to the fact that the information about the spot extension and the contrast are merged in surface integrated observations. Further problems are possible contributions of faculae, which are bright spots in the 'canyons' between convection cells emerging on the solar photosphere. Additionally, Doppler shifts of spectral features and the fact that substantial assumptions about the atmospheric conditions of the spot are made, further complicate the temperature measurements. Saar et al. (2001) presented a method using TiO bandheads at 7050 Å and 8860 Å in combination with photometric colors. They found values for the difference between the photosphere and the spot temperature of 600-1900 K for their sample of 11 stars, which is in agreement to the values in sunspots.

Possible techniques to observe the lifetime of starspots are periodic brightness variations (Hall 1991) and Doppler Imaging (Strassmeier et al. 1991). A restriction of these observational methods is that they can only be applied to highly active stars. Because of the need of long-term observations, studies on spot lifetimes are focused on a few well-observed objects. One of these objects is the long period RS CVn binary HR 7275 (K1 IV), with a rotational period of 28.6 days. Strassmeier et al. (1994) found spot lifetimes of several, up to a few dozen rotation periods. Another well studied object is the single star AB Dor (K0V), which possesses a rotation period of 0.51 days. Donati et al. (1999) found that only the polar spot appears to survive for time spans of years, while other spots extending several 10° on the surface persist longer than five days and spots of around 10° size appear and decay on similar timescales.

1.1.2 Chromospheric activity

Sun and solar-like stars

In the 18th and 19th century, when observations of solar eclipses were performed, scientists realized the presence of an extended corona, as well as the red flames today known as prominences and a pink ring of emission at the solar limb, called chromosphere ("color sphere"). These phenomena were confirmed to be of solar rather than terrestrial origin in the mid 1800s, followed by spectroscopic observations during an eclipse in India and Malaysia in 1868. Further studies led to the realization that the spectra of the chromosphere as well as the corona contain numerous emission features of ionized species (Edlén 1945). This led to the conclusion that the temperature in the solar atmosphere rises from about 5700 K in the cooler parts of the photosphere to more than 7000 K in the chromosphere, only to rise to even higher temperatures of more than 1 000 000 K in the corona.

A very simple model of the stellar photosphere is a black body, which emits electro-magnetic radiation according to its temperature. The increase of the temperature in the outer layer of the solar atmosphere contradicts the expected behavior of a black body-like object, which means that the energy transfer from the photosphere to empty space involves a mechanism beyond simple transfer of radiation.

The structure of the chromosphere is not homogeneous. Roberts (1945) first discovered "small spike" prominences, the so-called spicules (see Figure 1.3). These extremely small but

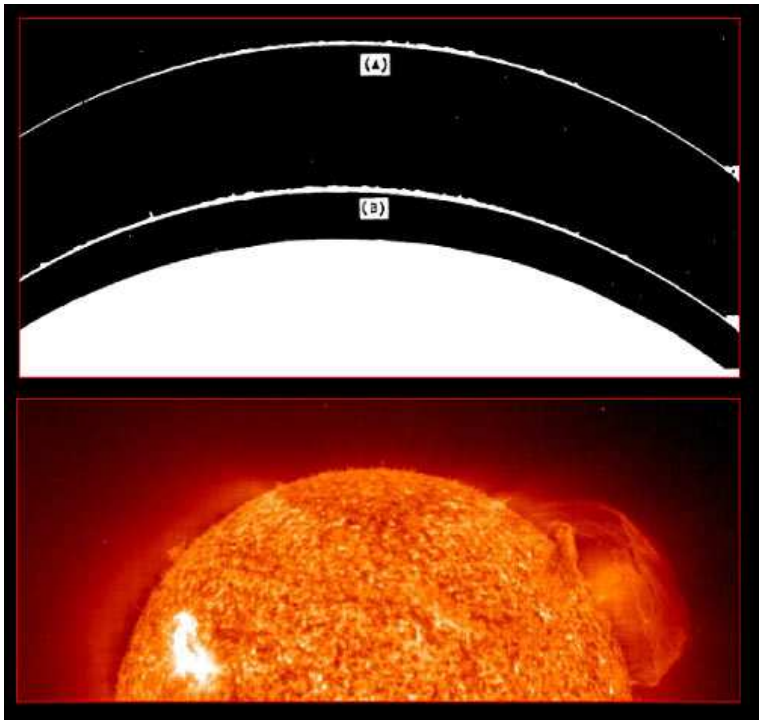

Figure 1.3: Chromospheric spicules observed by Roberts (1945) from images taken eight minutes apart (A and B). On the left side of picture B, two pronounced spicules can be seen. The lower part of the image shows the SOHO observation of the Sun at a wavelengths around 304 Å in the He II. All over the disk, but especially on the limb of the Sun, macrospicules can be seen.

omnipresent features of the chromosphere exist only on short timescales in the order of minutes. 30 years later, Bohlin et al. (1975) discovered a larger version of the spicules, the so-called macrospicules. Both versions are connected to plasma jets flowing through the chromosphere. The bright emission of the spicules in the Hα line at 6563 Å result in the pink color of the chromosphere, while the larger and hotter macrospicules are also bright in the extreme ultraviolet. In contrast to these features of hot gas, the observed CO bands indicate the presence of widespread cool gas in the chromosphere (Solanki et al. 1994). All these phenomena demonstrate that the chromosphere is highly inhomogeneous on temporal and spatial scales.

An early one-dimensional model of the chromosphere is shown in Figure 1.4 (Vernazza et al. 1981). It shows the temperature structure of a semi-empirical model and the formation heights of important lines and continuum areas. In this picture, the chromosphere is roughly defined by the temperature minimum at the height of 500 km and sharp increase of the temperature at 2200 km. This gives a thickness of the chromosphere of around 1700 km, in which the temperature rises from 4000 K to more than 20 000 K. In the transition region the temperature rises sharply, closing the gap to the several million degree in the corona.

The cooling of the plasma takes place when the increase of the temperature from 5000 K to 8000 K releases a large pool of electrons which allows collisional radiative cooling through strong resonance lines. This happens over a relatively wide region, explaining the large extend of the chromospheres of solar-like stars. The lines which play an essential role in the cooling of this region of the stellar atmosphere, like Ca II H&K, Hα and Mg II, are characteristical for the chromosphere. With the exception of the calcium lines at 3933 and 3968 Å, the Hα line and the calcium triplet at $\sim$ 8600 Å, most lines are part of the UV or even shorter wavelength areas

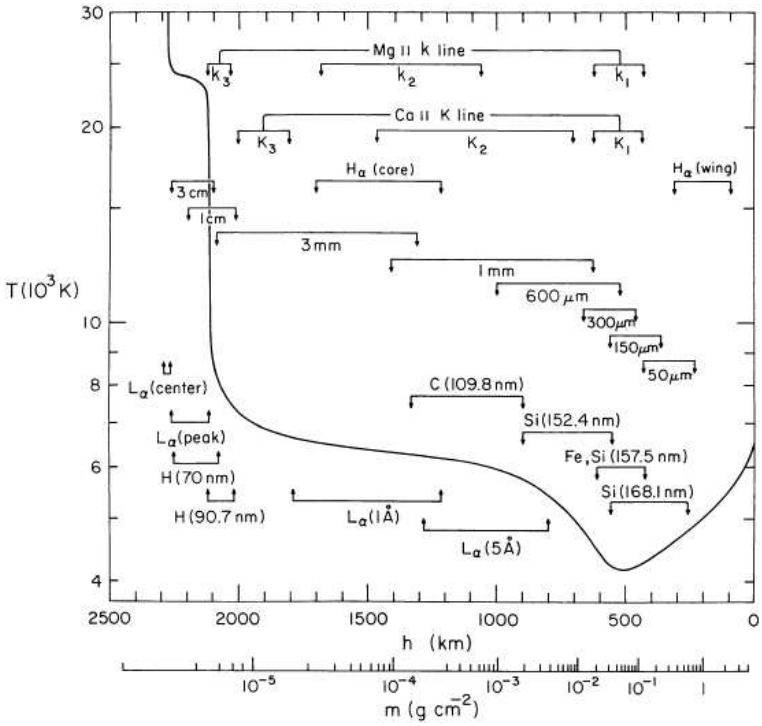

Figure 1.4: The temperature distribution of the average Sun in the range from 0 to 2500 km above the photosphere. The approximate depths of the formation of the lines and continua and their wavelengths are shown in the plot (Vernazza et al. 1981).

of the spectrum and can therefore not be observed from the ground. Once the hydrogen becomes fully ionized, the plasma looses this cooling mechanism and the sharp rise of the temperature visible on the left side of Figure 1.4 takes place.

Chromospheres in hot stars

A problem with chromospheres of hot stars is the fact that heating mechanisms, which are responsible for the temperature increase in the outer atmosphere, are connected with the presence of subsurface convection (see Section 1.1.4). Additionally, the described energy dissipation mechanism applies only to cool F- to M-type stars, in which hydrogen is neutral near the photosphere and is found increasingly ionized only at larger heights. In hot stars, beginning at early F- to late A-type stars, hydrogen is already (partly) ionized in the photosphere. This leaves not enough electrons at larger heights to build an extended chromosphere as can be found at the cool stars. These restrictions lead to the conclusion that solar-like chromospheres are found only on cool stars with subsurface convection layers. Such structures can be found in late A-type stars, beginning around spectral type A7, and over the whole range of cool dwarfs. For the hotter stars, only the evolved giants form outer convection zones, but due to their short lifetime the number of observable objects is quite small.

These more theoretical arguments are strongly supported by observational data. At the hot end of the convection zone limit, Ferrero et al. (1995) presented observations of chromospheric emission in the A7 IV-V star Altair. Further, Simon et al. (2002) concluded from observations of a sample of A-type stars carried out with the Far-Ultraviolet Spectroscopic Explorer (FUSE) that high temperature emission characteristic for coronae and chromospheres, appears for stars with about $T_{\rm eff} < 8250$ K. At these high temperatures, the chromospheres reach only a small extent, due to the increased fraction of ionized hydrogen. The emission of these stars is about a few percent of

the solar values. However, the onset of the emission appears to be abrupt, suggesting an equally abrupt transition from radiative to convective stellar envelopes at an effective temperature in good agreement with the stellar structure models.

Chromospheres in very cool stars

Following the idea that the absence of the solar-like convection zone on the hot end of the solar-like stars results in the disappearance of the chromosphere, a similar disappearance of a chromosphere in the cool dwarf regime seems reasonable. In these stars the transition region, which is an essential part of the solar-like dynamo, disappears due to the fully convective internal structure of the star. Initial observations focused on the dMe stars, which are M stars with the Hα line in emission. In these surveys (Joy & Abt 1974; Giampapa & Liebert 1986) a correlation between Hα emission and the kinematic class, and therefore the statistical age of the star, was found. The fact, that even in fully convective stars an activity-age relationship exists, led to the conclusion that a rotation dependent dynamo is operating in these objects as well. Fleming & Giampapa (1989) performed follow-up observations with a Ca II K survey of M stars, which also suggested the presence of a chromosphere, although with increasingly inefficient non-radiative heating for later spectral types. Even in the very late-type stars, like the M8 dwarf VB10 (Fleming et al. 2003) and an L dwarf binary (Audard et al. 2007), quiescence X-ray emission like in the Sun's quiet corona have been observed with Chandra. Since the presence of a corona is, according to the current state of research, connected to the presence of a chromosphere, these X-ray observations also indicate the existence of a chromosphere in these objects. This indicates the possibility that similar dynamos, which do not depend on the boundary layer between the radiative core and the convection zone, operate in both the Sun and the very low-mass stars, where the principal cycle generating dynamo cannot exist. In recent measurements of magnetic fields in these very late-type stars, Reiners & Basri (2007) found that magnetic fields are present throughout the observed M stars, and that the field strengths are correlated to the rotational velocity. These studies give further indications of the presence of a magnetic dynamo in the coolest stars.

Chromospheres in evolved stars

Another question considering the presence of the chromosphere is the behavior of evolved stars. As described in the previous sections, the presence of a subsurface convection zone is accompanied with chromospheric and coronal activity. Linsky & Haisch (1979) used early IUE observations to show that emission lines like N V, C IV and C II, which are associated with coronae and transition regions, can be found in giant stars in the range of K1 and earlier, but not in the cooler giants. The absence of any emission might be due to cool stellar winds. The dividing line in their data between G and K stars with solar-like chromospheres and M (super)giants with cool chromospheres seemed quite sharp, but studies based on larger samples (Reimers 1982; Judge et al. 1987) revealed the existence of 'hybrid' stars, which possess both strong winds and coronal features. The dividing line can only be found in giants, with all G and K stars with an absolute bolometric magnitude $M_{bol} < -2$ appearing to be X-ray sources (Reimers et al. 1996). Rosner et al. (1995) suggested that the described behavior results from a change in the nature of the dynamo as a star evolves. On the one hand, evolved stars in the solar-like category retain the large-scale dynamo observed in the Sun, leading to a solar-like atmosphere and activity. One example of such an object is HD 81809, which is a binary consisting of two G subgiants. It shows a well-defined 8.2 year activity cycle (Baliunas et al. 1995; Hall et al. 2007). On the other hand, for stars on the other side of the dividing line the activity becomes dominated by small-scale magnetic fields with an open large-scale topology, which allows the formation of strong winds, but prohibits the large, closed magnetic structures associated with transition regions and coronae. The hybrid stars with their large range of activity seem to be in the transition of the two stages. The details of giant star chromospheres and coronae are still poorly understood, but the recent observations make it clear that the magnetic nature that drives the chromospheric activity on the Sun is preserved by stars beyond the end of their main-sequence lives.

As the plethora of chromospheric activity phenomena shows, chromosphere activity measurements are an important tool for the understanding of the mechanisms that influence the solar activity cycle. Further details on measurements of the activity indicators like the Mount Wilson S index and the chromospheric emission ratio $R'_{\rm HK}$ can be found in Section 1.2.4 and Chapter 4.

1.1.3 X-ray activity and the corona

X-ray emission can be found in two groups of stars: first, in the hot O and B stars, in which shocks in the stellar winds produce high temperatures (see Section 1.1.6), and second in late-type stars in the spectral range from F- to M-type stars. In these late-type stars, magnetic fields play an important role in heating the corona up to temperatures of several million degrees. Though the astronomers made great progress in understanding the mechanisms which drive the activity phenomena, the topic of magnetic heating in late-type stars and shocks in hot stars are still subject of the actual research, and their details are not well understood. With respect to the X-ray activity of cool stars, there is a differentiation between two states: the quiescent state and the flare state. The quiescent state describes the permant, more or less constant X-ray emission. Flares, on the other hand, are characterized by a sharp increase in the X-ray brightness of a star and in some cases may include all wavelengths. They are based on the disposal of huge amounts of magnetic energy in small areas of the coronal plasma over a short time. The energy is released when the magnetic field lines change their configuration to a lower energy level due to reconnection (see Section 1.1.4).

Two different forms of flares are known from the Sun:

1. Compact flares are connected to a single magnetic field loop, which may have existed before the flaring event. A compact flare can be triggered through different mechanisms, for example when the plasma is heated through instabilities caused by a strong deformation of the magnetic field.

2. Two-ribbon flares got their name from the ribbon-like, bright structures in the chromosphere, which can be seen in the Hα line. They are formed when a magnetic filament is torn apart and the magnetic field lines reconnect afterwards. Thus, a number of new magnetic field loops are formed. The foot points of these loops are the Hα ribbons. The duration of a two-ribbon flare is longer than the cooling time of the individual magnetic loops, which implies that more energy is transferred into the system during the flare. This leads to the formation of additional superposed loops and the foot points seem to move aside. Due to the energy transfer during the flare and long duration of the event, two-ribbon flares are also called dynamic flares or long-duration events.

The 'typical' X-ray luminosity of a solar flare is about 10^{27} - 10^{29} erg/s, while flares on more active stars than the Sun reach values of 10^{30} - 10^{31} erg/s and more in extreme cases (Schmitt 1997). The temperature in the flaring plasma depends on the strengths of the flare and reaches values of 10 MK and beyond. Flares are short term events, with durations ranging from minutes to hours, while the lifetime of an active region reaches up to months.

Variable magnetic fields which drive the described activity phenomena are related to dynamo processes in the interior of the Sun. The following section gives an introduction of the dynamo theory and the magnetic heating caused by the changes in the magnetic field configuration.

1.1.4 Magnetic heating and stellar dynamo

To reach the high temperatures of the coronae of solar-like stars, which are the cause of the observed coronal X-ray emission, there has to be an effective heating mechanism. This mechanism leaves the surface temperature of the star unaffected, but transfers the energy from the stellar interior to the upper parts of the stellar atmosphere, thus generating temperatures of several million degrees in those areas. One important aspect is the fact, that the energy needed to produce such high temperatures is, compared to the total energy budget of the star, relatively small. The X-ray luminosity of the Sun for

example is only 10^{-6} times the bolometric luminosity. With this small energy emission, the needed heating mechanisms can be weak, which increases the difficulty to differentiate between possible heating mechanisms. In addition to the small total energy, a heating mechanism model should be able to explain the local high-energy processes in the corona, such as flares. Subphotospheric, turbulent convection streams exhibit many times the energy needed to heat the corona. The question is: how is this energy transported from the lower parts of the photosphere to the corona? Also considering other signs of activity, the following phenomena have to be explained by a model:

1. the 11 year cycle of sunspots in combination with the 22 year magnetic cycle.

2. the butterfly diagrams, which describe the movement of the sunspots towards the equator during the activity cycle.

3. the change of polarity of the spots between two spot cycles and the fact that the polarity on one hemisphere is opposite in polarity in the other hemisphere.

4. the reversal of the magnetic field during the minimum of the cycle.

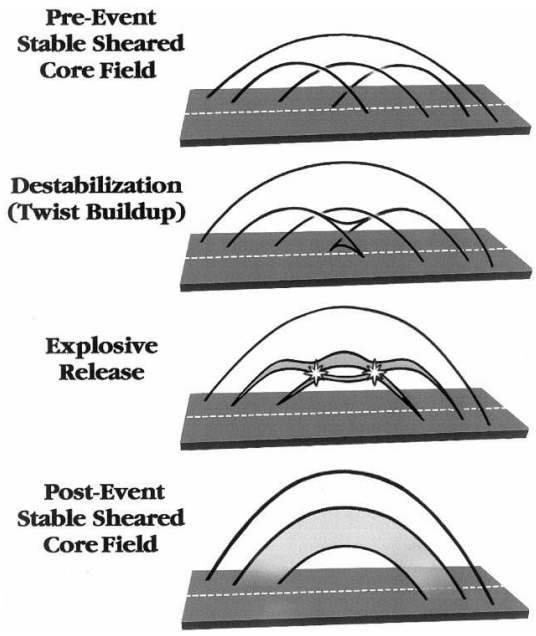

Figure 1.5: Conceptual model of the reconnection of magnetic field lines. The pictures show the disturbance of the stable structures due to the motion of the magnetic foot points. This leads to the storage of energy in the field configuration, which is released when the field lines reconnect (Moore et al. 1999).

Heating mechanisms

For a long time, acoustic waves have been discussed to be responsible for the coronal heating. Longitudinal compression waves form in turbulent motions of the convection zone. The density of the stellar atmosphere decreases with increasing distance to the stellar surface and the amplitude of the waves increases for lower densities. When the amplitude reaches a critical limit, non-linear effects lead to shocks, which deposit their energy in the stellar atmosphere. Since this model is not able to explain the periodic phenomena observed on the Sun's corona, but is able to explain the basal emission of the chromosphere, it is nowadays only used to explain the basal emissions and the heating of the Sun's chromosphere.

Another possible heating mechanism is magnetic heating. The energy source for the magnetic heating processes are the photospheric motions of the foot points of the magnetic field. The relation between the magnetic and atmospheric pressure is described by the plasma parameter $\beta = 8\pi p/B^2$, where B is the magnetic field strength and p the pressure in the surrounding plasma. Since $\beta \gg 1$ at photospheric densities and outside magnetic flux tubes, the field follows the motions of the plasma. In this way, energy is stored in the magnetic field configuration. For the magnetic heating models, there is a differentiation between two mechanisms: the direct current (DC) and the alternating current (AC). Both are based on the fact that the magnetic fields are frozen in the photospheric plasma and that the field follows the movement of the foot points of the coronal fields. In AC mechanisms, the motion of the foot points is too fast for the corona to adapt to the perturbation. This is determined by the Alfvén time $\tau_A = L/v_A$. In such a case the magnetic waves, which formed due to the perturbation of the photospheric field, propagate and dissipate like acoustic waves. The aforesaid condition for the time scale means that the wavelength of the magnetic wave is shorter than the characteristic dimension of the system L.

In DC mechanisms on the other hand, the changes of the system are slow enough to be approximated by a sequence of quasi static states. This means, that the time scale of the perturbation is larger than the Alfvén time τ_A. This scenario involves current sheets on small scales (Parker 1990). A current sheet describes a boundary layer between two plasmas, which is orientated tangential to the magnetic field. The magnetic field has opposing signs on both sides of the sheet. Through the field pressure, the plasma is transported across the field lines into the current sheet, which tries to evade the pressure by pushing the plasma sideways out of the sheet with the speed τ_A. The magnetic flux follows the plasma which leads to a breakup of the magnetic field and a reconnection of the field lines (see Figure 1.5). Since the in- and outflowing components are in equilibrium, the outflowing field is smaller than the inflowing field in the case of sub-alfvénic inflow. This leads to the conversion of the magnetic energy into heat. The reconnection requires magnetic diffusion, which is suppressed under typical stellar conditions. Hence, the process can only be effective on small scales. Shimizu & Tsuneta (1997) proposed, that the energy supply of the corona is indeed based on a huge number of stochastic events, the so-called nano flares (Parker 1988).

The stellar dynamo

An answer to the question, how the variable magnetic fields are generated, which are required for the magnetic heating, is provided by the dynamo theory (Parker 1955). It describes the conversion of a large-scale, static dipole field into a dynamic field by differential rotation. All dynamo theories require either fully convective stars or the presence of an outer convection zone, and are therefore only applicable for late-type stars.

The dynamo effect is based on the fact that the magnetic field lines are frozen in the plasma and therefore follow the motions of the plasma. This follows from the induction equation of magnetohydrodynamics:

$$\frac{\partial \vec{B}}{\partial t} = \vec{\nabla} \times (\vec{v} \times \vec{B}) + \eta \nabla^2 \vec{B} \qquad (1.1)$$

which is equivalent to

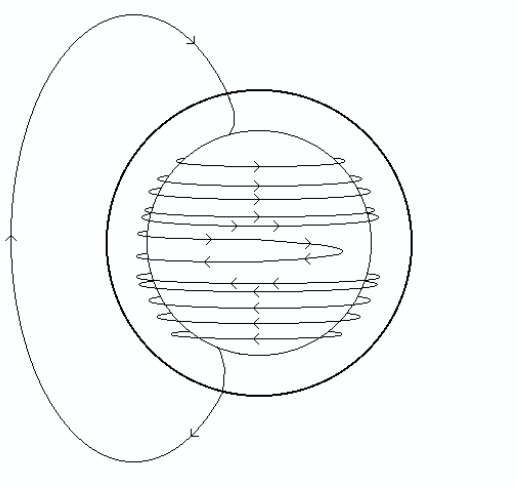

Figure 1.6: Schematic representation of the Omega effect. A primordial poloidal magnetic field is converted into a toroidal field through differential rotation. (http://science.nasa.gov/ssl/pad/solar/dynamo.html)

$$\frac{d}{dt} \int_S \vec{B} \cdot \vec{n} dA = 0, \qquad (1.2)$$

since according to the Stokes Theorem, the relation

$$\begin{aligned} \frac{d}{dt} \int_S \vec{B} \cdot \vec{n} dA &= \int_S \frac{d\vec{B}}{dt} \cdot \vec{n} dA - \oint_C (\vec{v} \times \vec{B}) \cdot d\vec{L} \\ &= \int_S \frac{d\vec{B}}{dt} \cdot \vec{n} dA \\ &\quad - \int_S (\vec{\nabla} \times (\vec{v} \times \vec{B})) \cdot \vec{n} dA. \end{aligned}$$

applies. In this equation S represents the area enclosed by the loop C. For $\eta = 0$, equation 1.2 describes the fact that the magnetic flux in a closed loop does not change. whether a magnetic field is 'frozen' in the plasma or the plasma is moved by the magnetic field motions, depends on the the Reynolds number. This value is calculated by $R_M = \tau_D v/L$, where v and L are characteristic values for the movement and the dimension of the plasma and τ_d represents the diffusion time, in which the magnetic field dissolves. In the case of a large R_M, e.g. in the Sun, the dissolving time of the magnetic field is long and the plasma can be transported. On the other hand, if the Reynolds number

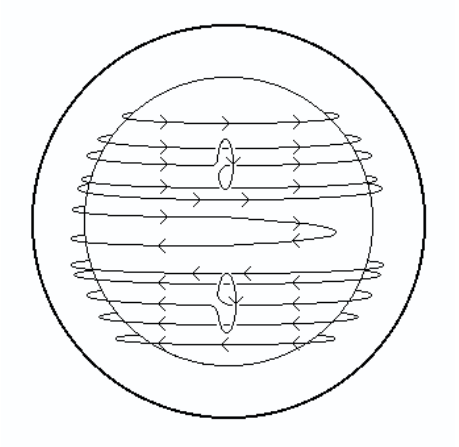

Figure 1.7: Illustration of the alpha effect, where the Coriolis force induces a rotation into the rising and expanding plasma cells. (http://science.nasa.gov/ssl/pad/solar/dynamo.html)

is small, the magnetic field dissolves so fast, that no significant transport occurs.

In the case of a large-scale, polodial magnetic field, whose field lines run from pole to pole in the stellar interior, the entire field rotates with the plasma of the star. Detailed spectroscopic and seismologic studies have shown that a significant number of stars are not rigid rotators. A rigid rotator is an object which rotates with the same angular velocity on all parts of the surface and in its interior. Instead, a significant fraction of stars show differences in rotation on the surface and in their interior. Under the influence of this differential rotation, the polodial field is twisted around the star. This mechanism converts the polodial field into a toroidal field, which might reach very high field strengths (see Figure 1.6). In this way, a weak polodial field in transformed into a strong toroidal field. This phenomenon is called the Ω effect. The resulting magnetic field is formed in a thin layer below the convection zone, called the overshoot region. This layer is characterized by infalling material from the convection zone into the radiative zone.

When the magnetic field rises with the plasma in the convection cells, these cells are influenced by the Coriolis force. The effect of the Coriolis force is the rotation of the plasma cells, resulting in a preferred rotation direction of the magnetic field. In this way the toroidal field is reconverted into a polodial field. The polarity of the new polodial field is in a reverse direction of the primordial field (see Figure 1.7). Due to reconnection of the magnetic field lines, the original configuration of the magnetic field can be restored. This phenomenon is called the α effect. The combination of the α and the Ω effect are able to explain the Sun's magnetic field cycle. In addition, the described dynamo model and the corresponding magnetic heating mechanism are able to explain the activity phenomena in the different layers of the stellar atmosphere of solar-like stars.

1.1.5 On the distinctiveness of A-type stars

In comparison to solar-like stars discussed above, the earlier and more massive A-type stars possess a significantly different internal structure. While the mid to late A-type stars are fully radiative, the dominating energy transport mechanism in the cores of the earliest A-type stars is convection. The convective motions are driven by the steep temperature gradient, arising from the burning of the CNO cycle. With increasing stellar mass, the convective core becomes larger and reaches more than 20 $\%$ of the stellar mass for the most massive O- and B-type stars.

Above the convective core follows a stable zone in radiative equilibrium. The material in this area is mixed with the core material by overshooting. Upward moving fluid parcels penetrate into the stable zone, decelerate and mix with their surrounding. Such overshooting motions affect the lifetime of the star on the main sequence, since they can transport new fuel into the core.

Just below the photosphere, two convective shells follow the radiative zone. The inner one contains mostly helium, the outer one is composed of hydrogen. These shells are much thinner than the convective zones of solar-like stars.

The masses of main-sequence A-type stars vary from 2 to 3.5 $M_{\odot}$ and the radii range from 1.5 to 2.1 $R_{\odot}$. With effective temperatures of 7000 to 10 000 K these stars do not possess the internal structure to drive atmospheric activity, which starts at early F-type stars.

Another phenomenon associated with X-ray activity in stellar atmospheres, strong winds, have

only been observed in the more massive O- and B-type stars, leading to the assumption that A-type stars have a simple structure and do not show any special features. Surprisingly, A-type stars possess a huge variety of spectral variations and peculiarities. At least 20% of the A-type stars show spectral anomalies, even at low spectral resolution. In addition, a large number of A-type stars are rapidly rotating stars and the resulting broadening of spectral features might hide the indicators for exceptional metallicities or magnetic fields. Therefore, the fraction of peculiar stars might be even larger.

In the following a brief introduction into the spectral subclasses of A-type stars is given. These subclasses are included in the sample of A-type stars which is studied in Chapter 2.

Subclasses of A-type stars

A-type giants

Stars in the same spectral class may show large differences in luminosity. The variations of the luminosity reach up to a factor of ten. To further differentiate the relatively rough classification of spectral classes, another criterion has been included into the spectral notation: the luminosity class. These subclasses are represented by roman numerals. Ia describes the most luminous hypergiants, Ib the less luminous supergiants, II the bright giants, III the normal giant stars and the least luminous evolved stars of luminosity class IV are called subgiants. Stars on the main sequence, e.g. the Sun, are of the luminosity class V and are called dwarfs. Due to an depletion of heavier elements, some stars have a luminosity which is 1.5 to 2 magnitudes lower than the luminosity of main sequence stars. These objects are called subdwarfs (sd) or luminosity class VI. The metaphorical denotation of dwarfs and giants are based on the size of the objects. Stars with the same spectral type exhibit roughly the same effective temperature and differ only in their radius. At the same temperature, a small 'dwarf' has a lower luminosity than a larger 'giant' star. In the HR diagram, the luminosity classes are arranged in horizontal lines with the most luminous classes on the top side of graph.

If a star is a member of the giant class or positioned on the main sequence depends on its stage of development. When the hydrogen reservoir in the stellar interior is exhausted, the inner core of the star contracts and the outer shells expand. Thus, the volume of the star increases while its surface temperature decreases. Accordingly, the star appears to be a member of a later spectral type but is more luminous than a star of the same surface temperature on the main sequence.

A-type stars of the luminosity classes V to III posses a similar internal structure, in contrast to the more evolved bright giants or supergiants. These massive objects evolve very fast, leading to a small number of observable A-type supergiants compared to the number of main sequence A-type stars.

Am stars

Finding an unambiguous definition of the class of Am stars (m for metallic lines) is an intricate task, since the occurring phenomena are of different origin and cannot be observed in all Am star spectra.

A classical definition of the class of Am stars is that the spectral subclasses derived from the Ca II K line and the ones derived from the hydrogen lines differ by more than five spectral subclasses. With this method it is possible to distinguish between some magnetic stars and those Am stars with weak K lines and strong Eu II, Cr II or Sr II lines. The drawback of this method is that spectral criteria are less sensitive for early A stars and appear primarily in the later A-type stars.

A second definition was proposed by Conti (1970), in which the surface underabundance of Ca (and/or Sc) and/or the enhancement of the iron group and heavier elements are decisive. This leads to three groups of Am stars: one with Ca depletion and Fe overabundance, and two other groups, in which only one of the criteria is fulfilled. The advantage of this method is the possibility to classify Am stars earlier than A5. In this early A-type stars, the strong hydrogen lines complicate the identification of some metal lines. The Ca/Sc criterion solves this problem.

One possibility for the observed metallicities is that the observed elemental abundances in the upper layers of the star represent the abundance of the entire star. In another scenario, there has been an accumulation of the elements near the surface after the formation of the star. This accumulation

is caused by the coupling of photons on their way to the surface with the ions of some elements, accelerating them towards the outer layers of the star. This so-called microscopic diffusion can only be detected in the absence of convection zones, since the involved mixing would prohibit any form of accumulation. Michaud (1970) showed that for elements with an ionization potential between 10.5 and 13.6 eV, like carbon, calcium, strontium, zirconium and radon, the buoyancy due to the radiation field of an Am star is stronger than the gravitational drag. Elements with an ionization potential of less than 10.5 eV or more than 18 eV, like helium, lithium, beryllium, bohrium, neon and sodium, receive a significantly weaker buoyancy, making the gravitational drag the dominating force.

Hui-Bon-Hoa & Alecian (1998) reviewed this model by searching for a correlation between the age of a star, determined by the age of the according star cluster, and the elemental abundances. Figure 1.8 shows the results of their studies. With increasing age, the nickel abundance increases, while the scandium abundance decreases. A problem with this scenario is that the atomic data of scandium and other heavy elements, are not known in detail and are needed for further simulations of the microscopic diffusion.

In addition the question arises whether Am stars might be in an evolved state of their life cycle. Several authors addressed this topic, like Jaschek & Jaschek (1967), Conti & van den Heuvel (1970), Smith (1970), Hartoog (1976) and van Rensbergen et al. (1978). Abt (1979) presented a summary of the corresponding data:

1. Am stars can be found in very young stellar populations like Orion. Thus, the peculiar metallicities can be formed in a few million years.

2. The mean frequency of Am stars in star clusters and in the Ori Ic association is comparable to those of field stars.

3. The frequency of Am stars is independent of the age of the according cluster, assuming that the age of the cluster is high enough for the A-type stars to reach the main sequence. The anomalies vanish with increasing age and the inherent development from the main sequence, indicating an upper limit for the phenomenon of the Am stars.

4. There are only marginal indications for a significant difference in the frequency of Am stars in different star clusters.

The fact, that metallicity can be observed with the same frequency in field stars and in star clusters, leads to the conclusion, that Am stars are located on the main sequence. This conclusion is supported by observations of spectroscopic binaries by Conti (1968). According to those observations, the frequency of spectroscopic binaries is constant from spectral types B to G, if the Am stars are included. On the other hand, if the Am stars are excluded from the sample, the spectroscopic binary frequency is significantly lower in the group of A-type stars than in the other spectral types.

Ap stars

The first observation of an Ap (p for peculiar) star was carried out by Maury in 1897, who discovered strange spectral properties at the A-type star α^2 CVn. Among these peculiarities were exceptionally strong K and weak Si II lines. Several years later Ludendorff and Belopolsky reported variable line strengths in Fe, Cr, Mg lines and the Eu lines at 4129 and 4205 Å. In addition, further observations revealed that α^2 CVn is a photometric variable star and that the maxima and minima in the light curve are correlated to the extrema of the line strength of Eu.

For a long time it was impossible to find a satisfactory explanation for this feature. Yet, in 1947 Babcock found an apparently variable magnetic field in 78 Vir (Babcock 1947), and as such fields were found in most of the other Ap stars, the rigid rotator model was devised. The fundamental idea of this model is that the axis of the large-scale, fossil magnetic field is not aligned with the rotation axis of the star. Due to the rotation of the the star, the constant magnetic field appears variable to a distant observer. The variability of the line strength of several elements is caused by a concentration of these elements on the surface of the star, which is supported by the long time stability of the magnetic field configuration. The ionized elements are fixed in position by the magnetic fields, leading to a higher concentration of specific elements

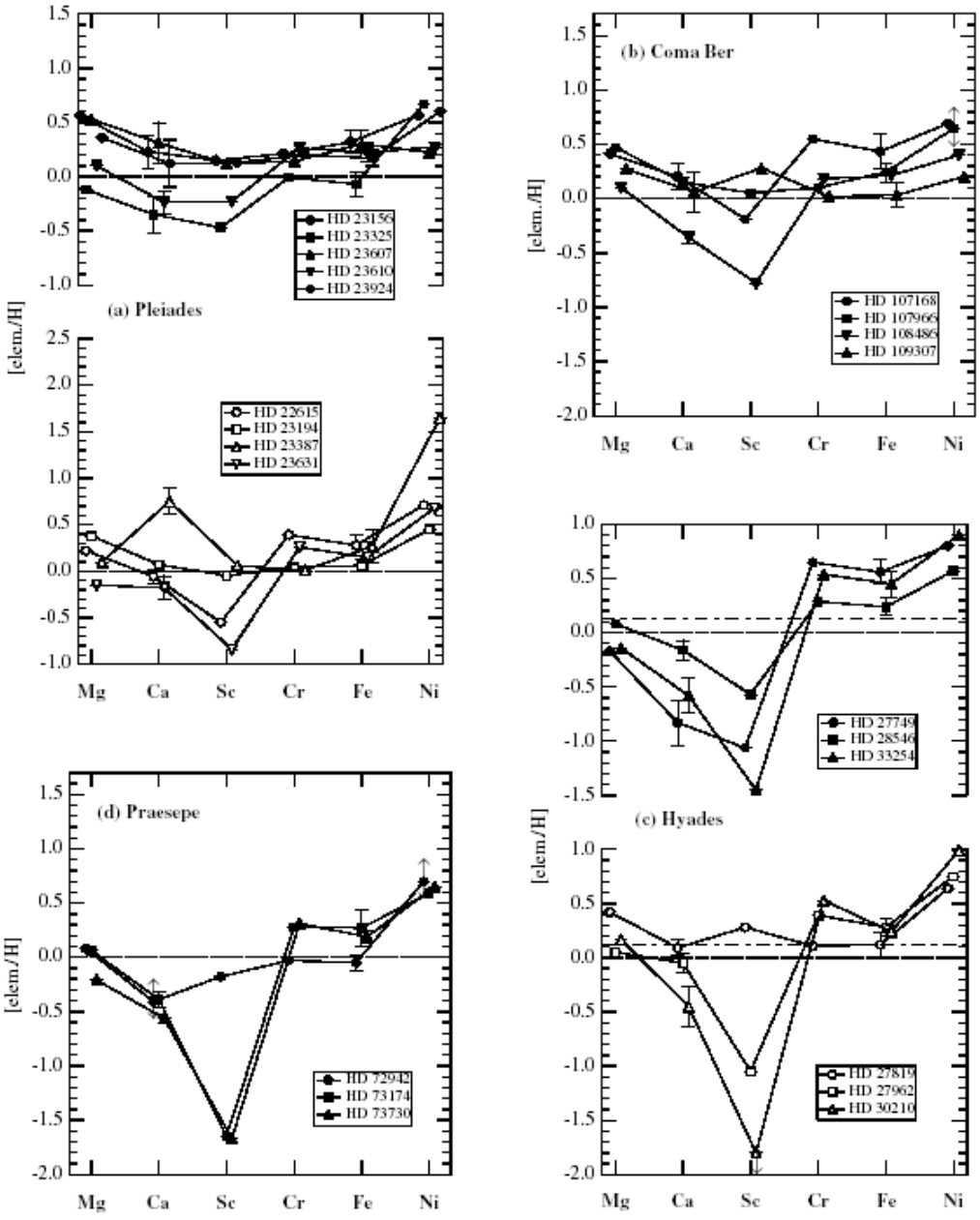

Figure 1.8: Abundances of individual Am stars of a) Pleiades, b) Coma, c) Hyades and d) Praesepe. The age of the clusters ranges from 50 to 700 million years. The increase of nickel and the decrease of scandium with increasing age is clearly visible (Hui-Bon-Hoa & Alecian 1998).

through microscopic diffusion.

As a result of the spectral peculiarities of these objects, it is a difficult task to find the correct spectral subclass for the individual Ap stars. Responsible for these problems are the spectral features, which counter the classification criteria, as well as the difficulties in estimating the temperatures and luminosities of the stars. The effective temperatures for example are lower than predicted by the UVB color index. Leckrone (1973) presented observations, which showed that the Ap stars appear more blue in the B-V index than normal A stars of the same spectral class, which led to an overestimated effective temperature of these objects.

As in the case of the Am stars, the question arises if the Ap stars are in an evolved state of their evolution and hence have left the main sequence. On the one hand, there are indications that Ap stars are located on the main sequence, for example the fact that they can be associated with young clusters like Orion and Scorpius-Centraurus and therefore would not have had enough time to leave the main sequence. On the other hand Hubrig et al. (2000) found that most of the Ap stars seem to be located on the upper end of the main sequence, but they note that there might be a bias in their sample: two third of their star have rotational periods of more than ten days. In the group of stars with periods of less than ten days, there are enough stars to search for correlation between the rotational period and the phase of evolution. The authors did not find such a correlation.

1.1.6 Winds and shocks

In the previous Sections I described the cause of the X-ray emission of solar-like stars and the special position of the A-type stars. Since the first X-ray observation more than 20 years ago it is known that O and B-type stars are X-ray emitters, too. Typical X-ray luminosities of these objects are 10^{32} erg/s for O stars and 10^{30} to 10^{31} erg/s for B stars. The ratio of X-ray luminosity to bolometric luminosity for these early-type stars is $\log\,(L_X/L_{bol}) = -7$. In a few cases this value increases up to -5. Since their first detection, several models have been developed to explain the X-ray emissions from hot stars. Due to the absence of the outer convection zone, the dynamo model is not able to give such an explanation. In the past 30 years, the following theories have been proposed to identify the origin of the X-ray emission of the most massive stars:

Base corona

Hearn (1972, 1973) suggested dissipation of acoustic waves as a possible mechanism of chromospheric and coronal heating and estimated the size of the corona, based on the equivalent width of the Hα line, at about one stellar radius. Cassinelli et al. (1978) corrected this value down to 0.1 R_*. Shortly after the launch of the Einstein satellite, this model was abandoned, since the X-ray emission below 1 keV was not so strongly absorbed as proposed by the base corona model. For the O5Ia star ζ Puppis, Baade & Lucy (1988) could rule out a corona as the X-ray emitting source, since no coronal Fe XIV line could be detected.

Blob model

Lucy & White (1980) suggested a phenomenological model for the structure of unstable, line driven winds. In this model radiation driven, dense gas clouds or clumps collide with gas in the surroundings of the star, which is screened from the radiation of the star by the clumps. Therefore, the gas is not exposed to radiation pressure. The X-ray emission is produced by shock fronts between the clumps and the surrounding gas. Although this model can be adjusted to the observed X-ray luminosities, the expected X-ray spectrum does not fit the observations: since the bow shaped shocks should reach their maximum strength near the star, the expected absorption of the soft X-rays is too strong to fit the observations.

Forward shocks

To include the shading of the clumps in the blob model, Lucy (1982) replaced the sequence of successive clumps with a saw tooth shaped structure of radiation driven, preceding shocks. In this model the forward shocks are shaded by the following shocks and dissolve (see Figure 1.9). As a result of this mechanism the X-ray emission can reach far into the outer areas of the winds. Although this model produced predictions which where qualitatively consistent with the data from Einstein observations, it failed to reproduce the X-ray luminosity by a factor of 20. Under the assumption that a small number of shocks is extremely strong, this model is consistent with the observations.

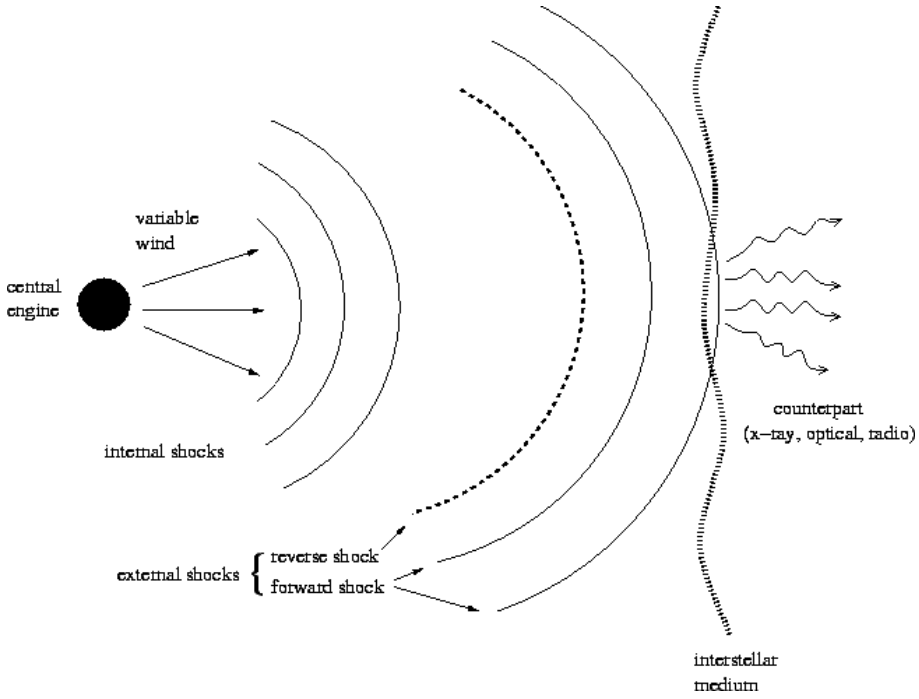

Figure 1.9: Schematic picture of the formation of shocks in radiation driven winds. (http://www.cabrillo.cc.ca.us/divisions/mse/phys/joes_thesis/node36.html)

Inverse Compton scattering

This model tries to explain the possible hard X-ray emission. White (1985) associated the non-thermal radio emission from some very hot stars with synchrotron radiation produced by relativistic electrons, which received their energy from the first order Fermi mechanism in the wind shocks. Thereby, the electrons are reflected multiple times between successive shock fronts and gain energy. Pollock (1987), Chen & White (1991) proposed inverse Compton scattering of UV photons at relativistic electrons as a source of the observed X-ray emission above 2 keV. The resulting spectrum should follow a power law$F \propto E^{-1/2}$. In agreement with this model, the spectra of Einstein observations of three Orion belt stars show a more flat developing than the exponential tail of a thermal component with a temperature of a few million degree.

Reverse shocks

After the discovery of Owocki et al. (1988), that line-driven instabilities in the winds of early-type stars may lead to the formation of reverse shocks instead of the formation of forward shocks, Macfarlane & Cassinelli (1989) developed a phenomenological model for the low-density winds of the B0V star τ Scorpii. In this model a perturbation leads to the formation of two shockfronts, a forward and a reverse shock, which confine a layer of high density gas. This combination of shockfronts and gas propagate into the wind. By adjusting the strength of the shocks through variation of the initial perturbations, this model is able to reproduce the Einstein observations of τ Scorpii, with the exception of the hard tail of the spectra. First hydrodynamic simulations of the X-ray emissions, in which hot gas is generated through the growth of initially small perturbations based of line-driven winds, were presented by Cooper & Owocki (1992, 1994). They used two different approaches for the thin winds of early B-type stars on the one hand and for the dense winds of O-type stars on the other hand. In the winds of B stars, cooling processes based on radiation can be neglected and only adiabatic cooling have to be considered. This leads to a huge amount of hot gas in the winds, however, not enough to explain the X-ray emission of these objects. Cassinelli (1994)

regarded this an indication that the presence of an huge amount of hot gas in the winds is responsible for the X-ray emission. For the dense winds in O-type stars Cooper and Owocki simulated isothermal wind structures, since the introduction of radiative cooling caused significant problems. Because of the presumed small cooling zones, this approximation should be feasible. Using the properties of the simulated shocks for the calculations of the X-ray emissions (under the assumption of stationary cooling zones), they found a good agreement between the model and the observed spectra, but the X-ray luminosity was 10 times higher than the observed value.

Clump infall

To be able to explain the hard spectrum and the redshifted UV absorption feature in the τ Sco data, Howk et al. (2000) developed a model, in which areas with high densities are formed in the wind of the star due to small perturbations. The studies on the dynamics of this clouds with respect to radiation pressure, gravitation, and drag revealed that the clouds get optically thick at the height of several stellar radii and, therefore, the radiative acceleration gets smaller than the gravity of the star. The clumps, which fall back towards the star, produce bowshocks. In this shocks the temperatures reach values of several 10^7 K, which are needed to produce the observed hard X-ray emissions. Additionally, the observed redshift of the absorption features as well as the absence of strong line broadening in Chandra spectra can be explained with this model, since the wind is decelerated by a factor of 4 due to the penetration of the shock fronts. Another advantage of this model is the correct prediction of the height, in which the infall of the clumps starts. This value can be observed by measuring the f/i-ratio of helium-like triplets. This method detects the ratio between forbidden and intercombination transition of helium-like elements. Under certain circumstances with respect to pressure, density, UV radiation field, etc., these ratio changes towards more frequent forbidden transitions compared to the intercombination transitions. This phenomenon can be observed in the strengthening or weakening of the according lines. The measurement of the line strengths allows to draw conclusions about the physical properties at the point of the lines' origin.

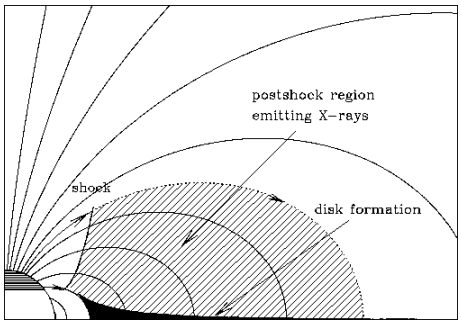

Figure 1.10: Schematic picture of the magnetically confined wind shock model for IQ Aur (Babel & Montmerle 1997).

Magnetically confined wind shocks

The relative young age and the slow projected rotational velocity suggest that τ Sco possesses a fossil magnetic field. Calculations of the radiation-driven winds in combination with magnetic fields provide the opportunity for a different model than the different forms of cloud models. Babel & Montmerle (1997) proposed a shock model based on the confinement and the compression of winds in a suitably strong dipole field for the X-ray emitting A-type stars IQ Aurigae (see Figure 1.10). The gas clouds are channeled along the field lines, collide on the magnetic equator and produce shocks. With this model it is possible to explain the areas of high densities at a distance of several stellar radii. According to the calculations, a magnetic field strength of 100 G would be enough to explain the observations of τ Sco. This model has been successfully adapted to other young and hot stars, e.g. σ Ori C (Donati et al. 2002; Gagné et al. 2005). A detailed description of the magnetically confined wind shock model is given in Chapter 3.

As can be seen on the various models developed in the last decades, there has been no uniform picture on the X-ray production mechanisms in the surroundings of hot stars. While most of the observations can be explained by one of the shock models with hot plasma distributed in the wind of the star, some individual stars do not fit into this pattern and the according models have to be adjusted. There is still a lot of discussion if this is a problem of the models or if there is just a huge

variety of X-ray emission mechanisms. The most promising model is the magnetically confined wind shock model, and a lot of effort has been spent to further improve the model (Ud-Doula & Owocki 2003; Ud-Doula et al. 2005).

1.2 Observational methods

The following sections give an introduction in the observational methods which have been applied to study the activity phenomena at the onset of the solar-like dynamo. Sections 1.2.1 and 1.2.2 give a brief overview of the ROSAT mission and X-ray astronomy. Magnetic field measurements are described in Section 1.2.3 and Section 1.2.4 presents a summary of previous Ca II H&K measurements.

1.2.1 X-ray astronomy

X-ray observations are a relatively young field in astronomy. The reason for this is that the Earth's atmosphere absorbs the vast majority of X-rays and therefore X-ray sources cannot be observed from the ground. With the development of rocket technology in the Second World War the possibility arose to leave the Earth's atmosphere and bring X-ray telescopes into space. First tests with Geiger counters mounted on rockets showed that the Sun and objects outside the solar system are X-ray emitters.

The first satellite launched specifically for the purpose of X-ray astronomy was 'Uhuru' (Swahili for freedom). It began its two years of observation in December 1970 and discovered 339 X-ray sources. Uhuru was followed by e.g. the High Energy Astronomy observatory (HEAO-1) in August 1977. HEAO-1 scanned the sky in the range of 0.2 keV to 10 MeV, provided pointed observations and almost constant monitoring of X-ray sources near the ecliptic poles. About a year later, in November 1978, HEAO-2 was launched to perform pointed observations in the range of 0.2 to 3.5 keV. This satellite, more commonly known as Einstein, was the first fully imaging X-ray telescope after the Skylab mission in 1973 and offered unprecedented levels of sensitivity.

On June 1, 1990 the German X-ray satellite ROSAT (acronym for Roentgensatellit) was launched on top of a Delta II rocket. With more than 100 000 detected sources in the full-sky survey and eight years of life time ROSAT was one of the most successful scientific missions of those years.

The most recent X-ray telescopes are the complementary XMM-Newton and Chandra X-ray Observatory, which were both launched in 1999. While XMM-Newton is characterized by high sensitivity and simultaneous imaging and spectroscopic observations, Chandra offers an unprecedented spatial resolution of 0.5 arcseconds. Both missions are supposed to continue far into the next decade and provide new insights in the physics of X-ray sources.

1.2.2 ROSAT

Due to its instrumentation, ROSAT was capable to observe in the extreme ultraviolet (XUV), as well as in the the soft X-ray. The Wide Field Camera (WFC) was provided by British Science and Engineering Council (SERC) to carry out the XUV observations. It covered the range between 0.042 and 0.21 keV or 300 to 60 Å. The X-ray observations were carried out by two different instruments: the position sensitive proportional counter (PSPC), which was provided by the Max-Plank-Institute for Extraterrestrial Physics (MPE) and the high resolution imager (HRI), which was contributed by NASA. A similar instrument was mounted on the Einstein mission. These instruments covered a spectral range from 0.1 to 2 keV (100 - 6 Å) in X-rays.

From the two redundant PSPCs which were used on ROSAT, one failed in January 1991. These multi wire proportional counters possessed two wire grids to detect the position of the incoming photons. Additionally, these photons were allocated to one out of 256 pulse height channels. The provided energy resolution was $\delta E/E = 0.43 * (E/0.93)^{-0.5}$. The entrance window of the detector had a diameter of 8 cm, resulting in a field of view of 2 degrees. To seal the gas chamber, a propylene foil was used, which was supported by wire structure (see Fig 1.11). Two different wires meshes were fixed on the rib structures to withstand the gas pressure of 1466 mbar at 22° C. Since the ribs and the meshes were impenetrable for X-rays,

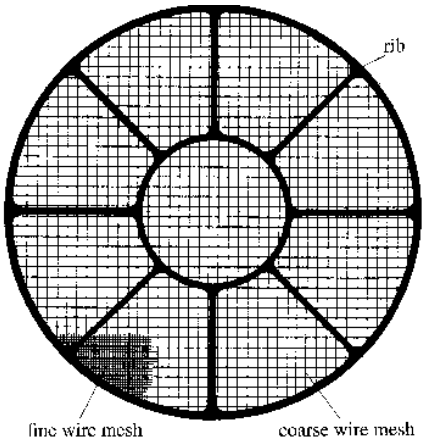

Figure 1.11: The support structure of the propylene foil with the two different wire meshes. (http://www.heasarc.gsfc.nasa.gov/docs/rosat/pspc.html)

the satellite performed an oscillating movement to prevent the occultation of sources. The period of these 'wobbles' was 400 seconds and the positions of the photons had to be corrected with the attitude. With this configuration, the PSPC offered a spatial resolution of around 20 arcseconds.

The second instrument for the X-rays was the high resolution imager (HRI), which was built up out of two cascaded microchannel plates with a crossed grid position readout system. A very similar detector was used on the Einstein observatory. The HRI had a negligible energy resolution, but compared to the PSPC the spatial resolution of 6 arcseconds was significantly higher. The square field-of-view of the HRI was 38 arcminutes. In contrast to the PSPC, which was used for the survey and for pointed observations, the HRI was only used for pointed observations.

One characteristical property of the X-ray emission is that the high-energy photons penetrate materials usually used as mirrors or lenses without refraction or reflection. Since the energy of a single photon in the keV range is roughly 1000 times higher than the energy of an optical photon, it is impossible to focus the X-rays through classical lenses like in optical instruments. In fact, the deflection is achieved through grazing reflection of the X-ray photons on a highly polished surface. Today's X-ray telescopes utilize a parabolic mirror as well as a hyperbolic mirror system to correct for aberration and to achieve the needed image quality. In 1952 Hans Wolter outlined this type of optical system to build an X-ray microscope, but he failed due to the insufficient polishing of the surface of his mirrors. The wavelength of X-ray photons is comparable to the size of an atom, resulting in a receptiveness to even slightest unevenness in the X-ray optics. Therefore, the requirements for the mirrors are extremely high. For the ROSAT satellite, an X-ray telescope with a mirror assembly of a four-fold nested Wolter type I with an 84 cm diameter and a focal length of 240 cm was used. The high quality of the mirrors surface made a huge contribution to the success of the mission.

Mission

The first part of the ROSAT mission was the all-sky survey, which mapped the whole celestial sphere. After a first test and calibration phase, the survey started on July 30, 1990 and was completed about half a year later on January 25, 1991. Since some parts of the sky were missed out due to a defect near the end of the survey, additional survey observations were inserted in the observation schedule in summer 1991. The geometry of the orbit of ROSAT was utilized for the execution of the survey. Through a 96 minute orbit period which was synchronized to the rotation period of the satellite, ROSAT was able to perform scanning observations on great circles perpendicular to the plane of the ecliptic. Additionally, the great circles were perpendicular to the line Earth-Sun. While the Earth moves on its orbit around the Sun, the great circles rotate around an axis through the ecliptical poles. After half a year, the scan circles have been rotated by 180° and have covered the whole sky. This geometry assures that the telescope is never pointed towards the Sun or towards the Earth, which would damage the detectors. Another advantage is the constant power supply, since the solar panels are always pointed towards the Sun.

The main purpose of the pointing mode was the detailed observation of some selected targets. It was possible to aim at targets in the area of $90° \pm 15°$ towards the Sun. The maximal duration of a continuous observation was 90 minutes.

Based on the data obtained with ROSAT, a detailed search for X-ray sources at the position of bright A-type stars was performed. The correlation of the ROSAT catalogs and the A-type stars contained in the Bright Star Catalogue (Hoffleit & Warren 1995) is presented in Chapter 2.

1.2.3 Magnetic fields

Stellar magnetic fields are characterized and detected using the Zeeman effect, which was first described in 1897 by Pieter Zeeman in his pioneering paper 'The Effect of Magnetisation on the Nature of Light Emitted by a Substance'. If an atom is immersed in an external magnetic field, individual atom levels with the energy E_0, the total angular momentum J and the Landé factor g are split into 2J+1 substates, characterized by the magnetic quantum number M ($-J \leq M \leq +J$). The energies of these atomic states are given by

$$E_M = E_0 g M \hbar \omega_L, \tag{1.3}$$

where $\omega_L = eB/(2m_e c)$ is the Larmor frequency (Mathys 1989). As a result of this splitting, each transition that generates a single line in the stellar spectrum when no field is present leads, in the presence of a field, to a group of closely-spaced spectral lines, or Zeeman components (see Figure 1.12). The interaction between the quantum the orbital angular momentum L and the spin angular momentum S is called Russell-Saunders coupling or LS coupling. For transitions in LS coupling, these lines may be grouped into two different types with different properties. Those lines resulting from transitions in which M does not change (i.e.$\Delta M = 0$) are spread symmetrically about the zero-field wavelength $\lambda_0 = hc/E_0$ of the line. These are called the π components. Those resulting from transitions in which $\Delta M = \pm 1$ have wavelengths shifted to the red (+) and blue (-) of the zero-field wavelength. These are called the σ components. The wavelength separation between the centroids of the π and σ component groups can be calculated from equation 1.3, and is:

$$\Delta\lambda = \frac{eN\bar{g}}{4\pi m_e c^2}\lambda_0^2 \equiv \Delta\lambda_z B\bar{g}, \tag{1.4}$$

where $\bar{g}$ is the effective Landé factor of the transition and λ_z is called the Lorentz unit. The splitting

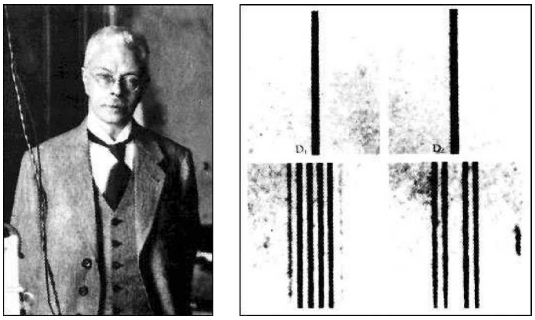

Figure 1.12: On the left side a picture of Pieter Zeeman. The right side shows the splitting of the Na D triplet under the influence of a magnetic field.

is directly proportional to the strength of the field B. As an example, the splitting of a 5 kG field at 5000 Å is about 0.1 Å.

Zeeman furthermore investigated, on the suggestion of Lorentz, the polarization properties of the π and σ components. He found that in a longitudinal magnetic field, the π components vanish, whereas the σ components have a opposite circular polarizations. On the contrary, when the magnetic field is aligned perpendicular to the observer's line-of-sight (transverse field), the π components are linearly polarized parallel to the field direction, while the σ components are linearly polarized perpendicular to the to the field direction. Summing up, the spectral lines are split into multiple Zeeman components in the presence of a magnetic field and the polarization bears information about the orientation of the field at the line-forming region.

In the 'weak-field limit', when the ratio of the Zeeman splitting ΔZ to the intrinsic width ΔI of the line $\Delta Z/\Delta I \ll 1$, one obtains the first-order solution for the Stokes profiles emergent from a stellar photosphere:

$$I(\tau = 0, \lambda) = B_0 + B_0 \beta\mu[1 + \eta(\lambda)]^{-1} \tag{1.5}$$

$$Q(\tau = 0, \lambda) = 0 \tag{1.6}$$

$$U(\tau = 0, \lambda) = 0 \tag{1.7}$$

$$V(\tau = 0, \lambda) = -\bar{g}\Delta\lambda_Z B_Z \frac{dI(\lambda)}{d\lambda}, \tag{1.8}$$

where B_0 and β_0 are the Millne-Eddington parameters, μ is the limb angle, $\eta(\lambda)$is the line opacity in the absence of a magnetic field and B_Z is the longitudinal component of the magnetic field.

Equation 1.5 is the Milne-Eddington solution for the emergent Stokes I profile in the absence of a magnetic field, i.e., to first order, the Stokes I profile is unaffected by the presence of a weak magnetic field. Furthermore, equations 1.6 and 1.7 show, to first order, that the line profile is not linearly polarized for weak fields. In fact, the only first-order influence of the magnetic field in the weak-field regime is on the amplitude of the Stokes V profile. For any spectral line, the shape of Stokes V is determined entirely by the shape of the corresponding Stokes I profile, via the derivative $dI/d\lambda$. However, the amplitude of Stokes V is proportional to the intensity of the longitudinal component of the magnetic field. This implies that for most stars, the most easily accessible Zeeman diagnostic will be circular polarization of the line, and for such stars practically only the longitudinal field component can be measured. The linear polarization Stokes parameters, which constrain the transverse components of the field, will in general be much weaker (appearing only at second order), and consequently much more difficult to detect. Synthetic line profiles, illustrating the influence of field strength on the splitting and polarization profile amplitudes, are shown in the upper part of Figure 1.13.

In real stars, our ability to diagnose magnetic fields depends on various (nonmagnetic) physical and spectroscopic attributes (e.g., visual magnitude, S/N , spectral line depth and density, rotational velocity, spectral resolving power of the spectrograph, etc.), as well as the magnetic field. In many situations, the observable signal may be near the practical limits of available instrumentation. This problem is illustrated in the lower part of Figure 1.13, in which the disc-integrated line profiles of an unresolved, rotating, magnetic star are simulated.

Typically, Zeeman circular polarimetry is obtained differentially, by recording the two orthogonal polarization states (left and right circularly polarized light, separated using a $\lambda/4$ retarder and a polarising beamsplitter) simultaneously on a CCD. The sum of the recorded fluxes gives the natural light spectrum (Stokes I), whereas their difference gives the net circularly polarized flux (Stokes V). This procedure is described in detail by, e.g. Bagnulo et al. (2002) and Hubrig et al. (2003). The application of this method to measure magnetic fields in A-type stars associated with X-ray sources is presented in Chapter 3.

1.2.4 Ca II H&K measurements

One important aspect in understanding the activity phenomena in the solar and stellar atmospheres and underlying dynamo is the variation of the chromospheric activity with time. In 1966, Olin Wilson began his pioneering observation of the Ca II H&K lines at the Mount Wilson Observatory (the matching of the names is a coincidence). In the presentation of the first results of this long term study (Wilson 1978), he concluded that all stellar chromospheres were variable to some extent, that cyclical variations very likely exist, and that they should be considered to be generated and dissipated by processes and structures analogous to those of the Sun. Sally Baliunas continued the so called 'HK Project' until 2003. The collected data represent one fundamental basis of the understanding of the chromospheric stellar activity. Mayor summaries of the observations are given by Wilson (1978); Duncan et al. (1991); Baliunas et al. (1995). The activity of the stars measured in the HK Project is given in terms of the dimensionless S index, which represents the ratio of emission in the Ca II H&K line cores compared to the emission in nearby continuum bandpasses. The S values were constructed as $S = \alpha(H + K)/(R + V)$, where H, K, R, and V are the values for the flux measured in the according bandpasses and α is an instrumental calibration factor. Figure 1.14 shows the two 1.09 Å wide H and K filters in the center of the lines and the 20 Å wide R and V continuum filters at 3901 and 4001 Å. A detailed description of the MWO activity measurements is given in Chapter 4. Baliunas et al. (1998) found cyclic, periodic variations in 60% of the stars in the Mount Wilson Observatory (MWO) survey, 25% showed irregular or aperiodic variability and 15% showed flat activity (see Figure 1.15). Given this rough classificication of activity, there are also stars that show

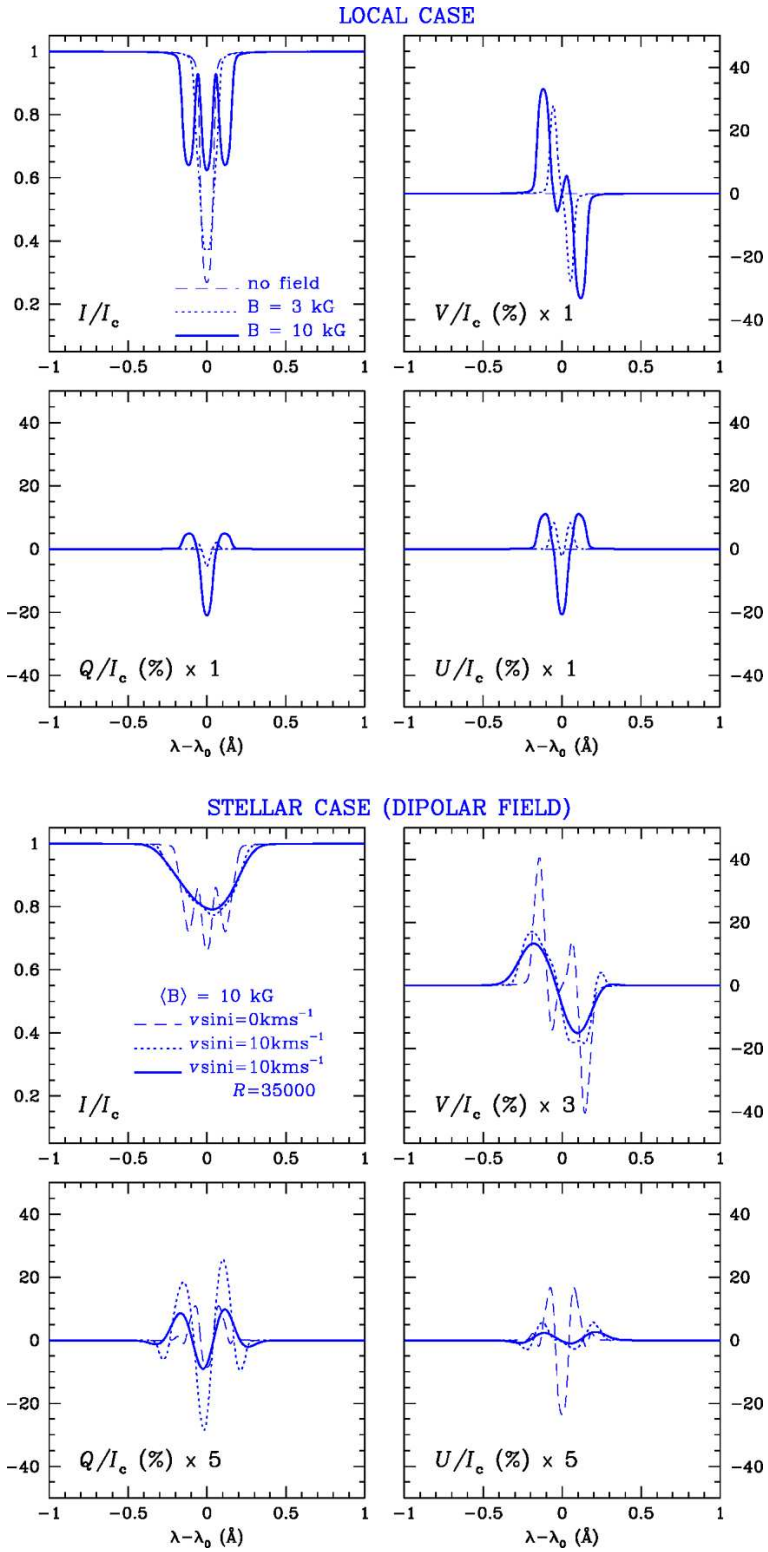

Figure 1.13: Upper panel: the effect of different magnetic field strengths on a spectral line. Shown are the natural light (Stokes I), the circular polarization (Stokes V) and the linear polarization (Stokes Q and U). Each of these different profiles are connected to a single intensity and direction of the magnetic field. Lower panel: disk-integrated line profiles as they are observed in an unresolved star with a distribution of field strengths over the observed hemisphere. Profiles are shown for rotational velocities v sin(i) = 0 km/s, v sin(i) = 10 km/s and v sin(i) = 10 km/s with additional instrumental broadening according to the given spectral resolution R = 35 000 (Wade 2004).

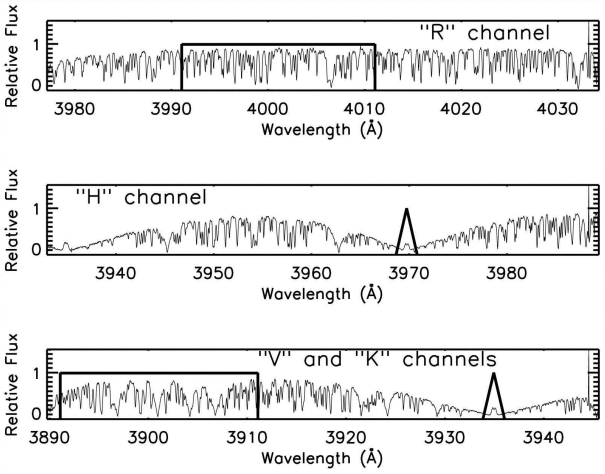

Figure 1.14: The filters used to determine the S index. Size and position of the filters are based on the HKP-2 spectrometer, which was used for the Mount Wilson observations (Wright et al. 2004).

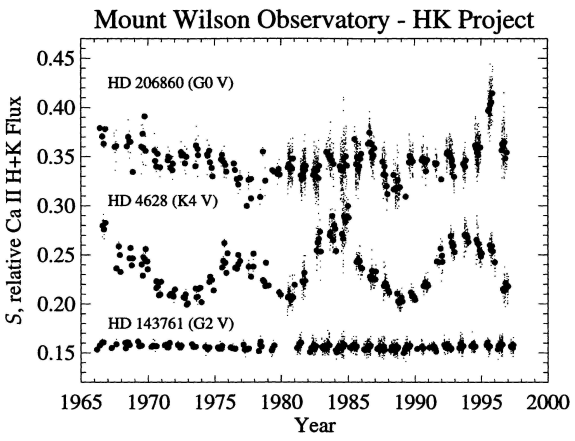

Figure 1.15: Variations of the S index for three stars with different activity patterns. On top is shown an irregular variable star, in the middle a periodic variable and on the bottom a flat activity star (Baliunas et al. 1998)

evidence for multiple periodicities (Baliunas et al. 1995). This general distribution of activity levels is found in a complementary program too, the Solar-Stellar Spectrograph (SSS) program at the Lowell Observatory (Hall et al. 2007). Generally speaking, the MWO stars decrease in the amplitude and in the mean level of chromospheric activity with increasing cycle length. Cycles shorter than six years have not been observed (Baliunas & Soon 1995).

An interesting side product of the cycle observations in the MWO data is the possibility to search for rotation periods and even differential rotation via drifts in rotation-timescale periodicities in activity index S. The basic assumption for this method is the idea that the emergence sites of the stellar active regions migrate in latitude like their solar counterparts and that their evolution does not distort the signal. The first attempts by Baliunas et al. (1985) to extract the weak signal of differential rotation had limited success, but Donahue & Baliunas (1992) reported the detection of a drift in the apparent rotation period in the G0V star β Com (HD 114710). Interestingly, the direction of the change was opposite to that of the Sun, with longer periods late in the cycle. From the migration of the solar active regions late in the cycle towards the equator, which rotates faster than the poles, we would expect shorter periods for a solar-like differential rotation. Another way to further investigate this topic are Photometric Doppler imaging techniques, which have been applied to a number of very active stars (e.g. Strassmeier (1996) and subsequent papers in the series). On the other hand, Hempelmann (2003) argues that the HK proxy and similar diagnostics such as Mg II and Ly α are more fruitful avenues for this kind of work in low-activity, solar-like stars. Their advantage is that they are not affected by the cancellation of active region brightening and spot darkening.

Due to instrumental limitations and the necessity of maintaining a relatively high observing cadence on samples of about 100 stars, the MWO and Lowell data sets are magnitude limited to about $m_V < 7$. They have been supplemented by several observation programs, which both reach fainter stars and provide a broader range of chromospheric activity.

Henry et al. (1996) observed Ca II H&K activity in over 800 southern solar-like stars. Some results of the measurements are shown in Figure 1.16. They represent the typical color-activity appearance of Sun-like stars. Henry defined four activity classes, ranging from 'very active' with the chromospheric emission ratio $R'_{\rm HK}$ of more than -4.25 to 'very inactive' stars with log $R'_{\rm HK}$ values of

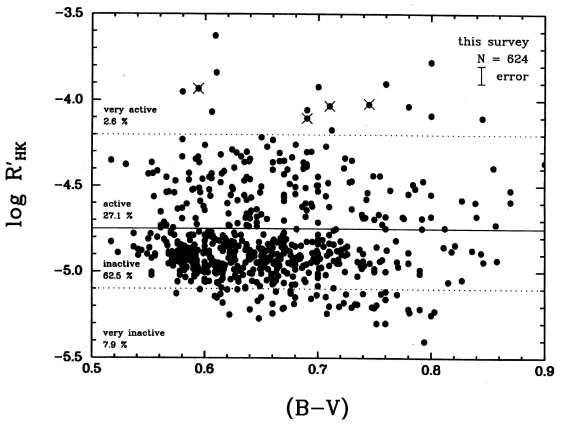

Figure 1.16: Distribution of activity in the 815 stars observed by Henry et al. (1996). The plot shows the four activity regions.

less than -5.1. The emission ratio is defined as $R'_{\rm HK} = (1.34 \times 10^{-4}\ C_{cf}\ S) - R_{\rm phot}$, where C_{cf} is a color dependent conversion factor, S is the activity index and $R_{\rm phot}$ is the photospheric contribution to the measured flux in the Ca II line cores. About 90% of the stars in their sample are located in the 'active' or 'inactive' region, with a deficiency between these two region, which leads to a bimodal distribution of activity. Additionally, there was an excess of very low-activity stars with $R'_{\rm HK} < -5.1$, which might be stars in a Maunder Minimum-like state.

Another addition to the MWO data was presented by Wright et al. (2004), based on the Carnegie Planet Search data set. From the observations of more than 1200 stars, values for S, $R'_{\rm HK}$, chromospheric ages and rotation rates have been derived, making this sample the largest survey presented to date.

Giampapa et al. (2006) measured the Ca II $H\&K$ emission of solar-like stars in the open cluster M67, probing a fainter sample than the MWO data at a solar-like age. The observed chromospheric activity was comparable to the values of actual solar cycles, although about 25% of the stars were found outside the modern solar cycle excursion. Around 15% of these were found to have activity levels below the present solar minimum, which is comparable to the frequency of flat activity stars in the MWO and Lowell surveys. If these stars are truly in non-cycling states or solely show the minima of cyclic stars is still unknown.

Another more recent survey presented by Gray et al. (2003, 2006) obtained a bimodal activity distribution essentially identical to that of Henry et al. (1996), including a significant excess of possibly Maunder Minimum stars at $R'_{\rm HK} \leq -5.1$. They found that the apparently ubiquitous bimodal distribution was in fact a function of metallicity. Those stars with [M/H] < -0.2 do not show a bimodal activity distribution. Gray et al. (2006) interpret this as a possible physical change that allows the presence of active chromospheres for solar-metallicity stars, while suppressing them in metal-deficient stars. The picture is complicated by the presence of active stars in the metal-poor sample.

All these surveys are based on the method of the MWO survey. A known problem of this method is the fact that the emission measured in the Ca II H&K line core is influenced by the rotational broadening at high rotational velocities. Additionally, the correction for the photospheric contribution to the measured values has not been determined for early F-type stars and giants. Therefore, the previous survey are focused on late F to late K dwarfs. A new method to measure the chromospheric activity in Ca II H&K for rapidly rotating stars at the onset of the solar-like dynamo is presented in Chapter 4, including a comparison to the MWO method.

1.3 Outline

The present thesis deals with observation of stellar activity at the onset of the solar-like dynamo. To study the activity phenomena in this special region, where the stellar interior is subject of significant changes, two different approaches were chosen. In the first part, a comprehensive survey of possible X-ray emitting A-type stars is presented. The second approach is measuring the chromospheric Ca II H&K activity in rapidly rotating solar-like stars.

Chapter 2 contains the results of the search for X-ray emitting A-type stars. The list of stars which have been tested for X-ray emission contains 1966 objects presented in the Bright Star Catalogue (Hoffleit & Warren 1995). A correlation between

the optical position of the stars and the positions of nearby X-ray sources listed in the ROSAT All-Sky Survey and pointed observations revealed that 312 A-type stars can be associated with X-ray sources. The matching criteria for the survey data were 90 arcseconds, 36 arcseconds for the pointing data with the PSPC and 18 arcseconds for the HRI data. Since the common explanation for X-ray emission from A-type stars are unresolved late-type companions, the presented study includes the search for signs multiplicity in the 312 objects given in Table 2 and 3 in Chapter 2. The resulting 84 bona fide single or resolved multiple stars are promising candidates for follow-up observations.

Based on the hypothesis that the X-ray emission from single A-type stars is produced by a magnetically confined wind-shock as proposed by Babel & Montmerle (1997) for IQ Aurigae, individual objects which can be associated with X-ray sources have been tested for the presence of magnetic fields (see Chapter 3). The observations have been carried out on August 28th 2006 with FORS1 at the VLT Kuyen. This multi-mode instrument allows the measurement of circular polarization caused by large-scale magnetic fields. Due to observational contrains, not all of the observed stars were top priority targets. The observations and the data reduction were carried out by S. Hubrig, who also provided the tools to calculate the magnetic fields. Although three out of 13 stars observed in this program showed Zeeman features which were strong enough for a detection at a 3 σ level. Close inspection by eye revealed Zeeman features in individual lines for nine additional stars. The magnetically confined wind-shock model predicts a correlation between the strength of the magnetic field and the X-ray luminosity, but no clear dependence between the two values could be found. A possible explanation might be that parameters like the wind velocity or the mass loss rate have a large impact on the X-ray properties of the star.

To observe the onset of the solar-like dynamo in the hottest solar-like stars, a new method to measure the Ca II H&K activity had to be developed. This is due to the fact that the classical Mount Wilson method is influenced by the rotational broadening of the lines. In addition, some of the parameters which have to be determined to calculate the chromospheric activity are not defined for stars with B-V < 0.45. Therefore, the onset of the solar-like dynamo has not been observed in Ca II H&K before. The new method presented in Chapter 4 is based on the comparison of activity of a star with an inactive template star. With this technique it is possible to measure the chromospheric emission ratio log $R'_{\rm HK}$ for stars with B-V < 0.45. Our sample of solar-like stars consists of 481 objects ranging from late A- to late K-type stars. The observations, data reduction and determination of the basic stellar data like log g and $T_{\rm eff}$ of 326 of these stars were carried out by A. Reiners. For the 481 stars, the S index and, where determined, the log $R'_{\rm HK}$ values were measured. Table 2 in Chapter 4 lists the basic data and the activity measurements of the 481 stars. The number of stars measured with the template method is smaller, because of the limited number of template stars. A detailed description of the classical and the template method as well as a comparison between the results of the two methods are given in Chapter 4.

Finally, a summary can be found in Chapter 5 as well as an outlook to future projects.

References

Abt, H. A. 1979, ApJ, 230, 485

Audard, M., Osten, R. A., Brown, A., et al. 2007, A&A, 471, L63

Baade, D. & Lucy, L. B. 1988, in IAU Symposium, Vol. 132, The Impact of Very High S/N Spectroscopy on Stellar Physics, ed. G. Cayrel de Strobel & M. Spite, 123–+

Babcock, H. W. 1947, ApJ, 105, 105

Babcock, H. W. 1961, ApJ, 133, 572

Babel, J. & Montmerle, T. 1997, A&A, 323, 121

Bagnulo, S., Szeifert, T., Mathys, G., Wade, G. A., & Landstreet, J. D. 2002, in Astronomical Society of the Pacific Conference Series, Vol. 274, Observed HR Diagrams and Stellar Evolution, ed. T. Lejeune & J. Fernandes, 610–+

Baliunas, S. & Soon, W. 1995, ApJ, 450, 896

Baliunas, S. L., Donahue, R. A., Soon, W., & Henry, G. W. 1998, in Astronomical Society of the Pacific Conference Series, Vol. 154, Cool Stars, Stellar Systems, and the Sun, ed. R. A. Donahue & J. A. Bookbinder, 153–+

Baliunas, S. L., Donahue, R. A., Soon, W. H., et al. 1995, ApJ, 438, 269

Baliunas, S. L., Horne, J. H., Porter, A., et al. 1985, ApJ, 294, 310

Biermann, L. 1941, Vierteljahresschrift der Astr. Ges., 76, 194

Bohlin, J. D., Vogel, S. N., Purcell, J. D., et al. 1975, ApJ, 197, L133

Cassinelli, J. P. 1994, in Astronomical Society of the Pacific Conference Series, Vol. 57, Stellar and Circumstellar Astrophysics, a 70th birthday celebration for K. H. Bohm and E. Bohm-Vitense, ed. G. Wallerstein & A. Noriega-Crespo, 112–+

Cassinelli, J. P., Olson, G. L., & Stalio, R. 1978, ApJ, 220, 573

Chen, W. & White, R. L. 1991, ApJ, 381, L63

Conti, P. S. 1968, Highlights of Astronomy, 1, 437

Conti, P. S. 1970, PASP, 82, 781

Conti, P. S. & van den Heuvel, E. P. J. 1970, A&A, 9, 466

Cooper, B. C. & Owocki, S. P. 1992, in Astronomical Society of the Pacific Conference Series, Vol. 22, Nonisotropic and Variable Outflows from Stars, ed. L. Drissen, C. Leitherer, & A. Nota, 281–+

Cooper, R. G. & Owocki, S. P. 1994, Ap&SS, 221, 427

Donahue, R. A. & Baliunas, S. L. 1992, ApJ, 393, L63

Donati, J.-F., Babel, J., Harries, T. J., et al. 2002, MNRAS, 333, 55

Donati, J.-F., Collier Cameron, A., Hussain, G. A. J., & Semel, M. 1999, MNRAS, 302, 437

Duncan, D. K., Vaughan, A. H., Wilson, O. C., et al. 1991, ApJS, 76, 383

Eddy, J. A. 1976, Science, 192, 1189

Edlén, B. 1945, MNRAS, 105, 323

Ferrero, R. F., Gouttebroze, P., Catalano, S., et al. 1995, ApJ, 439, 1011

Fleming, T. A. & Giampapa, M. S. 1989, ApJ, 346, 299

Fleming, T. A., Giampapa, M. S., & Garza, D. 2003, ApJ, 594, 982

Gagné, M., Oksala, M. E., Cohen, D. H., et al. 2005, ApJ, 628, 986

Giampapa, M. S., Hall, J. C., Radick, R. R., & Baliunas, S. L. 2006, ApJ, 651, 444

Giampapa, M. S. & Liebert, J. 1986, ApJ, 305, 784

Gough, D. O. 1990, Nature, 347, 346

Gray, R. O., Corbally, C. J., Garrison, R. F., et al. 2006, AJ, 132, 161

Gray, R. O., Corbally, C. J., Garrison, R. F., et al. 2003, in Bulletin of the American Astronomical Society, Vol. 35, Bulletin of the American Astronomical Society, 1273–+

Hale, G. E. 1908, ApJ, 28, 315

Hale, G. E. & Nicholson, S. B. 1925, ApJ, 62, 270

Hall, D. S. 1991, Springer Verlag, New York

Hall, J. C., Lockwood, G. W., & Skiff, B. A. 2007, AJ, 133, 862

Hartoog, M. R. 1976, ApJ, 205, 807

Hearn, A. G. 1972, A&A, 19, 417

Hearn, A. G. 1973, A&A, 23, 97

Hempelmann, A. 2003, A&A, 399, 717

Henry, T. J., Soderblom, D. R., Donahue, R. A., & Baliunas, S. L. 1996, AJ, 111, 439

Hoffleit, D. & Warren, Jr., W. H. 1995, VizieR Online Data Catalog, 5050, 0

Howk, J. C., Cassinelli, J. P., Bjorkman, J. E., & Lamers, H. J. G. L. M. 2000, ApJ, 534, 348

Hubrig, S., Bagnulo, S., Kurtz, D. W., et al. 2003, in Astronomical Society of the Pacific Conference Series, Vol. 305, Astronomical Society of the Pacific Conference Series, ed. L. A. Balona, H. F. Henrichs, & R. Medupe, 114–+

Hubrig, S., North, P., & Mathys, G. 2000, ApJ, 539, 352

Hui-Bon-Hoa, A. & Alecian, G. 1998, A&A, 332, 224

Jaschek, C. & Jaschek, M. 1967, in Magnetic and Related Stars, ed. R. C. Cameron, 287–+

Joy, A. H. & Abt, H. A. 1974, ApJS, 28, 1

Judge, P. G., Jordan, C., & Rowan-Robinson, M. 1987, MNRAS, 224, 93

Leckrone, D. S. 1973, ApJ, 185, 577

Linsky, J. L. & Haisch, B. M. 1979, ApJ, 229, L27

Lucy, L. B. 1982, ApJ, 255, 286

Lucy, L. B. & White, R. L. 1980, ApJ, 241, 300

Macfarlane, J. J. & Cassinelli, J. P. 1989, ApJ, 347, 1090

Mathys, G. 1989, Fundamentals of Cosmic Physics, 13, 143

Michaud, G. 1970, ApJ, 160, 641

Moore, R. L., Falconer, D. A., Porter, J. G., & Suess, S. T. 1999, Space Science Reviews, 87, 283

Owocki, S. P., Castor, J. I., & Rybicki, G. B. 1988, ApJ, 335, 914

Parker, E. N. 1955, ApJ, 122, 293

Parker, E. N. 1988, ApJ, 330, 474

Parker, E. N. 1990, Advances in Space Research, 10, 17

Pollock, A. M. T. 1987, A&A, 171, 135

Reimers, D. 1982, A&A, 107, 292

Reimers, D., Huensch, M., Schmitt, J. H. M. M., & Toussaint, F. 1996, A&A, 310, 813

Reiners, A. & Basri, G. 2007, ApJ, 656, 1121

Roberts, W. O. 1945, ApJ, 101, 136

Rosner, R., Musielak, Z. E., Cattaneo, F., Moore, R. L., & Suess, S. T. 1995, ApJ, 442, L25

Saar, S. H., Peterchev, A., O'Neal, D., & Neff, J. E. 2001, in Astronomical Society of the Pacific Conference Series, Vol. 223, 11th Cambridge Workshop on Cool Stars, Stellar Systems and the Sun, ed. R. J. Garcia Lopez, R. Rebolo, & M. R. Zapaterio Osorio, 1057–+

Schmitt, J. H. M. M. 1997, A&A, 318, 215

Shimizu, T. & Tsuneta, S. 1997, ApJ, 486, 1045

Simon, T., Ayres, T. R., Redfield, S., & Linsky, J. L. 2002, ApJ, 579, 800

Smith, M. A. 1970, ApJ, 161, 1181

Solanki, S. K., Livingston, W., & Ayres, T. 1994, Science, 263, 64

Strassmeier, K. G. 1996, A&A, 314, 558

Strassmeier, K. G., Hall, D. S., & Henry, G. W. 1994, A&A, 282, 535

Strassmeier, K. G., Rice, J. B., Wehlau, W. H., et al. 1991, A&A, 247, 130

Ud-Doula, A. & Owocki, S. 2003, in Astronomical Society of the Pacific Conference Series, Vol. 305, Astronomical Society of the Pacific Conference Series, ed. L. A. Balona, H. F. Henrichs, & R. Medupe, 343–+

Ud-Doula, A., Townsend, R., & Owocki, S. 2005, in Astronomical Society of the Pacific Conference Series, Vol. 337, The Nature and Evolution of Disks Around Hot Stars, ed. R. Ignace & K. G. Gayley, 319–+

van Rensbergen, W., Hammerschlag-Hensberge, G., & van den Heuvel, E. P. J. 1978, A&A, 64, 131

Vernazza, J. E., Avrett, E. H., & Loeser, R. 1981, ApJS, 45, 635

Wade, G. A. 2004, in IAU Symposium, Vol. 224, The A-Star Puzzle, ed. J. Zverko, J. Ziznovsky, S. J. Adelman, & W. W. Weiss, 235–243

White, R. L. 1985, Revue Scientifique et Technique CECLES CERS, 45

Wilson, O. C. 1978, ApJ, 226, 379

Wright, J. T., Marcy, G. W., Butler, R. P., & Vogt, S. S. 2004, ApJS, 152, 261

Chapter 2

X-ray emission from A-type stars

C. Schröder and J. H. H. M. Schmitt
Astronomy & Astrophysics, 475, 677 (2007)

A&A 475, 677–684 (2007)
DOI: 10.1051/0004-6361:20077429

Astronomy & Astrophysics

X-ray emission from A-type stars⋆

C. Schröder and J. H. M. M. Schmitt

Hamburger Sternwarte, Universität Hamburg, Gojenbergsweg 112, 21029 Hamburg, Germany
e-mail: cschroeder@hs.uni-hamburg.de

Received 7 March 2007 / Accepted 10 September 2007

ABSTRACT

Being fully radiative, stars of spectral type A are not expected to harbor magnetic dynamos and hence such stars are not expected to produce X-ray emission. Indeed, while the X-ray detection rate of such stars in X-ray surveys is low, it is not zero and some of the brighter A-type stars have been detected on different occasions and with different instruments. To study systematically the puzzle of the X-ray emitting A-type stars, we carried out an X-ray study of all A-type stars listed in the Bright Star Catalogue using the ROSAT public data archive. We found a total of 312 bright A-type stars positionally associated with ROSAT X-ray sources; we analyzed the X-ray light curves as well as searched for evidence of RV variations to identify possible late-type companions producing the X-ray emission. In this paper we present a list of X-ray active A-type stars, including the collected data about multiplicity, X-ray luminosity and spectral peculiarities.

Key words. X-rays: stars – stars: activity – stars: coronae – stars: general

1. Introduction

Many if not all late-type, main-sequence stars are surrounded by X-ray emitting coronae. Extensive ROSAT surveys (Schmitt & Liefke 2004) show that the X-ray detection rates among the brighter late-type stars with spectral type F and later are approaching 100%; the same holds for early-type stars surveyed by Berghöfer et al. (1996, 1997), although the X-ray production mechanisms in the early-type stars is thought to be fundamentally different from that in late-type stars. The X-ray production mechanism for the late-type stars is believed to be similar to that of the Sun, and indeed, the dramatic increase in X-ray detection rates for stars thought to possess surface convection zones lends support to the idea that the stellar magnetism, which is ultimately held responsible for the observed activity phenomena, is generated in the turbulent outer layers of late-type stars. Early-type stars on the other hand produce strong radiatively driven winds, and instabilities in these winds are thought to be ultimately responsible for the ubiquitous X-ray emission observed from these stars. A general paucity of X-ray emission among (late-type) B- and especially A-type stars has been noticed ever since the days of the *Einstein Observatory* (Schmitt et al. 1985). Since A-type stars have neither convection zones nor do they have – at least – strong winds, none of the X-ray production mechanisms operating in early- or late-type stars ought to be operating and therefore A-type stars are "expected" to be intrinsically X-ray dark.

This expectation of intrinsic X-ray darkness/weakness is borne out by the available X-ray data on nearby A-type stars. The nearest A-type stars are Sirius and Vega, but the signals seen in the ROSAT X-ray detectors (especially the ROSAT-HRI) are in all likelihood produced by UV-radiation rather than genuine X-ray radiation (Zombeck et al. 1997; Berghöfer et al. 1999). A further, and more severe problem for the interpretation of X-ray data from A-type stars is binarity. Because of the ubiquity of X-ray emission among late-type stars, all A-type stars with a late-type companion should be X-ray sources, which are simply attributable to the presence of late-type companions. Since such optically, possibly quite faint, companions are easy to hide in the vicinity of an optically bright A-type star, the X-ray emission from even presumably single A-type stars could in fact attributed to previously unknown late-type companions. Because of the rather short main sequence life times of A-type stars late-type companions of such stars are still considered young, hence most of the "hidden" late-type companions are expected to be X-ray bright and active sources.

One of the unique attributions of the observed X-ray emission in a stellar system is quite difficult; it requires X-ray data with sufficient angular resolution, which would actually still be insufficient to rule out close companions. Stelzer et al. (2006) used Chandra imaging observations to spatially resolve a sample of main sequence B-type stars with recently discovered companions at arcsecond separation. They found that all spatially resolved companions are X-ray emitters, but – somewhat surprisingly – seven out of eleven B-type stars were also found to be X-ray sources. Obviously this result still does not rule out additional close companions of the B stars in the system, but would imply a rather large binary frequency of intermediate-mass stars and a high number of systems with more than two components.

Another technique is observing systems with a special viewing geometry such as an eclipsing binary. Schmitt & Kürster (1993) and Schmitt (1998) studied the (totally) eclipsing binary α CrB, consisting of an A0V primary and a G2V secondary. At secondary optical minimum with the optically bright A-type star in front of the optically fainter G-type star a total X-ray eclipse was observed, thus demonstrating, first, that the A-type primary is indeed X-ray dark "as expected", and second, that the size of the X-ray corona around the secondary is at least smaller than the size of the primary.

In a few other cases, the correct attribution of observed X-ray emission from A-type stars can be made using the spectral

⋆ Tables 2 et 3 are only available in electronic form at http://www.aanda.org

information contained in the X-ray data. In the prototypical case β Crt (Fleming et al. 1991) the soft PSPC spectrum suggested the presence of an X-ray emitting white dwarf, which was subsequently confirmed (Barstow et al. 1994; Vennes et al. 1998). Thus β Crt is very similar to the binary system Sirius AB with its prototypical white dwarf; if this system was ten times further away from the Sun, it would still be quite X-ray bright, but the B component would be almost impossible to detect at least at optical wavelengths.

Obviously the set of – for whatever reasons – X-ray bright A-type stars is a bewildering zoo of quite different beasts. The purpose of this paper is to provide a definitive summary of the ROSAT observations of bright A-type stars. If the puzzle of X-ray emitting A-type stars is ever to be solved, a well defined sample of the brightest of such objects is required. The X-ray emitting A-type stars were detected and identified and an extensive literature search was carried out to single out those objects whose X-ray emission cannot be explained by emission from late-type companions, at least with the currently available information on these objects.

2. Observations and data analysis

2.1. Data basis

The ROSAT Observatory was operated between 1990–1998. Between July 1990 and January 1991 it carried out its ROSAT All-Sky Survey (RASS) with the ROSAT Position Sensitive Proportional Counter (PSPC). Afterwards pointed observations of individual objects were carried out within the framework of the ROSAT guest investigator program both with the PSPC and a High (angular) Resolution Imager (HRI). These detectors had fields of view of about 7000 arcmin^2 for the PSPC and 1000 arcmin^2 for the HRI, so that many X-ray sources were picked up serendipitously in the field of view of many observations, whose original scientific goal was actually quite different.

2.1.1. X-ray data

The results of both the RASS observations and the ROSAT pointed observations are available in the ROSAT results archive in the form of source lists. Four of the five catalogs were used for the present study, i.e., the ROSAT Bright Source and Faint Source Catalog, the Second ROSAT Source Catalog of Pointed Observations with the PSPC and the First ROSAT Source Catalog of Pointed Observations with the HRI. These catalogs as well as detailed information on the detection and screening procedures applied in the construction of the catalogs are available via www from the ROSAT Home Page at Max-Planck-Institut für extraterrestrische Physik (`http://wave.xray.mpe.mpg.de/rosat/catalogue`) or its mirror sites. Altogether, these catalogs contain 372 896 entries. From the data provided by these catalogs we extracted position and count rates of those sources, which can be positionally associated with bright A-type stars. For those sources observed with the PSPC with the RASS, we used the X-ray luminosities derived by Hünsch et al. (1998).

2.1.2. Optical data

As our source of optical data we used the 5th version of the Bright Star Catalog (BSC) by Hoffleit & Jaschek (1991), which contains 9110 objects of magnitude 6.5 or brighter. For the parallax values we used the data given in the Hipparcos database. Out of those 9110 objects, 1966 stars are listed as A-type stars in the BSC. The BSC thus constitutes a very large and complete database of bright A-type stars with a lot of auxiliary information about its entries. For information concerning possible hidden late-type companions of the A-type stars we used the SIMBAD database extensively.

2.1.3. Catalogs

The catalogs in Tables 2 and 3 present the main result of our efforts; in Table 2 we provide optical and X-ray data of 84 detected "bona fide" single A-type stars as contained in the BSC. Table 3 shows the same data for 228 X-ray associated A-type stars that are members of known binary or multiple systems or show signs of hidden companions. The columns of the table contain the following information:

Col. 1: HR number, taken from the BSC;
Col. 2: binary flag; S means single star, B visual or eclipsing binary, SB spectroscopic binary, PB potential binary;
Col. 3: rotational velocity in km s^{-1};
Col. 4: separation for visual binary systems;
Col. 5: difference in the magnitude between the A star and its closest companion;
Col. 6: MK spectral types of the components;
Col. 7: distance of the star as given by Hipparcos parallaxes;
Col. 8: catalog flag indicating in which observation mode the star has been observed; r means ROSAT all-sky survey, p PSPC pointing and h HRI pointing;
Col. 9: mean count rate of the associated X-ray source; first choice were PSPC pointing source data, second HRI and third survey observation data;
Col. 10: error of the count rate; errors with a value of 0.0 mark sources with flags in the ROSAT catalogs that indicate a suspect source or false detection in the field;
Col. 11: X-ray luminosity derived from the distance as given in Col. 7 and the count rates as given in Col. 9. The values are given in units of 10^{27} erg/s.

2.2. Data analysis

2.2.1. Correlation of the catalogs

For the correlation between the X-ray and the optical source lists we combined the ROSAT Faint Source Catalog and the ROSAT Bright Source Catalog to the RASS catalog. The resulting three X-ray catalogs and the Bright Star Catalog were searched for positional coincidences. As a matching criterion we used 90 arcsec for survey data, 36 arcsec for pointing data with the PSPC and 18 arcsec for HRI data. The differently chosen positional acceptance thresholds reflect the fact that the intrinsic positional accuracy of survey data, and the PSPC and HRI pointing data increases in that order. In Fig. 1 we plot histograms showing the number of sources obtained by our positional correlation analysis as a function of angular distance. The concentration of the sources towards the target positions, i.e., the 1966 A-type stars in the BSC catalog, is obvious. As shown in Fig. 1 the matching criteria approximately mark the distances at which the probability of obtaining a spurious X-ray source becomes greater than the chance to obtain a correct identification. Therefore the chosen values for the acceptance thresholds do not introduce significant errors into our list of seemingly X-ray active A-type stars.

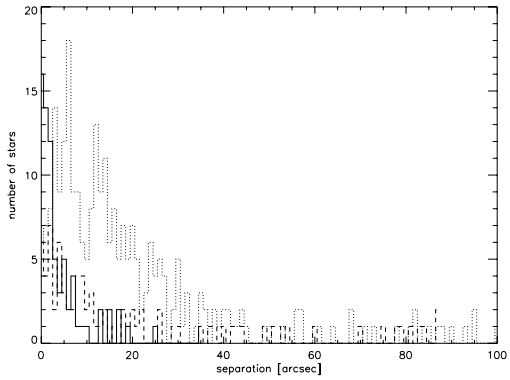

Fig. 1. Number of A-type stars at a given separation between the optical position of the star and the position of the associated X-ray source. The dotted line shows the data for the BSC-RASS correlation, the dashed line represents the BSC-PSPC data and the solid line those from the BSC-HRI correlation.

2.2.2. Search for late-type companions

The most common explanation for seemingly X-ray active A-type stars is to assume that the X-ray emission does not originate from the A-type star itself but rather from a low mass (binary) companion. To check this hypothesis we searched for signatures of hidden companions in four ways. First, we examined possible variations in the radial velocity and proper motion of the A-type star given in the SIMBAD database and accordant papers. Second, we checked the ROSAT X-ray light curves for flare-like variations which might be an indicator of the presence of a late-type companion. Third, for those stars observed in more than one observation mode we performed a comparison of the count rates in the different observations to check for long time scale variability. Different count rates at the two different observation times are an indicator for a variable source and therefore hint at the presence of a hidden companion. Admittedly, the significance of this indicator is small, since the possible mechanisms for the X-ray emission from A-type star are somewhat speculative. Finally, another, albeit only weak, indicator is the rotational velocity of the A-type star itself. Given enough time to synchronize their orbits, the members of a binary system would rotate slowly and a high rotational velocity might therefore indicate a single star or a young binary system. The results of these tests are included in our list of seemingly X-ray active A-type stars. Stars without any available information on binarity and no signatures of hidden companions we consider as bona fide single stars.

3. Results

On basis of the correlation of the Bright Star Catalogue and the three ROSAT catalogs we can associate 312 of the 1966 A-type stars with one or more X-ray sources. In total, 272 of these sources are listed as RASS detected X-ray sources, 63 sources are listed in the PSPC pointing catalog and 69 have been observed at the highest possible angular resolution with the ROSAT HRI. The total number of these sources is larger than 312 because some stars have been detected in more than one mode/instrument.

Table 1. Statistics of spectral peculiar A-stars.

	Total	X-ray detected	Known binaries	Binaries among X-ray detections
A-type stars	1966	312 (16%)	733 (37%)	194 (62%)
Am	212	41 (19%)	89 (42%)	34 (83%)
Ap	133	18 (14%)	51 (38%)	8 (44%)
A giants	474	62 (13%)	179 (38%)	35 (56%)

3.1. Spurious identifications

We stress that all our X-ray source identifications are obtained solely on the basis of positional coincidence. Despite of this we expect the number of spurious identifications to be very small. Calculating the number of identifications obtained by distributing approximately 120 000 RASS sources over 1966 positions (i.e., the number of A-type stars contained in the BSC) with a detected cell radius of 90 arcsec results in 11 spurious identifications or 4% of the total number of RASS detections of A-type stars. The actual distribution of position offsets is much narrower (cf., Fig. 1). To be specific, only 4 out of our 272 survey detections have position offsets of more than 50 arcsec, and only 11 X-ray detections are off by more than 30 arcsec from the optical positions of the A-type star. We thus conclude that the fraction of incorrectly identified X-ray emitters in our sample is at the one to two percent level and that the overwhelming majority of our sources are correctly identified with an optically bright A-type star.

3.2. Detection statistics

Next we divide the 1966 A-type stars as listed in the BSC into four subgroups according to their spectral features: Am, Ap, giant and main sequence stars. To check whether the X-ray activity of A-type stars depends on this grouping we determined the fraction of X-ray active stars in all of the different subgroups. In Table 1 we list the total number of A-type stars, the number of seemingly X-ray active stars, the number of known binary or multiple systems and the binary frequency among the X-ray active stars.

Given the count statistics there are obviously no significant differences in the fraction of X-ray active stars between the different subgroups. However, the X-ray detection rates among the known binaries are larger than the binary fraction in the corresponding subsamples. We interpret this strong increase of the binary frequency in the X-ray active subsamples as an indicator for a larger number of binary systems. These systems, which can be optically separated in quite a number of cases, cannot be separated in the ROSAT X-ray data and therefore cause possibly false correlations between the A-type star and the X-ray source (i.e. the companion). Clearly, the number of known binaries among all A-type stars has to be considered a lower limit. While the sample of seemingly X-ray active stars was intensively searched for signatures of binarity, the remaining 1654 A-type stars, which have not been detected in X-rays, have been classified only according to the multiplicity information given in the BSC.

3.3. Detection rate vs. spectral type

In Fig. 2 we plot the detection rate of A-type stars vs. spectral type. As is obvious from Fig. 2, the mean percentage of X-ray

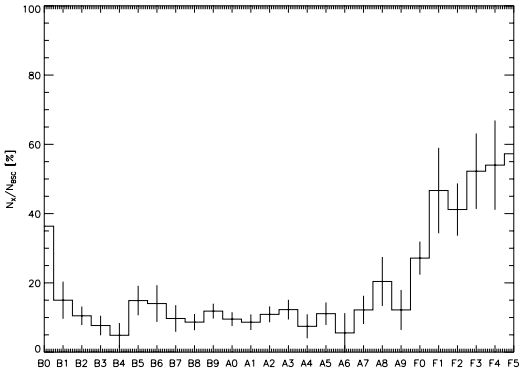

Fig. 2. Percentage of X-ray active stars N_x from the total number of stars N_{BSC} of a given spectral type. Note the strong increase in the X-ray detection rates for stars in the range A9–F3.

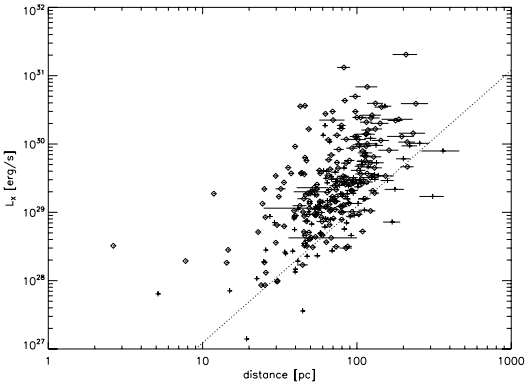

Fig. 3. L_x vs. distance for the 312 A-type stars associated with a ROSAT X-ray source. The crosses indicate single stars, and the diamonds known or possible multiple systems. The dotted line represents the typical detection limit for the RASS observations, i.e., $f_X \approx 10^{-13}$ erg cm^{-2} s^{-1}.

active stars among the stars with spectral type A0 to A9 is 10% to 15%. This is consistent with the X-ray activity frequency in the above mentioned special subgroups in Table 1. The onset of convection and hence the presumed onset of an $\alpha\Omega$ − dynamo at spectral type A9–F3 and the radiation driven winds at early B-type stars are clearly visible. The fact that less than 60% of the F5 stars are X-ray active in our data we attribute to the flux limit of the X-ray data; if instead, one considers a volume-limited sample of F-type stars (Schmitt & Liefke 2004), one finds a detection rate of essentially 100%.

3.4. X-ray luminosity

Figure 3 shows the X-ray luminosity of the ROSAT sources associated with the 312 X-ray detected A-type stars as a function of stellar distance; the parallaxes for the stars have been taken from the Hipparcos catalog (ESA 1997). The two objects with the faintest X-ray sources are the AV5 star β Pictoris (HD 39060) and the AV7 star δ Doradus (HD 39014). In the case of β Pictoris the recorded ROSAT HRI signal is completely consistent with being due to UV contamination (Hempel et al. 2005), in the case of δ Doradus this is extremely likely. Berghöfer et al. (1999) derived a relation between the U, B and V magnitudes and the HRI count rates. The predicted count rate for δ Doradus of 0.24 cts/ks corresponds to the observed HRI count rate of 0.63 cts/ks within the errors. The dotted line represents the typical detection limit for the RASS observations, i.e., $f_X \approx 10^{-13}$ erg cm^{-2} s^{-1}. Sources with a lower L_X have been observed with the PSPC or HRI via pointing mode, resulting in deeper observations with lower detection limits. Figure 3 suggests the single and double stars from our X-ray detected sample do not possess significantly different X-ray luminosities as a function of distance.

The distribution functions of the X-ray luminosities of single and binary stars are shown in Fig. 4. Carrying out a formal test with a one-sided Kolmogorov-Smirnov test allows us to reject the null hypothesis that in both classes the X-ray originate from the same population, with a significance of 95%, according to a maximum difference of 0.158 between the two distributions. Additional bootstrap tests with two artificial samples of randomly chosen X-ray detected stars and the same size as the original samples do not support this high level of significance. Out of 10 000 runs 2127 show distributions in which the maximum difference between the distributions is larger than the measured value of 0.158, hence the bootstrap test suggests only an 80% confidence for the rejection of the hypothesis that the two samples originate from the same population. We note that the offset in the cumulative distribution function might be a result of a observational bias. The problem is that binary systems with an A-type star and a low mass companion are harder to resolve than systems with a higher mass companion and therefore more likely to be misidentified as a single star. For solar-like companions this would create a "single star" sample with lower X-ray luminosity, since L_X scales with L_{bol}. This effect might be negated by the fact that for M-type stars, especially young ones which are to be expected in binary systems with A-type stars, the difference in X-ray luminosity vanishes (Stauffer et al. 1994; Stern et al. 1995; Randich et al. 1996).

3.5. Completeness

Since the absolute magnitudes of our sample stars vary quite a lot, our sample is definitely not volume-limited. Considering a distance limit of 50 parsecs our sample is definitely complete in the sense that all A-type stars up to that distance are sample members. Furthermore, since from the typical RASS flux limit we can compute the RASS upper X-ray luminosity limit of $ul = 2.4 \times 10^{25} \times d_{pc}2$ erg/s, which translates into an X-ray luminosity of $L_X = 6 \times 10^{28}$ erg/s, and thus the X-ray luminosity distribution faction above that limit is unaffected by any non-detections. In the 50 pc volume there are 220 cataloged A-type stars, out of which 82 (or 37%) are associated with an X-ray source; in other words, the observed detection rate in a volume-limited sample of A-type stars significantly exceeds 15%. The upper limits to the X-ray luminosity of most of the 138 non-detections are in the range $\approx 10^{28}$ erg/s for the RASS data; a few nearby A-type stars with upper limits from dedicated pointings (Schmitt 1997; Pease et al. 2006) have upper limits considerably below this value; these stars include α Lyr (A0V), β Leo (A3V) and α PsA (A3V). Out of these 82 X-ray detcted stars, 60 objects (or 73% of the X-ray detected stars) are known or supposed to have one or more companions, while 22 stars (or 27%) of the X-ray detected stars are "bona fide" single stars. The cumulative

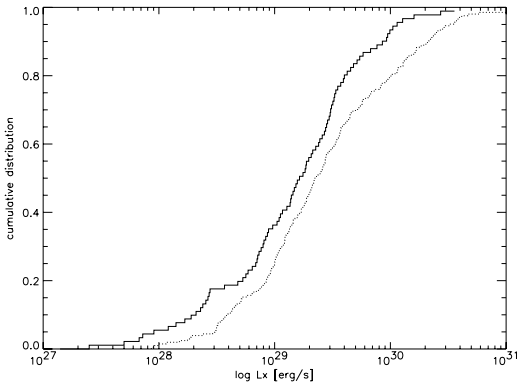

Fig. 4. Cumulative distribution function of the X-ray luminosity for the single star sample (solid line) and binary star sample (dotted line). The null hypothesis that both samples originate from the same distribution can be rejected with a significance of 95%.

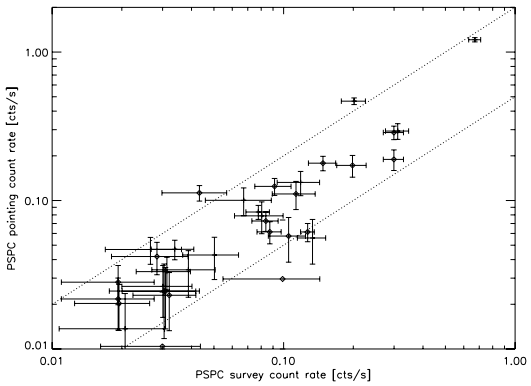

Fig. 5. Comparison of X-ray count rates for 35 stars detected both in the all-sky survey and the PSPC pointing program. The two dotted lines indicate a factor 2 variation from unity. Single and double stars are represented by crosses and diamonds respectively. Stars with large deviations from the regression line are identified.

distribution functions of the 22 single stars and 60 known binary stars shows a comparable offset as the samples presented in Sect. 3.5, they do of course, suffer from the same possible bias(es). Thus we conclude that a volume-limited sample yields similar properties for X-ray detected A-type stars, except that the true detection rate maybe quite a bit higher.

3.6. Variability between survey and pointing data

For some of our sample stars multiple X-ray detections are available from RASS data, the ROSAT PSPC pointing or HRI pointing program. The time span between survey and pointed observations with the PSPC is typically of the order of 1–2 years with larger time spans between the survey and the pointed observations carried out with the HRI instrument.

In Fig. 5 we plot the PSPC count rate observed during the all-sky survey vs. the PSPC count rate observed during the pointing program in a double-logarithmic representation for those of our sample stars detected in both observing modes. The two dotted lines indicate a factor of two deviation above and below unity. As Fig. 5 shows, all count rates lie within this area according to their error bars. Variations by a factor of 4 are not uncommon for active late-type stars and would therefore support the late-type companion hypothesis, as does the fact that there is no significant difference in the variability of single and binary stars.

The variability between the count rates obtained during the PSPC pointed observations and the HRI pointed observations is shown in Fig. 6. Again, the dotted lines mark a factor of two deviation above and below "unity"; "unity" in this case accounts for the fact that the ROSAT-HRI instrument is less sensitive than the ROSAT-PSPC leading to an HRI count rate typically a quarter of the PSPC count rate. Only HR 5999 shows a variation in count rate differing by a factor of 12; however, we suspect that the X-ray emission originates from the possible T Tauri star Rossiter 3930, which is separated to HR 5999 by 1.3″ (Zinnecker & Preibisch 1994; Stecklum et al. 1995), also, HR 5999 lies in a crowded field not resolved in the survey data.

Figure 7 shows the third possible combination of the three catalog data sets, the comparison of the count rates obtained during the PSPC survey program and the HRI pointing program. As in Fig. 6, the dotted line indicates "unity" which takes into account the lower sensitivity of the ROSAT-HRI instrument. Five stars show apparent count rate variations. HR 1189 is a binary system with a separation of 8″, containing an A1V and a late B-type star. Due to the fact that the survey observation has an exposure time of only 70 s, it is most likely that the variation originates from the uncertainty in the count rate of the RASS source. HR 2890 (Castor B) is a spectroscopic binary with spectral types of A5Vm and early M (Gudel & Schmitt 1996). Closeby, with a separation of 3.9″, lies the spectroscopic binary system Castor A, which is composed of an A1V and a late K-star. Due to the configuration of these two binary systems the X-ray emission and its variability can be clearly associated with the late-type companions of the A-type stars (Güdel et al. 2001). HR 3524 (RS Cha) is an eclipsing binary consisting of two A8V stars (Andersen 1975). In contrast to earlier publications, Mamajek et al. (2000) derived ages of 5.0×106 and 4.3×106 yr for the two components and suggest that this system, because of the fact that the X-ray emission of RS Cha shows flare-like variations, is actually a triple system with an undetected T Tauri star. According to the Washington Visual Double Star Catalog, HR 8662 is a visual binary with a separation of 10.5″ and additionally the A component is a spectroscopic binary. Corbally (1994) specifies the spectral type of the B component as G9V, thus giving a likely explanation for the count rate variations, keeping in mind the resolving power during the survey observations.

3.7. Individual objects of pointed HRI observations

In the following we present some ROSAT HRI observations of X-ray detected A-type stars for which PSPC and high resolution ROSAT HRI observations are available. Additionally, detailed information about these stars has been published in different papers and might give hints about the absence or presence of undetected late-type companions.

All of the HRI observations presented here show very small deviations between the optical position of the A-type star and the position of the associated X-ray source. The values range from less than 1″ to 5″ which is less than the spatial resolution of the HRI. All of the discussed stars are single stars or binary systems with a separation which is large enough to be resolved by the

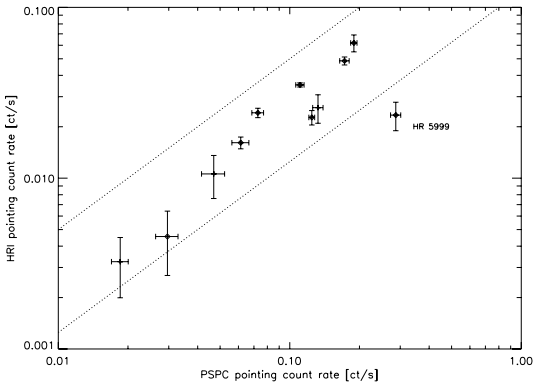

Fig. 6. Comparison of X-ray count rates for 14 stars detected both in the PSPC pointing program and the HRI pointing program. The two dotted lines indicate a factor 2 variation from unity. Single and double stars are represented by crosses and diamonds respectively. Stars with large deviations from the regression line are identified.

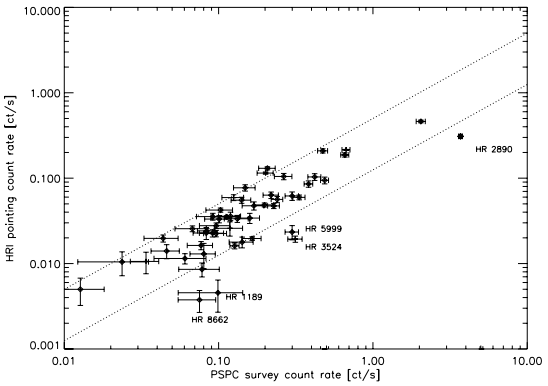

Fig. 7. Comparison of X-ray count rates for 55 stars detected both in the PSPC survey program and the HRI pointing program. The two dotted lines indicate a factor 2 variation from unity. Single and double stars are represented by crosses and diamonds respectively. Stars with large deviations from the regression line are identified.

HRI. Objects with associated X-ray source near the edge of the detector, and therefore less accurate positions, are also excluded.

3.7.1. HR 191

This system is a visual binary with a separation of 19.8″, according to the Washington Visual Double Star Catalog, with spectral types of A0IV and K2-5V. Two HRI observations of HR 191 have been carried out, one in 1991 with an exposure time of 2.1 ks and a second in 1995 with 5.3 ks. Both observations show a weak X-ray source near the position of HR 191. While the K-star could not be detected in the first observation in 1991, a weak source is found at the position of the K-star in 1995, possibly due to a flare. The positional deviations of the X-ray sources with respect to their optical counterparts are less than one arcsecond for both stars. Unfortunately, the count rate of the A-star associated source is too low and the exposure time is too short for a significant statistical test for variability, which would be an indicator for the presence of a hidden late-type companion. The X-ray luminosity of 1.7×10^{29} erg/s is in the range that can be explained by an active late-type companion and indeed, Gerbaldi et al. (1999) mention this star as a possible astrometric binary.

3.7.2. HR 433

As for the previous system, HR 433 is a binary system composed of an A0V and an early K-star. The separation is 22″ and the deviation of the position of the X-ray source from the A-type star is about 5″. Only one source was found in the X-ray observations with an exposure time of 4.8 ks. While an X-ray luminosity of 1.1×10^{29} erg/s is clearly consistent with an active late-type star, the statistical variability tests show no significant signature of variability, which would have indicated such a hidden active late-type star. The values for the radial velocity vary from −7 to 12 km s^{-1}, and this might be a hint for a yet undetected companion.

3.7.3. HR 778

The Hipparcos Catalog lists this A6V star as a potential astrometric binary with a short period, but no other publication gives any information about a possible companion. The only X-ray source in the HRI image is separated from the optical position of the A-type by less than one arcsecond. During the observations, which took place in July 1997 (5.4 ks) and December 1997 and January 1998 (27.6 ks combined) the L_X of 1.7×10^{28} erg/s led to count rates which were too low for statistical tests of variability. The two measurements of the radial velocity give consistent values of 3 km s^{-1}.

3.7.4. HR 789

HR 789 is again a visual binary system consisting of A2V primary accompanied by an early M dwarf with a separation of 24″. The ROSAT HRI image with an exposure time of 1.5 ks, presented in Fig. 8., clearly shows two X-ray sources at the optical positions of the stars, with the brighter X-ray source being associated with the position of the A-type star. While the Kolmogorov test showed no clear signs of variability, an additional χ^2 test gives a probability of less than 5% that this source is constant. The L_x of 9.2×10^{29} erg/s is consistent with an active late-type star. The rotational velocity of 190 km s^{-1} contradicts a synchronously rotating companion, but Buscombe & Morris (1961) found variations in the radial velocity leading to the possibility of a non-synchronously rotating companion.

3.7.5. HR 2174

This A3V star is a member of a triple system with its closest companion at a distance of 29.2″. Only one source was found near the optical position of the A-type star. During the two HRI observations in March 1995 (1.8 ks) and March 1996 (3.8 ks) this X-ray source has a deviation of one and two arcseconds to the optical position of HR 2174 and is therefore associated with the A-type star. As in the two cases mentioned above, the count rates are too low and the exposure times are too short to allow any significant statements about the variability of the X-ray

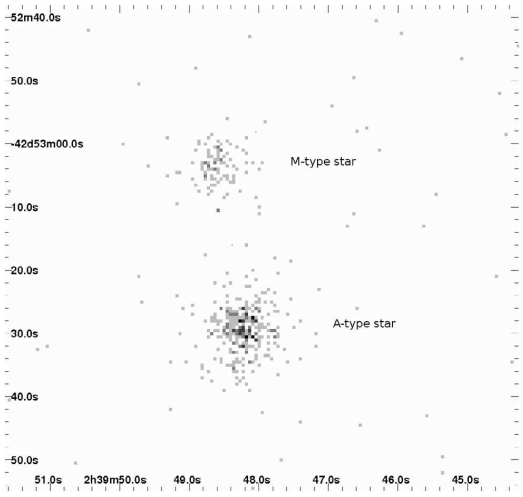

Fig. 8. ROSAT-HRI image of HR 789. The separation between the brighter X-ray source and the optical position of the A-type star is about an arcsecond.

source. With 2.3×10^{30} erg/s the X-ray luminosity is at the upper limit for late-type stars. The fast rotational and constant radial velocity are indicators against an undetected companion.

3.7.6. HR 3321

This star is an A5III-IV star with no known companion. The HRI observations took place during April 1998 and show one X-ray source, separated by 3″ from the optical position of HR 3321. The combined exposure time of the three observation blocks is 6.4 ks. The statistical test shows a significant variability during one of these observations. Additionally, the value of the rotational velocity is 11 km s^{-1} and therefore too low to be an indicator against a late-type companion. The radial velocity is constant at a value of 27.3 km s^{-1}.

3.7.7. HR 6681

This A0V star is a member of a triple system with a separation of 20.8″ from its closest companion, most likely an early G-type star. In the ROSAT HRI observations with an exposure time of 2.9 ks carried out in September 1994, two X-ray sources with a separation of 16″ are visible and the position of the brighter X-ray source agrees with the optical position of the A-type star to better than 3″. The statistical test showed no significant signs for or against variability and measurements of the radial velocity have not been carried out so far.

3.7.8. HR 8463

HR 8463 is an A5V star and a member of a quadruple system with a separation of 23.2″ from its nearest companion. Two X-ray sources are detected in the vicinity of the A-type star and the weaker source has a deviation of less than an arcsecond to the optical position of the A-type star. The observation is divided in four parts with a total exposure time of 6.4 ks; in three of them statistical tests do not show any signs of variability and in the forth one the tests do not give a significant result. With a distance of 55 pc and a count rate of 0.021 ± 0.002 cts/s the L_X amounts to 1.8×10^{29} erg/s. The varying values for the radial velocity of −2 to −16.2 km s^{-1} might be an indicator for a companion.

3.8. Further comments on HRI observations

From the six known and optically separated binary systems two companions have not been found in the observations, even though the separation of the stars is large enough to be resolved by the HRI. The reason for this is most likely the fact that at a distance of 67 pc in the case of HR 433 and 186 pc for HR 2174 late-type stars are hardly detectable, even in a very active state.

HR 2015 is a single star separated from a X-ray source by less than 3″. This source is listed in the HRI catalog but could not be found by our source-detection routines. We therefore flagged HR 2015 as an uncertain candidate and excluded it from the previous discussion.

4. Summary and conclusion

The correlation of the Bright Star Catalogue with the ROSAT X-ray catalogs results in a list of 312 bright A-type stars which can be positionally associated with an X-ray source. The overall ROSAT detection rate of bright A-type stars lies between 10–15% in the spectral range A0–A9, with a steep increase in detection rates among F-type stars. Those 312 A-type stars whose associated X-ray sources are listed in the ROSAT all-sky survey or the pointed observations catalog have been further investigated for signatures of the presence of late-type companions.

As a result of the evaluation of the distribution of seemingly X-ray active stars in the different spectral subgroups it is obvious that there is neither a connection between the spectral type and the frequency of X-ray active stars nor an indication for a connection between spectral peculiarities and X-ray activity. On closer inspection, this is no real surprise. Due to the fact that a significant portion of the observed X-ray emission comes, without much doubt, from late-type companions and these companions are distributed equally on the different spectral classes, a concentration of X-ray activity on a few spectral classes would indeed be astonishing. Otherwise an increased X-ray frequency in a group of spectral peculiar stars would have given a hint about a possible mechanism for X-ray production, such as in the magnetically-confined wind shock model proposed by Babel & Montmerle (1997). Actually none of these subgroups showed an significant increase in the X-ray detection frequency.

The examination of the count rates showed that most of the sources lack sufficient signal to obtain unambiguous results in a variability analysis. The reason for this is the fact that most of the available HRI observations are short snapshots of up to 5 ksec to check if the target is X-ray active at all. Of the presented individual candidates, only the lightcurves of HR 789 and HR 3321 showed significant signs of variability while the lightcurve of HR 8463 was constant in three of four observation periods. We mention in passing that even clear signs of variability do not rule out the possibility that the X-ray source is the A star itself. Due to the absence of a conclusive theory for an X-ray producing mechanism at A-type stars, it is hard to predict if the A stars are variable X-ray sources or not.

For many of the X-ray detected A-type stars, information on binarity exists in partly ambiguous and partly unambiguous forms. A total of 84 of the detected X-ray stars are, however, either bona fide single stars (meaning that no information on binarity and no indications of hidden companions are available),

or resolved multiple stars, implying that at least a third system component must exist, if the X-ray emission is not attributed to the A-type star. These 84 bona fide single stars are therefore particularly well suited candidates for follow-up observations, for example, for high resolution X-ray and IR observations to separate the suggested companion from the A-type star or radial velocity monitoring to search for companions. The list presented here may serve as a starting point for such a project.

References

Andersen, J. 1975, A&A, 44, 445
Babel, J., & Montmerle, T. 1997, A&A, 323, 121
Barstow, M. A., Holberg, J. B., Fleming, T. A., et al. 1994, MNRAS, 270, 499
Berghöfer, T. W., Schmitt, J. H. M. M., & Cassinelli, J. P. 1996, A&AS, 118, 481
Berghöfer, T. W., Schmitt, J. H. M. M., Danner, R., & Cassinelli, J. P. 1997, A&A, 322, 167
Berghöfer, T. W., Schmitt, J. H. M. M., & Hünsch, M. 1999, A&A, 342, L17
Buscombe, W., & Morris, P. M. 1961, MNRAS, 123, 233
Corbally, C. J. 1994, VizieR Online Data Catalog, 3117, 0
ESA 1997, VizieR Online Data Catalog, 1239, 0
Fleming, T. A., Schmitt, J. H. M. M., Barstow, M. A., & Mittaz, J. P. D. 1991, A&A, 246, L47
Gerbaldi, M., Faraggiana, R., Burnage, R., et al. 1999, A&AS, 137, 273
Gudel, M., & Schmitt, J. B. M. M. 1996, in Radio Emission from the Stars and the Sun, ed. A. R. Taylor, & J. M. Paredes, ASP Conf. Ser., 93, 315
Güdel, M., Audard, M., Magee, H., et al. 2001, A&A, 365, L344
Hamaguchi, K., Yamauchi, S., & Koyama, K. 2005, ApJ, 618, 360
Hempel, M., Robrade, J., Ness, J.-U., & Schmitt, J. H. M. M. 2005, A&A, 440, 727
Hoffleit, D., & Jaschek, C. 1991, The Bright star catalogue (New Haven, Conn.: Yale University Observatory), 5th rev. Ed., ed. D. Hoffleit, & C. Jaschek,
Mamajek, E. E., Lawson, W. A., & Feigelson, E. D. 2000, ApJ, 544, 356
Pease, D. O., Drake, J. J., & Kashyap, V. L. 2006, ApJ, 636, 426
Randich, S., Schmitt, J. H. M. M., Prosser, C. F., & Stauffer, J. R. 1996, A&A, 305, 785
Schmitt, J. H. M. M. 1997, A&A, 318, 215
Schmitt, J. H. M. M. 1998, A&A, 333, 199
Schmitt, J. H. M. M., & Kürster, M. 1993, Science, 262, 215
Schmitt, J. H. M. M., & Liefke, C. 2004, A&A, 417, 651
Schmitt, J. H. M. M., Golub, L., Harnden, Jr., F. R., et al. 1985, ApJ, 290, 307
Simon, T., Drake, S. A., & Kim, P. D. 1995, PASP, 107, 1034
Stauffer, J. R., Caillault, J.-P., Gagne, M., Prosser, C. F., & Hartmann, L. W. 1994, ApJS, 91, 625
Stecklum, B., Eckart, A., Henning, T., & Loewe, M. 1995, A&A, 296, 463
Stelzer, B., Huélamo, N., Micela, G., & Hubrig, S. 2006, A&A, 452, 1001
Stern, R. A., Schmitt, J. H. M. M., & Kahabka, P. T. 1995, ApJ, 448, 683
Vennes, S., Christian, D. J., & Thorstensen, J. R. 1998, ApJ, 502, 763
Zinnecker, H., & Preibisch, T. 1994, A&A, 292, 152
Zombeck, M. V., Barbera, M., Collura, A., & Murray, S. S. 1997, ApJ, 487, L69

C. Schröder and J. H. M. M. Schmitt: X-ray emission from A-type stars, *Online Material p 1*

Online Material

C. Schröder and J. H. M. M. Schmitt: X-ray emission from A-type stars, *Online Material p 2*

Table 2. List of X-ray associated "bona fide" single or resolved multiple A-type stars.

HR	Binary	$v \sin(i)$	Sep.	δ Mag	Components	Distance	Catalog			CR	±CR	L_{x27}
191	B		20	7	A0IV+K2-5V	74	R		H	0.01147	0.00158	270
378	S	100–112			A3V	67	R			0.01713	0.00787	78.3
398	S				A0Vnn	158	R			0.01228	0.00537	292.1
433	B		22	5	A0V+K0V	68	R		H	0.00856	0.00159	353.3
710	B	23–31	12	3.5	A6Vsp+G5-8V	66	R		H	0.03550	0.00327	422.6
778	PB				A6V	44		P	H	0.01851	0.00154	21
789	B		24	10	A2V+M2-5V	40	R		H	0.2090	0.01200	924
817	S				A1V	107	R			0.04391	0.01295	554.6
943	S	80–90			A5V	58	R			0.04234	0.01681	137.9
1014	S	79			A3V	58		P		0.02082	0.00226	50.2
1039	S	65			A0Vs	104	R			0.03048	0.01085	299.9
1196	S	35–44			A5m	60	R			0.04111	0.01120	141.0
1314	S	230–249			A2Vn	108	R			0.03234	0.00957	498.5
1700	S				A1V	130	R			0.01966	0.00737	358.0
1706	B		12.6/14.6	6/3	A9IV+K2+F+WD	82	R		H	5.051	0.1068	13211.6
1732	S	40–49			A0pSi	137		P		0.02576	0.00168	343.7
1940	S	14-15			A8Vs	41	R			0.01679	0.00761	19.2
2174	B		29.2/..	1.2/3.2	A3V+A0	187	R		H	0.02279	0.00366	3351
2180	S	225–264			A0Vn	78	R			0.02316	0.00804	185.8
2209	S	220–238			A0Vn	54	R			0.04748	0.01412	120.4
2265	S	249			A2-3V	62	R			0.5004	0.02675	1858.1
2350	S				A5V	69		P		0.00796	0.00059	27.3
2351	S	35–44			A9IV	61	R	P		0.05592	0.0	402.3
2658	S				A0V	125	R			0.02326	0.00855	329.1
2683	S				A0pSi	87	R			0.02306	0.00863	186.7
2709	S	62			A0III	255	R			0.02186	0.00799	1023.4
2720	S				A8V	48	R			0.05062	0.01390	74.6
2776	S	83–94			A7s	34	R			0.03516	0.01172	24.8
2869	S	214			A1IV	106	R			0.02414	0.01043	267.7
3131	S	177–245			A1V	73	R			0.03230	0.01504	280.6
3321	S	11–13			A5III-IV	53	R		H	0.02777	0.00213	223.7
3401	S	230–254			A2Vn	110	R			0.01488	0.00712	156.7
3649	S	21–29			A9IVDel Del	51	R			0.03393	0.01188	67.2
3761	S	249			A3Vn	68	R			0.05223	0.01440	331.3
4263	S				A0pSiCr	152	R			0.1431	0.02499	3577.0
4502	S	0–19			A0V	64	R			0.09110	0.02831	270.8
4554	S	163–178			A0VSB	26	R	P		0.04295	0.00349	28.0
4680	S	135–180			A9.5III	55		P		0.01051	0.00094	23.1
4886	S	215–233			A7V	112		P		0.01200	0.0	107.6
4889	S				A7III	48	R	P		0.01368	0.0	22.7
4893	B		22		A1IIIshe.+HR4892	93	R		H	0.00499	0.00176	101.9
4971	S				A9III-IV	62	R			0.02244	0.00843	61
5040	S	18–26			A2m	64	R			0.1240	0.02372	398.1
5062	S	210–248			A5V	25	R	P		0.04679	0.0	18.8
5069	S				Ap SrEuCr	88	R			0.03570	0.01525	137.2
5107	S	178–222			A3V	22	R			0.02536	0.01250	10.7
5216	S	70–81			A3V	83	R			0.07485	0.01343	444.9
5343	S	96			A8III	49		P		0.00597	0.00092	10.3
5357	S	230			A2Vn	68	R			0.05173	0.01835	305.7
5406	S	90–102			A2IV	72	R			0.07643	0.02048	387.0
5468	S	85–96			A1V	60	R			0.3418	0.03006	1341.9
5491	S				Am	64	R			0.04996	0.01835	148.7
5511	S	265–334			A0V	39	R			0.04499	0.01307	55.9
5729	S				A2V	67	R			0.2684	0.03963	1077.2
5759	S	55–65			A3m	92	R			0.00757	0.00353	45.8
5845	S	68–78			A2m	53	R	P		0.1003	0.00477	181.0
5870	S	120–133			A3V	77	R			0.03756	0.01185	247.8
6081	S				A4II/III	361		P		0.00849	0.00187	790.8
6153	S				A7pSrEuCr	54		P		0.05472	0.00462	113.4
6332	S	21–29			A3IV	90	R			0.00731	0.00380	86.4
6386	S	15–23			A0V	114	R			0.03536	0.01261	740.6
6537	S				A0V	118	R			0.04082	0.0189	461.9
6539	S				A0V	104	R	P		0.07882	0.0	915.0
6681	B		20.8/33.7	2.2/6.5	A0V+G0-2V	76	R		H	0.01784	0.00258	950.9
6782	B		14.2		A3V	51	R		H	0.4866	0.0	81
7012	S				A5IV-V	29	R			0.09705	0.03182	70.8
7018	S	30			A0V	131	R			0.01584	0.00307	303.6
7085	S	90–102			A1V	176		P		0.00967	0.00291	216.6
7250	S	35–44			A4III	102	R			0.01807	0.00725	134.8
7312	S	55–64			A9V	27	R			0.1271	0.00981	86.9
7384	S	170–186			A0V	123	R			0.07768	0.01714	1210.4
7416	S				A0p(CrEuSr)	134	R			0.03580	0.01333	532.1
7423	S	165–180			A3V	95	R			0.01309	0.00464	189.8
7498	S				A4III	42	R			0.08967	0.03027	111
7634	S	175			A4Vn	86	R			0.01048	0.00380	70.1
7702	S	190–207			A3V	200	R			0.01118	0.00461	607.6
7730	S		337		A5IIIn	220	R			0.02710	0.00671	939.9
7734	S	220–238			A0V	310		P		0.00248	0.00068	170.7
7826	S				A3V	83	R			0.02057	0.00765	56.9
8463	B		23.2/	5/	A5V	55	R		H	0.02248	0.00192	219.6
8578	S	45–81			A2m	63	R			0.02248	0.00584	81.1
8675	S				A3V	40		P		0.01243	0.00206	13.4
9060	S				A1IV	63	R			0.07669	0.01949	314.3

C. Schröder and J. H. M. M. Schmitt: X-ray emission from A-type stars, *Online Material p 3*

Table 2. continued.

HR	binary	$v \sin(i)$	sep.	δ mag	Components	Distance	Catalog	CR	±CR	L_{X27}
9062	S	187–191			A1V	49	R	0.05986	0.01889	102.2

C. Schröder and J. H. M. M. Schmitt: X-ray emission from A-type stars, *Online Material p 4*

Table 3. List of X-ray associated A-type stars in binary or multiple systems or with hints of hidden companions.

HR	Binary	$v \sin(i)$	Sep.	δ Mag	Components	Distance	Catalog			CR	±CR	L_{x27}
104	SB				A3m+F0V	81	R			0.03230	0.01111	281.7
127	B			1.2	A2V+F0-1V	53		P		0.02874	0.0	229.5
196	B		2	10	A2Vs+M2-5V	108	R			0.02738	0.00988	303.1
273	SB				A+A	115	R			0.03753	0.01084	1404.7
325	S	70–100			A3III	72	R			0.03847	0.01332	147.2
328	PB	135–149			A3V	49	R			0.06896	0.01929	143.9
361	B		20/1	1/6	A7IV+F0-1+	45	R			0.09316	0.01655	158.2
428	S	75–86			A2Vs	87	R			0.02676	0.00829	157.4
499	B		1+13	1.4+0.3	A3V+F0-5	79	R			0.2440	0.03439	1685.7
526	B		2	0.6	A3V+A2-5V+.	102	R			0.03084	0.01243	275.9
575	SB			2.1	A3IV+?	36	R		H	0.08562	0.00733	451.1
579	B		5	3	A5III+ F	111	R			0.01921	0.00677	684.1
707	SB		0.5/1.9		A5pSr	43	R		H	0.04733	0.00328	372.1
803	B		3+50	4+5.5	A3V+G5-8V	108	R			0.02129	0.00961	262.5
804	B		2.7	3.8	A3V+G5-8V	25	R			0.3764	0.04390	219.9
815	B				A3V+K0IV	63	R	P	H	1.211	0.02160	2771.5
820	B		1.5+30	2+7	A9V+G2-5V	47	R			0.03485	0.00914	74.2
853	B		<1	3.8	A0V+G5V	100	R			0.1296	0.01978	1283.4
884	PB				A2.5V	145	R		H	0.05928	0.00468	3472
971	S	15–23			A1Vs	133	R			0.03695	0.01026	954.9
976	SB		30.8	5.7	A1m	67	R			0.05050	0.01219	215.8
1019	B		4.4	3.8	A0V	162	R			0.02790	0.00945	811.7
1042	PB	136			A1IV	100	R			0.1748	0.03913	2452.1
1189	B		7	0.6	A1V+G2-5V	49	R	P	H	0.02961	0.00328	134.7
1211	SB		7/165	1.4/7	A2V	106	R		H	0.1305	0.00553	2448.8
1324	B				A2V	98	R			0.4692	0.03117	4978.2
1330	PB	138–152			A7V	79	R			0.3023	0.02542	1872.0
1341	PB	35–44			A0pSi	97	R			0.1606	0.02224	1288.9
1342	S	130–145			A3V	95	R			0.02325	0.00856	322.7
1368	SB				A3m	46	R	P		0.02448	0.0	32.6
1376	SB				A1m	47	R			0.02222	0.00919	38.6
1380	SB				A7V	45	R			0.03143	0.00932	101.1
1389	B		1.3/63	3.3/4.5	A2IV	45	R		H	0.01973	0.00188	51.7
1412	SB				A7III	46		P		0.02410	0.0	361.1
1438	B		30	3	A2V	123	R			0.05492	0.02248	532.2
1458	SB				A5m	46	R		H	0.05959	0.00385	632.5
1466	B		0.3/0.8	0.8/1.6	A8V	85	R		H	0.01630	0.00179	524.6
1473	SB				A6V	46	R			0.02527	0.01011	46.0
1490	B		43	5	A2V	103	R			0.09877	0.01624	975.0
1501	PB	73–85			A8V	72	R			0.02963	0.00966	144.8
1511	B		<1	4	A3m	50	R			0.02433	0.00904	40.6
1522	PB	120–132			A2V	85		P		0.00677	0.0	35.1
1530	PB				A8/A9III/IV	68		P		0.0	0.0	[1]
1568	SB		<1	3.4	A1V	115	R			0.1428	0.02016	2088.7
1592	B		4.5	3	A1V+G0-2V	49	R		H	0.1872	0.01070	1656.2
1639	B		0.3	2.9	A5V+G2-5V	82	R			0.02810	0.00931	170.2
1664	B		0.7	0.8	Am+A5-F0V	59	R			0.03835	0.01250	73.5
1666	B	177–200			A3III	27	R			0.1763	0.02362	—
1670	B	30–87	11.8	2.7	A5m+M2V	55	R			0.03316	0.00977	109.8
1734	B	111–124	4.1	6	A7V+K5-M0V	72	R	P		0.02300	0.00181	109.8
1857	B		1.5	3.5	A0V+G0V	114	R			0.04920	0.01299	667.1
1872	PB	140–154			A2V	106	R			0.03153	0.00994	364.1
1971	PB	21–29			A2VpCr	148		P		0.0	0.0	[2]
2015	S	172–225			A7V	44		P	H	0.00609	0.00139	3.6
2020	S	104–130			A5V	19			H	0.00131	0.00031	1.4
2088	B	32–41	12.6	12.2	A2IV	25			H	0.01018	0.00186	18.5
2095	B		2.2/	4.5/	A0pSi+F2-5V	53	R			0.1186	0.01951	94.9
2124	SB				A2V	47	R	P	H	0.1245	0.00359	180.3
2181	B	248	0.1	0.1	A0V+A	80	R			0.02450	0.00744	184.3
2238	PB	35–47			A2Vs	46	R			0.01886	0.00877	35.1
2253	B		2.3/25.4	5.3/7	A3V+G2-5V	195	R			0.02084	0.00915	1292.0
2280	B		0.4	0.5	A4.5V	102	R			0.03662	0.01048	411.2
2298	SB		14/93.6	2.3/8.3	A5IV	39	R		H	0.01297	0.00426	85.7
2320	PB				Am	50	R			0.01822	0.00451	42.9
2328	B	220–238	21.1	2.4	A0Vn	125	R			0.1372	0.01845	2640.5
2421	SB				A0IV	32	R		H	0.06328	0.00555	220.5
2424	B		1.5/21.5	0.8/5.5	A0V+A0V	178	R		H	0.02561	0.00201	2209.4
2466	PB	90–102	0.0055	2.4	A2V	43	R			0.09255	0.01812	125.0
2482	B		8	1.5	A3V	91	R			0.04727	0.01076	259.1
2491	SB				A1V	3	R		H	2.584	0.02469	66.7
2550	PB	206			A7IV	30	R	P		0.08366	0.00296	65.2
2626	SB				A0V	130	R			0.01559	0.00698	191.3
2890	SB				A2Vm	16	R		H	0.3086	0.00202	830.4
2891	SB				A1V	16	R		H	0.3086	0.00202	226.8
2950	B		0.9		A0III	—		P		0.00514	0.00164	—
3173	B		45.6/7.3	8/0.5	A2V+M0V	67	R			0.02640	0.01003	104.6
3221	B		2.8/48.6/+	3.2/...	A7Vm	153	R			0.01983	0.00991	340.9

[1] Simon et al. (1995) calculate an L_x of 33×10^{27} erg/s from PSPC pointing observations. The Second ROSAT Source Catalog of Pointed Observation (2001) lists false detections in the field and therefor no count rate for the source.

[2] In The Second ROSAT Source Catalog of Pointed Observation (2001) this source is flagged as suspect in lightcurve, variability and spectrum. No count rate for the source is listed.

C. Schröder and J. H. M. M. Schmitt: X-ray emission from A-type stars, *Online Material p 5*

Table 3. continued.

HR	Binary	$v \sin(i)$	Sep.	δ mag	Components	Distance	Catalog			CR	±CR	L_{x27}
3260	B		3.6	2.6	A2V+F2V	74	R			0.09536	0.01760	535.5
3314	S	115–161			A0V	38			H	0.00639	0.00157	27
3337	SB		0.17		A5m	85	R		H	0.03410	0.00463	1172.2
3352	SB		1.8	3.3	A2m	84	R			0.05309	0.01266	328.3
3410	SB				A1Vnn	55	R			0.1015	0.02102	218.9
3455	B		3.8	2	A3V	70	R			0.5313	0.05003	2994.4
3460	B		21.4	9.8	A0V	73	R			0.03332	0.01167	214.3
3485	B		0.6/2.6	/3	A1V	24	R		H	0.1047	0.00888	134.0
3524	B				A8V+A8V	98	R		H	0.01935	0.00161	2985.0
3569	SB		10.7		A7IV	15	R		H	0.04752	0.00520	28.2
3586	B	170–186	0.53	3.2	A9Vn	66		P		0.01903	0.0	587.4
3655	B				A3III+A0V	83	R			0.03523	0.01223	271.2
3685	S	145–167			A2IV	34			H	0.00781	0.00090	26.1
3690	SB				A3V	37	R			0.2099	0.02384	206.2
3699	PB	10			A8Ib	212	R			0.05838	0.01893	464.6
3756	B		0.1	0.1	A5III/IV	115	R			0.06428	0.01169	930.5
4065	B	183	2	0.1	A1V	89	R			0.06759	0.01836	574.6
4096	B		1.7	4	A2V	66	R			0.03358	0.01125	131.3
4203	PB		200		A1Vn	116	R			0.02432	0.01012	278.2
4228	S				A0Ia	—		P		0.03660	0.00399	—
4229	B		1.9	0.6	A2IV	96	R			0.03664	0.01580	300.4
4237	B		27.3	5.8	A3m	112			H	0.00438	0.00072	158.8
4296	B		10.6	7.3	A3III-IV	60		P		0.01840	0.0	46.3
4309	B		8.2	5.6	A3III-IV	81			H	0.00536	0.00059	100
4343	B	40–49			A1V+WD	82	R			0.4689	0.04332	2262.8
4350	S				A3IV-V	50	R			0.07834	0.02435	204.1
4380	SB				A2V+A1V	56	R			0.05317	0.01638	122.8
4385	B		<1	3.4	A8IIIm	65	R			0.02670	0.00774	78.5
4405	B		5.2	3.8	A9V	26	R	P		0.02455	0.0	13.1
4422	SB		5.5		A2V	64	R			0.05441	0.01684	195.6
4454	B		<1	2.8	A2m+F8-G0	114	R			0.05492	0.01434	565.5
4528	B		0.3		A1	59	R			0.01922	0.00858	84.9
4535	SB				A3m	63	R			0.02716	0.01110	119.9
4574	B		7.4	6.1	A9V	47			H	0.00499	0.00234	32.2
4599	SB		4.5	9.5	Am	70	R			0.02888	0.01095	81.4
4646	SB				A5m	34	R			0.2709	0.05984	274.2
4703	B		32	5.7	A5V+G8-K0V	103		P		0.01230	0.00384	93.7
4717	PB				A3V	87		P		0.00576	0.00088	31.7
4791	SB		20.3	1.5	A3III-IV	806			H	0.00078	0.00047	—
4796	B		6.9	7.5	A0V	67	R	P	H	0.1107	0.00457	428.4
4855	S		139	3.2	A3V	75	R	P		0.1126	0.0	281.5
4892	SB		22		A0V+A2V+HR4893	68	R			0.01271	0.00541	42.3
4915	SB		20		A0pSiEuHg	34	R			0.07636	0.01479	62.6
4921	B		0.1/20.9	/4.3	A3V	91		P		0.02245	0.0	133.4
5037	PB	205–222			A2V	65	R	P		0.2937	0.00919	1149.8
5054	SB				A2V	24	R	P		0.02818	0.00269	8.6
5055	SB				A1m	—	R	P		0.02172	0.00259	—
5144	B		4.8	3	A1V	93	R		H	0.03321	0.00324	869.5
5234	B		1.5/27.9	0.8/6.4	A1V	143		P		0.04743	0.00848	1127.4
5269	S				ApSi	169			H	0.00088	0.00045	72
5291	SB				A0III	95	R			0.04237	0.00972	274.4
5350	SB				A9V	30	R			0.05820	0.01190	36.0
5360	S				A2IV	102			H	0.00797	0.00254	236.3
5386	B		6.1/	1.7/0.3	A0V+F0V+F2V	66	R			0.08158	0.01807	273.5
5401	B		26.9	5.7	Am	58	R			0.02251	0.01012	48.8
5413	SB		22	5.5	A1V	68	R		H	0.01965	0.00095	690.3
5433	B		2	9.8	A7Vn	71	R			0.04928	0.01152	245.3
5663	B		13.3	4.4	A3m	52	R			0.01862	0.00857	30.9
5697	B		5.7	2.2	A0pSi+F5-8V	123	R		H	0.03590	0.00405	2409.4
5719	B		1.4	5.5	A0pSi	118	R	P		0.05763	0.0	1601.4
5756	SB		11	2.7	A2V	73	R			0.02947	0.01199	112.7
5765	B		9.2/?	1.2/1.4	A4V	102	R			0.07019	0.01404	1160.5
5793	B				A0V+G5V	23	R	P	H	0.1324	0.00681	51.5
5818	B		?	?	A2V	76	R	P		0.06149	0.00519	443.6
5846	B		3.7	1.8	A0V+B	141	R			0.1035	0.01961	2006.2
5887	SB		1.3	3	A3m	80	R			0.01645	0.00533	78.3
5895	B	185–229	0.1		A3Vn	49	R	P		0.04194	0.0	50.9
5961	B		0.2/10	0.5/2.4	A7IV	43	R		H	0.4617	0.01690	3566.3
5983	SB				A2III+G8	212	R			0.03313	0.01155	1066.8
5999 [3]	SB				A7IVe	208	R	P	H	0.2870	0.01450	20422.5
6000	B		1.3	4.6	A1III	241	R	P	H	0.1892	0.00595	3902.4
6097	B		6.2	0.4	A0V+A0V	117	R			0.07391	0.01681	1009.1
6111	SB				A1III+M	105	R			0.02651	0.01026	473.1
6123	B		0.2		A5V	79	R			0.01403	0.00557	123.1
6129	SB		0.8	3.2	A3m	37	R			0.2882	0.02920	372.0
6162	B		16.3	3.3	A4Vn	69	R			0.04089	0.00916	155.2
6186	B		3.7	1	A1Vnn	122	R			0.07209	0.01542	418.2
6216	B		1.9/24	3.5/7.4	A2V	92	R			0.03966	0.01394	208.8
6218	B		5.4	7.6	A3IV	231	R			0.01908	0.00957	1438.3
6240	SB				A7+F6	74	R	P	H	0.4669	0.00742	1344.3
6254	B		1.8/	5.5/	A2VpSrCrEu	54	R		H	0.01402	0.00263	90.7
6317	SB		0.1		A7V	73	R			0.01663	0.00700	144.2
6377	B		0.08/19.5	0/6	A5m	54	R			0.02051	0.00739	42.9

[3] See Zinnecker & Preibisch (1994) and Hamaguchi et al. (2005).

C. Schröder and J. H. M. M. Schmitt: X-ray emission from A-type stars, *Online Material p 6*

Table 3. continued.

HR	Binary	$v \sin(i)$	Sep.	δ mag	Components	Distance	Catalog			CR	±CR	$L_{\alpha 27}$
6435	B	210–228	1.6/11.5	1/4.9	A0V(nn)	114	R		H	0.04231	0.00238	1390.6
6436	SB		0.9		A2V	55	R	P		0.03320	0.0	92.5
6554	SB		60		A6V	30	R			0.01433	0.00427	9.7
6555	SB				A4m	31	R			0.01433	0.00427	9.9
6556	PB				A5III	14	R			0.1241	0.01652	18.3
6618	PB	130–170			A2V	127	R			0.00979	0.00324	207.7
6641	SB		0.1		A2Vs	132	R			0.08195	0.00874	1661.5
6656	B				A2V	67	R			0.00915	0.00344	65.6
6730	B		6.1	0.2	A5IIIn	144	R			0.1143	0.01617	1680.3
6771	SB		25.3/51.7	10.3/7.3	A4IVs	25	R			0.02134	0.00982	8.6
6781	B		0.1/14.2		A3V	70	R		H	0.09434	0.00861	2239.4
6825	PB	25–33			ApSi	1205	R			0.05331	0.01705	–
6843	B		0.7	3.5	A8V	132	R			0.1390	0.02396	3939.3
6876	SB				A5m	58	R			0.04933	0.01029	145.0
6923	SB				A1V	58	R	P	H	0.06139	0.00518	373.0
6956	B		<0.1		A4-5IV/V	74	R			0.04510	0.01560	248.8
7001	B		43/46	9.5/11	A0Va	8			H	0.1125	0.00514	19.4
7051	B		3.4	0.9	A4V	50	R	P	H	0.07280	0.00424	189.1
7056	SB				A4m	47	R			0.2511	0.02232	571.6
7077	B		0.2		A1m	128	R			0.02421	0.01161	649.4
7124	SB				A1Vn	93	R			0.02501	0.00495	203.5
7160	S				A8V	88	R	P	H	0.04693	0.00536	243.4
7214	PB				A4V	55	R			0.07833	0.01560	255.2
7215	B		41.9	5.6	A7V	39	R			0.07750	0.01322	105.3
7235	SB				A0Vn	26	R		H	0.05526	0.00451	84.9
7313	PB	195–212			A1Vn	84	R			0.04254	0.01231	255.3
7392	SB				Am	57	R			0.03887	0.01431	122.3
7431	SB				A1mA2-F0	89	R		H	0.01046	0.00326	134.9
7557	S				A7V	5	R	P		0.1785	0.00357	6.4
7562	B		0.4	3.3	A1m	117	R	P		0.0264	0.0	370.2
7571	B		0.15		A1V+F8IV	117	R			0.3836	0.04335	6865.9
7610	SB				A1IV	63	R	P		0.03413	0.0	122.1
7695	B		4.9/150	3–4/5	A2II-III+	78	R			0.02284	0.00550	101
7755	B		0.2		A2Vn	109	R			0.00606	0.00297	52.6
7775	SB				B9.5III/IV	96	R			0.02685	0.01216	177.6
7781	SB		3		A2Vs	89	R			0.03763	0.00656	291.8
7917	SB		1.2	3	A2V	82	R			0.01681	0.00727	128.0
8021	SB				A7III+G2III	45	R			1.024	0.07911	1802
8028	B		0.2		A1Vne	109	R			0.04808	0.01015	788.3
8060	B		0.3	1.3	A5V	48	R			0.04937	0.01884	188.4
8101	B		17.9	1	A1V	621	R			0.06809	0.01332	—
8140	B		3	2.5	A5V+G0V	30	R		H	0.1034	0.00936	341.3
8151	B		0.15	2.5	A2pCrEuSr+	57	R			0.1062	0.01907	411.2
8162	B		209.2	8	A7IV	15	R	P		0.02026	0.00278	7.1
8210	SB				A8Vm+WD	46	R			1.052	0.06780	3631.1
8263	B		31.3	3.3	A2V	122	R			0.02600	0.01072	322.3
8266	PB	185–201			A5V	63	R			0.01405	0.00626	36.6
8307	B		1.4/	5.4/	A0V	84		P		0.05806	0.00468	4326.6
8322	B				Am	12	R			1.655	0.12550	187.5
8396	SB				A2V+K0III	145	R		H	0.03348	0.00316	505.2
8417	SB				A3m	31	R		H	0.05639	0.00470	169.7
8431	PB				A2V	40	R			0.03442	0.01345	89.6
8518	SB				A0V	48	R			0.05508	0.01707	92.9
8533	B		0.5/	0.2/	A0V	130	R	P		0.01041	0.0	448.2
8576	B		30.3	2	A0V	45	R			0.06447	0.01814	88.5
8598	B		9.5/	3/	A0V	123	R			0.01753	0.00758	104.9
8600	PB				A3Vn	69	R			0.03796	0.01648	169.9
8662	SB				A9IIIm	74	R		H	0.00376	0.00108	14.8
8724	B		3.9	2.9	A3Vs	82	R			0.04692	0.01266	337.9
8738	S				A1V	96		P		0.01433	0.00	90.2
8799	S				A5V	40	R			0.02123	0.00783	14.7
8865	B		1.2	4	A0V	76	R		H	0.07713	0.00658	834.0
8884	B		13.2	3.5	A5Vn	80	R			0.01986	0.00827	121.2
8963	B		27.7	6.2	A1Vn	73			H	0.00203	0.00086	31.3
9016	B		3.3/	7/	A0V	44	R	P	H	0.1724	0.00813	379.4
9039	PB	156–180			A4Vn	58	R			0.03021	0.01058	99.6

Chapter 3

Magnetic fields in A-type stars associated with X-ray emission

C. Schröder, S. Hubrig and J. H. H. M. Schmitt
Astronomy & Astrophysics, 484, 479 (2008)

Astronomy & Astrophysics manuscript no. 8963
May 22, 2008

Magnetic fields in A-type stars associated with X-ray emission

Christian Schröder[1], Swetlana Hubrig[2], and Jürgen H. M. M. Schmitt[1]

[1] Hamburger Sternwarte, Gojenbergsweg 112, 21029 Hamburg, Germany
[2] European Southern Observatory, Casilla 19001, Santiago 19, Chile

Received 30 October 2007 / Accepted 25 Februar 2008

ABSTRACT

A common explanation for the observed X-ray emission of A-type stars is the presence of a hidden late-type companion. While this assumption can be shown to be correct in some cases, a number of lines of evidence suggests that low-mass companions cannot be the correct cause for the observed activity in all cases. A model explains the X-ray emission for magnetic Ap/Bp stars, focusing on the A0p star IQ Aur. In this paper we test whether this theoretical model is able to explain the observed X-ray emission. We present the observations of 13 A-type stars that have been associated with X-ray emission detected by ROSAT. To determine the mean longitudinal magnetic field strength we measured the circular polarization in the wings of the Balmer lines using FORS1. Although the emission of those objects that possess magnetic fields fits the prediction of the Babel and Montmerle model, not all X-ray detections are connected to the presence of a magnetic field. Additionally, the measured magnetic fields do not correlate with the X-ray luminosity. Accordingly, the magnetically confined wind shock model cannot explain the X-ray emission from all the presented stars.

Key words. stars: magnetic fields – stars: activity – X-rays: stars

1. Introduction

One of the outstanding discoveries of X-ray astronomy is the detection of X-ray emission from essentially all late-type main sequence stars (cf. see the compilation by Schmitt & Liefke (2004) and references therein). For hot stars X-ray luminosity scales with the stars' bolometric luminosity, while for late-type stars X-ray emission is intimately linked to stellar rotation and convection. The role of magnetic fields – if any – in the X-ray emission of early-type stars is unclear. Almost immediately after the detection of X-ray emission from early-type stars (Seward et al. 1979; Harnden et al. 1979), Lucy & White (1980) and Lucy (1982) proposed a phenomenological model, in which the X-ray emission is generated from instabilities in these stars' radiatively driven winds (Feldmeier et al. 1997; Owocki & Cohen 1999); an example of this kind of X-ray producing mechanism is the prototypical O-type star ζ Pup (Kramer et al. 2003). An alternative wind shock model was introduced by Babel & Montmerle (1997), who assume large scale magnetic structures confining the (still radiatively driven) wind; the wind shock model can be brought into very good agreement with the observations (Gagné et al. 2005) for the magnetic O-type star Θ^1 Ori C. On the other hand, the X-ray emission from late-type stars is usually interpreted as a scaled-up version of solar X-ray emission, where the emitting hot plasma is believed to be confined by coronal magnetic fields. Indeed, convection and rotation have been shown to be the central ingredients of the magnetic dynamos thought to be ultimately responsible for the observed activity phenomena in the Sun and other late-type stars (see Schmitt et al. (1995) and references therein).

In this scenario, A-type stars ought to be devoid of any X-ray emission. The winds of such stars should be either absent or be weak at best. However, contrary to expectations some A-type stars do in fact show X-ray emission. About 15% of all bright A-type stars can be identified with X-ray sources found in the ROSAT All Sky Survey or ROSAT pointed observations (Schröder & Schmitt 2007). Specifically, out of 1966 bright A-type stars ($m_v < 6.5$), 312 were detected as X-ray sources, with 194 of these detections occurring in known binary systems. Subdivisions of these stars into Ap, Am and giant A-type stars gives detection rates similar to the overall sample. The usual explanation of these 194 "unexpected" X-ray detections is to attribute their X-ray emission to the presence of low mass companions, and in the 118 A-type stars without known companions such companions are postulated to exist. It is of course relatively easy to "hide" a low mass companion of, say, spectral type M in the vicinity of a bright A-type star. Further, A-type stars are by comparison young and thus an hypothetical late-type companion should be quite X-ray luminous, so that the observed X-ray luminosities of such A-type stars are consistent with X-ray luminosities observed for young M stars and even T-Tauri stars. In some specific cases, the correctness of the above described low-mass companion scenario can be explicitly shown. For example, in the case of the totally eclipsing binary α CrB, a total X-ray eclipse is found at the time of optical secondary minimum, when the A-type star in the system is located in the front of the X-ray emitting G-type star (Schmitt & Kürster 1993), thus proving that indeed essentially all the X-ray flux from this system does come from the G-type star.

Assuming this "companion hypothesis" to be correct, a few strange findings, which have been accumulated over the years, remain to be explained (summarized by Schmitt et al. (2005)). First, in quite a few cases (Berghöfer & Schmitt 1994; Hubrig et al. 2001; Stelzer et al. 2006a) high angular resolution data of (visual) binary systems show X-ray emission from both system components, implying that further components need to be introduced to explain the observed A-type star X-ray emission. Next, the star with the largest measured magnetic field of 35000 G is Babcock's star HD 215441 and its spectral type A0Vp suggests neither the presence of convection nor of a strong wind. Yet Babcock's star is an X-ray source (Czesla & Schmitt 2007). X-ray emission and in particular X-ray flaring has been observed

from the (extremely) peculiar B-type star σ Ori E with a surface magnetic field of 10 kG (Groote & Schmitt 2004), yet no companion is known. Two dimensional MHD simulations from ud-Doula et al. (2006) suggest that these flares are caused by centrifugal breakout of the magnetically confined line-driven wind. Further, X-ray emission has been observed not only from Babcock's star, but also stars with the highest measured magnetic fields as listed in the compilation by Bychkov et al. (2003). An orbital modulation of the X-ray emission has been observed for the magnetic stars Θ Ori C (Gagne et al. 1997) as well as HD 133880 (Czesla & Schmitt, in preparation). Finally, a survey for X-ray emission for the magnetic stars listed in the catalog by Bychkov et al. (2003) showed a total of 23 stars detected as X-ray sources identifiable with A-type stars with large magnetic fields (Schmitt et al. 2005). It appears to be extremely contrived to attribute the observed X-ray emission in all these cases to hitherto unseen late-type companions. Rather the existence of a large scale magnetic field seems to be necessary for the production of these "unexpected" X-ray emissions. With the so-called magnetically confined wind-shock model by Babel & Montmerle (1997) a theoretical framework has been constructed to explain the observed high energy emissions. In the last decade, significant progress has been made, for example by Donati et al. (2002), ud-Doula & Owocki (2002), Gagné et al. (2005) and Townsend et al. (2007), to describe and simulate the interactions between the line-driven winds and the magnetosphere of hot stars like σ Ori E and Θ Ori C. The predictions of the dynamical models used by these authors are in good agreement with the observations, and therefore motivated us to search for possible evidence for magnetically confined wind shocks in X-ray emitting A-type stars. Specifically, in this paper we try to test whether the detection of X-ray emission is directly related to the presence of a large scale magnetic field, as suggested by the wind-shock model. Additionally, we check if the measured magnetic field strengths are correlated to the X-ray luminosity of the star.

We present the observations and the data reduction technique in section 2. Section 3 is divided into the calculations of the magnetic fields, a verification of the magnetically confined wind-shock model for those stars that have been detected at a 3σ level and some comments on those stars. We summarize and discuss our data in section 4.

2. Observations and data reduction

The observations reported in this paper were carried out on August 28th 2006 with FORS1 at the VLT Kueyen. This multimode instrument is equipped with polarization analyzing optics comprising super-achromatic half-wave and quarter-wave phase retarder plates, and a Wollaston prism with a beam divergence of 22" in standard resolution mode.Two different grisms were used, the GRISM 600B and the GRISM 1200B, which cover all Balmer lines from H_β to the Balmer jump. 12 stars have were observed with the GRISM 600B and the corresponding spectral resolution of 2000, and three stars with the GRISM 1200B at a resolving power of R ~ 4000. GRISM 1200B does not include all hydrogen lines down to the Balmer jump (~3650 Å). The blue limit of the spectra is 3885 Å. Since we had only one observing night, we decided to observe only the two most promising targets with GRISM 1200B.

During the calibration runs in daytime two retarder waveplate setups with angles of +45° and -45° were used. The calibration itself was achieved by combining the science spectra with the corresponding calibration spectra of the same retarder waveplate angle. Ordinary and extraordinary beams were independently calibrated with the corresponding beams of the reference spectrum. By examining the differences between the circular polarizations observed in the red and blue wings of the hydrogen line profiles it is possible to measure the mean longitudinal field $< B_z >$ (Landstreet 1982) by using the formula

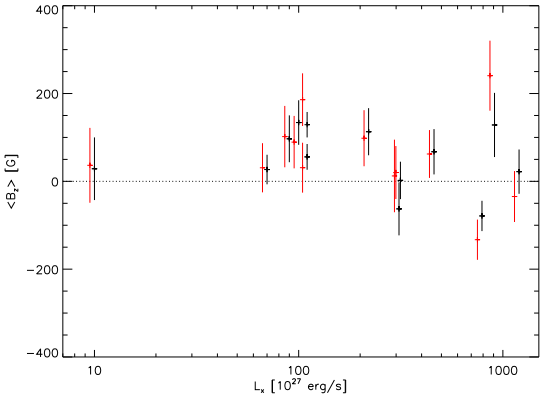

Fig. 1. Mean longitudinal magnetic field measurements plotted over L_x of the associated X-Ray source. Black symbols show the data measured by all lines, red data the values extracted from the hydrogen lines. For purposes of clarity, the red data points are shifted to the left by a few percent.

$$\frac{V}{I} = -\frac{g_{\rm eff} e \lambda^2}{4\pi m_{\rm e} c^2} \frac{1}{I} \frac{dI}{d\lambda} \langle B_z \rangle. \quad (1)$$

In (1) V denotes the Stokes parameter measuring the the circular polarization, I denotes the intensity in the unpolarized spectrum, $g_{\rm eff}$ is the effective Landé factor, e denotes the electron charge, λ the wavelength, $m_{\rm e}$ the electron mass, c the speed of light, $dI/d\lambda$ is the derivative of Stokes I, and $\langle B_z \rangle$ is the mean longitudinal field. The V/I values were calculated according to:

$$\frac{V}{I} = \frac{1}{2} \left\{ \left(\frac{f^o - f^e}{f^o + f^e} \right)_{\alpha=-45} - \left(\frac{f^o - f^e}{f^o + f^e} \right)_{\alpha=+45} \right\} \quad (2)$$

where α is the position angle of the retarder waveplate, which was rotated by 90° (+45°,-45°,-45°,+45° etc.) for the different exposures to reduce any cross-talk effect. f^o and f^e denote the ordinary and the extraordinary beams, which have been summed to obtain the Stokes I values. For each star we took three to four pairs of exposures with two orientations of the retarder waveplate, resulting in six to eight exposures for each object. A more detailed description of this method has been given by Bagnulo et al. (2002) and Hubrig et al. (2003, 2004a).

3. Results

3.1. Stellar sample and magnetic field detections

The stars in our sample were selected from a list of bright A-type stars, which can be associated with a X-ray source compiled by Schröder & Schmitt (2007). Out of 84 stars known as single or resolved binary stars a subsample of 13 stars (excluding the standard star HD 201601) was selected taking into account observational boundary conditions. In Table 1 we provide the basic data

Table 1. Basic data and measured magnetic fields for the stars from the GRISM 600 in the upper part of the table and the GRISM 1200 in the lower part. Stars with a longitudinal magnetic field at a $3\,\sigma$ level are indicated in bold face.

HD	Other id.	V	Sp. type	dist	log L_x	log L_x/L_{bol}	v sin(i)	$\langle B_z \rangle$ all	$\langle B_z \rangle$ hydr.	$\langle B_e \rangle$ lit. [1]	Rem.
GRISM 600				[pc]	[erg/s]		[km/s]	[G]	[G]	[G]	
147084	*o* Sco	4.6	A4II/III	361 ± 99	29.89	-0.91	23	-79 ± 35	-133 ± 46	170 ± 98	
159217	σ Ara	4.6	A0V	118 ± 10	29.66	-2.30	-	67 ± 52	62 ± 54		
159312	HR 6539	6.5	A0V	104 ± 10	29.96	-2.94	-	128 ± 73	241 ± 80		
163336	HR 6681	5.9	A0V	76 ± 6	29.49	-3.63	60	2 ± 43	20 ± 60		
172555	HR 7012	4.8	A5IV-V	29 ± 1	28.85	-4.89	-	27 ± 34	31 ± 56		disk
174240	HR 7085	6.2	A1V	176 ± 25	29.30	-3.23	102	113 ± 54	98 ± 64		
182761	HR 7384	6.3	A0V	123 ± 11	30.08	-2.69	186	22 ± 50	-35 ± 58		
186219	HR 7498	5.4	A4III	42 ± 1	29.34	-4.42	-	56 ± 29	58 ± 62		
201601	γ Equ	4.7	A9p	35 ± 1	< 28.47	-	10	-1121 ± 34	-1085 ± 42	(sect. 3.3)	std
215789	ϵ Gru	3.5	A3V	40 ± 1	28.00	-4.75	-	29 ± 71	37 ± 85		disk
217186	HR 8738	6.3	A1V	96 ± 8	28.95	-4.04	60	97 ± 53	93 ± 66		
224361	HR 9060	6.0	A1IV	63 ± 2	29.49	-3.89	-	-63 ± 60	12 ± 83		
224392	η Tuc	5.0	A1V	49 ± 1	29.00	-4.17	187	134 ± 51	89 ± 60		disk
GRISM 1200B											
147084	*o* Sco	4.6	A4II/III	361 ± 99	29.89	-0.91	23	-48 ± 15	-87 ± 36	170 ± 98	
148898	ω Oph	4.4	A7p	54 ± 2	29.34	-3.76	60	122 ± 29	186 ± 60	249 ± 169	
201601	γ Equ	4.7	A9p	35 ± 1	< 28.47	-	10	-1200 ± 12	-1136 ± 27	(sect. 3.3)	std

of the observed stars as well as the results of our magnetic field measurements. The columns in Table 1 give the HD number, the HR number, the visual magnitude, the spectral type, the X-Ray luminosity, the mean longitudinal magnetic field determined by all spectral lines, the mean longitudinal magnetic field extracted from the hydrogen lines given in Table 1, the averaged quadratic magnetic field whenever available as listed in the Bychkov catalog of stellar effective magnetic fields and in the last column remarks about the individual stars. The values of the averaged quadratic magnetic field given in column 11 are calculated by

$$\langle B_e \rangle = \left(\frac{1}{n} \sum_{i=1}^{n} B_{ei}^2 \right)^{\frac{1}{2}}, \qquad (3)$$

where B_{ei} is the i^{th} measurement of the effective magnetic field, and n is the total number of observations for a given star. The averaged quadratic errors are calculated accordingly.

The low-resolution FORS1 spectropolarimeter is usually used to measure circular polarization in the wings of strong and broad spectral lines like Balmer lines or strong He or Ca lines. One of the reasons for this is that weaker and narrower metal lines appear unresolved at the low spectral resolution achievable with FORS1 ($R \sim 2000 - 4000$) and the magnetic fields determined from all metal lines frequently appear to have lower strengths when compared to the fields measured using intrinsically broad hydrogen lines. The accuracy of the magnetic field measurements depends on the spectral type and the complexity of the spectra of the studied targets, on their rotational velocity, but of course also on the strength of the measured magnetic field. Our experience from a study of a large sample of magnetic and non- magnetic Ap and Bp stars and Herbig Ae stars (Hubrig et al. 2004b, 2006) shows that magnetic fields measured from Balmer lines only or using also all metal lines are in good agreement with each other for weak magnetic fields of the order of 300–400 G and less. For stronger fields the difference between both field measurements becomes larger than the measurement uncertainties with a tendency for magnetic fields to be larger when measured from hydrogen lines. The probable explanation for such a behavior is that Eq. (1) applied to metal lines is only valid in the weak field regime. Since the measured magnetic fields in this study are very weak, we present in Table 2 both measurements, using hydrogen lines and all metal lines.

Out of the 13 stars studied (excluding the standard star HD 201601), 8 show signatures of magnetic fields. The three stars HD 147084, HD 148898 and HD 159312 have field measurements above the 3σ level in all or the hydrogen lines, while previous measurements of B-fields were below the 2 σ level for HD 147084 and HD 148898 and the field measurement for HD 159312 is entirely new. The stars with a longitudinal magnetic field at at least a $3\,\sigma$ level are indicated in bold face in Table 1. The stars HD 174240 and HD 224392 are detected above the $B_z > 2\sigma$ level in all lines, the stars HD 186219 and HD 217186 just below the $B_z > 2\sigma$, while the Balmer line only detections have less significance, therefore follow-up measurements for these objects are highly desirable before any definite conclusions with respect to the presence of larger magnetic fields can be drawn. For the rest of our sample stars, i.e. HD 159217, HD 163336, HD 172555, HD 182761, HD 215789 and HD 224361, we do not claim any magnetic field detections. Thus in summary, out of 13 observed stars, we have 3 detections, 4 candidates for magnetic field detections and 6 non-detections.

Fig. 1 shows the magnetic field measurements, including the 1σ error bars, plotted over the X-ray luminosity of the associated X-ray source. The black symbols represent the values extracted from all available spectral lines, while the red data points show the magnetic field calculated from the hydrogen lines. In order to increase the clarity of the plot, we shifted the hydrogen lines measurements by a few percent. As the plot shows, no sign of a correlation between the X-ray luminosity and the magnetic field strength has been found. We note that because of the strong dependence of the longitudinal field on the rotational aspect, its usefulness to characterize actual field strength distributions is rather limited (Hubrig et al. 2007a). If the magnetic axis is tilted to the rotation axis, as is often the case, the component of the magnetic field parallel to the line of sight changes with the rotation phase. This can be overcome, at least in part, by additional observations to sample various rotation phases, hence various aspects of the field.

The mean longitudinal magnetic field is the average over the stellar hemisphere visible at the time of observation of the

[1] Catalogue of stellar effective magnetic fields (Bychkov et al. 2003)

component of the magnetic field parallel to the line of sight, weighted by the local emergent spectral line intensity. It is diagnosed from the slope of a linear regression of V/I versus the quantity $-g_{\rm eff}\Delta\lambda_z\lambda 2\frac{1}{I}\frac{{\rm d}I}{{\rm d}\lambda}\langle B_z\rangle+V_0/I_0$. This procedure is described in detail by Bagnulo et al. (2002) and Hubrig et al. (Hubrig et al. (2004a)). Our experience with a study of a large sample of magnetic and non-magnetic Ap and Bp stars revealed that this regression technique is very robust and that detections with $B_z > 3\,\sigma_z$ result only for stars possessing magnetic fields (Hubrig et al. 2006).

3.2. Disk contamination in H_α, H_β and Ca II H and K

In a few cases, namely HD 172555, HD 215789 and HD 224392, the presence of a circumstellar disk might contaminate the H_α, H_β and CaII H and K lines. The contamination also could affect H_γ, H_δ and the higher Balmer lines, but it is weaker than in H $_\alpha$ and H_β. To test the influence of this line contamination on the magnetic field measurements we calculated the magnetic fields in two ways: one calculation was done using all available spectral lines in the given spectral area, the other method was using just the hydrogen lines (see Table 1). Comparing the results for the two different line sets, there is no influence on the magnetic field measurements. Two disk stars, HD172555 and HD 215789, have no magnetic field. HD 224392 shows signs of magnetic fields at the 2σ level. In all these measurements the error bars are smaller in the calculations using all available spectral lines. This is no surprise, since the larger number of data points for the calculation of the magnetic field due to the larger number of measured spectral lines results in a lower error value. A systematic difference between the two line sets in respect of the presence of a disk has not been found.

3.3. Notes on individual stars

– **HD 147084** is an A4 giant star associated with an X-ray source at a distance of 5 arcsecond from the optical position of the star. Observations of this object have been performed in the PSPC pointing mode, resulting in an X-ray luminosity of 7.9 $\times 10^{29}$ erg/s. The nature of this object is unclear. If it is a member of Sco OB2, which has an age of around 30 MYrs and includes some pre-main sequence objects (Eggen 1998), it might be a laggard Herbig Ae star. However, Whittet (1988) argues against the presence of an infra-red excess, which would be expected for a Herbig Ae star. The Hipparcos and Tycho Catalogues list two entries with distances of 360±100 pc and 200±90 pc for HD 147084. The first measurement would question the association of this object with Sco OB2, which lies at a distance of roughly 150 pc; the second value would support membership. Admittedly, at such distances, the Hipparcos data have substantial errors. Another possibility would be that o Sco is a Ceph type radial pulsator. If this object is a massive star and member of Sco OB2, it might have left the main sequence after 30 MYrs and became a Cepheid-type variable. The magnetic field measurements revealed a weak field of -79 ± 35 G in all lines and -133 ± 46 G in the hydrogen lines in the GRISM 600B observations and -48 ± 15 G in all lines and -87 ± 36 G in the hydrogen lines in the GRISM 1200B observations. Distinct Zeeman features are visible in the Ca II H and K lines (see Fig. 2). Similar features have been discovered in the spectra of the Herbig Ae star HD 31648 (Hubrig et al. 2007b), which is shown in Fig. 3. In the Catalogue of stellar effective magnetic fields (Bychkov et al. 2003) HD 147084 is recorded with 170 ± 98 G. According to Levato et al. (1987), the radial velocity variations with an amplitude of 50 km/s may be due to intrinsic motions of the atmosphere. We therefore do not necessarily associate this radial velocity variations with the presence of a late-type companion.

– **HD 148898** is a chemical peculiar single star of spectral type A7p. The X-ray source, which is separated from the optical position of the A-type star by 8 arcseconds, possesses an X-ray luminosity of 1.1 $\times 10^{29}$ erg/s. Bychkov et al. (2003) list this star with a magnetic field of 248.6 ±169.4 G based on the measurements of Borra & Landstreet (1980). Our calculations resulted in a magnetic field of 122 ± 29 G for all lines and 186 ± 60 G for the hydrogen lines, therefore exceeding the 3σ level. The Stokes I and V/I spectra are presented in Fig. 4. In May 2003 Hubrig et al. observed this star with the GRISM 600B and found a magnetic field of 221 ± 38 G for all lines and 175 ± 64 G for the hydrogen lines.

– **HD 159217** This A0V star has an associated X-ray source listed in the ROSAT All-Sky Survey catalog. The separation from the optical position of the star is about 8 arcseconds and the X-ray luminosity is 4.6 $\times 10^{29}$ erg/s. No indicator for the presence of a hidden companion has been found. The magnetic field measurements yield no detection. The Stokes I and V/I spectra for this star are presented in Fig. 5.

– **HD 159312** is a single A0V star with a magnetic field of 128 ± 73 G measured with all spectral lines and 241 ± 80 G in the hydrogen lines (see Fig. 5). The longitudinal field is a first detection at a 3 σ level (see 1. This star has been detected in the ROSAT All Sky Survey and in the pointed observations with the PSPC instrument. While the X-ray source listed in the RASS catalog has a separation of 5 arcseconds from the optical position of the star, the PSPC pointings have a larger offset of 20 ” between the X-ray and optical positions. The larger offset in the pointing observation is most likely due to location of the source near the PSPC entrance rib, while the good agreement between RASS and optical position is probably a chance coincidence. No indications for a hidden late type companion have been found.

– **HD 163336** is an A0V star associated with an X-ray source separated by less than 3 arcseconds from the optical position of the star with an X-ray luminosity of 3.1 $\times 10^{29}$ erg/s in the HRI observations. No signs of a hidden companion have been found. Our measurements showed no significant magnetic field, but close inspection shows an increased signal in the Stokes V/I spectrum at the positions of the H_δ and H_ϵ line (see Fig. 6). Hence this star might be a possible candidate for further observations.

– **HD 172555** has a spectral type of A5IV-V and is one of the three stars in our sample with a debris disk. The star is only detected in the ROSAT All-Sky Survey with a separation of 27 arcseconds between the optical position and the X-ray source. With a X-ray luminosity of 7 $\times 10^{28}$ erg/s this object is one of the fainter sources in our sample. A M0 dwarf is positioned at a separation of 71 arcseconds. The X-ray emission from the M-type star and that from the A-type star are elongated in a way that they form an area of X-ray emission covering the positions of the two stars. In a *Chandra* observation from March 2004, the M dwarf was clearly detected but no X-ray source was found at the position of the A star. The upper limit for a thermal spectrum with a temperature of 0.9 keV is 5.7 $\times 10^{26}$ erg/s. The non-detection of HD 172555 suggests that the RASS detection might be an artifact. Radial

velocity measurements revealed no variations. The magnetic field measurement yielded no detection.

– **HD 174240** The associated X-ray source of this A1V star was observed in the PSPC pointing mode. Its luminosity is 2.2×10^{29} erg/s. The absence of radial velocity variations reduces the possibility for a hidden companion. A longitudinal magnetic field was measured at the 2 σ level.
– **HD 182761** This A0V star is associated with an X-ray source listed in the ROSAT All-Sky Survey catalog. The separation from the optical position of the star is about 25 arcseconds and the X-ray luminosity is 1.2×10^{30} erg/s, making this source the X-ray brightest in our sample. No indicator for the presence of a hidden companion has been found. The magnetic field measurement yielded no detection.
– **HD 186219** is listed as an A4III star in the SIMBAD catalog. The X-ray source is separated from the optical position of the star by 12 arcseconds. Its luminosity is 1.1×10^{29} erg/s in the RASS catalog. The radial velocity is constant and no other indicator for a hidden companion has been found. No magnetic field has been detected in our observations.
– **HD 215789** is an A3V star with a debris disk. A faint X-ray source with a luminosity of 1.3×10^{28} erg/s was detected near the optical position of the star in the PSPC pointing observations, separated from the star by 8 arcseconds. Further observations of this object have been carried out with XMM-Newton, showing a moderately active X-ray source with flaring in one of the three observations. With plasma temperatures ranging between 2 and 8 MK in a two temperature model for the less active state and up to 15 million Kelvin in the observation with the flare, this X-ray emission is in good agreement with a moderately active late-type companion. The X-ray luminosity varies between 6×10^{27} and 3×10^{28} erg/s and is therefor consistent with the ROSAT observations. Our own measurements showed no significant magnetic field.
– **HD 217186**: This bona fide single star of spectral type A1V is associated with an X-ray source observed in the PSPC pointing mode. The luminosity of the source is 9×10^{28} erg/s and it is separated from the star by 15 arcseconds. Our magnetic field measurements yielded weak signs of a longitudinal field of 97 ± 53 G in all lines and 102 ± 70 G using just the hydrogen lines, thus slightly below the 2 σ level.
– **HD 224361** is listed in the SIMBAD database as an A1IV star according to Houk & Cowley (1975). Other authors mention this star as spectral type A2p, which could indicate the presence of a magnetic field, but our measurements detected no magnetic field. Close inspection on the other hand shows a clear feature in the H_δ line (see Fig. 7). The associated X-ray source was detected in the RASS and has a luminosity of 3.1×10^{29} erg/s. Its separation from the optical position of the star is 15 arcseconds. No indicator for the presence of a hidden companion has been found.
– **HD 224392**: This A1V star is another IR excess star. The magnetic field measurements revealed a longitudinal field at a significance level of 2.5 σ using all lines. The field strengths in all and just the hydrogen lines are 134 ± 51 G and 89 ± 60 G, respectively.Observations done during the RASS detected an X-ray source with a separation of 16 arcseconds from the optical position of the A-type star and luminosity of 1×10^{29} erg/s.
– **HD 201601**: The strongly magnetic rapidly oscillating A9p star with a rotation period of approximately 77 yr has been selected to check that the instrument and data reduction were functioning properly. The measured values of the magnetic field using hydrogen lines agree well with the observations obtained a few years ago with the same instrument by Hubrig et al. (2004a). The calculated averaged quadratic magnetic field from the 18 measurements presented in that paper is 1085 ± 56 G.

4. Discussion and summary

In this paper we present measurements of the longitudinal magnetic field in A-type stars obtained with the FORS1 instrument at the VLT Kueyen. The 13 observed A-type stars were taken from a list of single or resolved binary stars that are associated with an ROSAT X-ray source (Schröder & Schmitt 2007) in order to test the hypothesis that X-ray emission in A-type stars might be related to the presence of magnetic fields. Two of our targets, HD 147084 and HD 148898, had been previously checked for magnetic fields, but the results of those observations lead to somewhat unsatisfactory significance levels of 1.5 σ. With our measurements we obtained detections above the 3 σ level for HD 147084 and HD 148898, thus confirming previous measurements with low significance, and for HD 159312, which is an entirely new result. Our measurements for four additional stars, HD 174240, HD 186219, HD 217186 and HD 224392, yielded detections at a significance level between 2 and 3 σ; we therefore consider these stars to be possible magnetic field candidates, which ought to be followed up. In the other six stars in our sample magnetic fields were not detected by our methods, although Zeeman features might possibly be present in some of the Balmer lines, warranting more sensitive observations for those stars.

With our observations we tested to what extent the magnetically confined stellar wind model (MCWS) proposed by Babel & Montmerle (1997) can explain the observed X-ray emission of late B- and A-type stars. Using radiatively driven wind models and including the effect of magnetic confinement of the wind, Babel & Montmerle (1997) were able to calculate a physical model explaining X-ray emission of the chemically peculiar A-type star IQ Aur. The basic assumption of the model is that the stellar wind is confined by the magnetic field lines. Due to the dipole structure of the field, the winds originating from the two different polar regions collide in the magnetic equatorial plane and produce shocks. In these shocks the kinetic energy of the wind is dissipated to eventually produce X-ray emission. In their calculations, Babel & Montmerle (1997) find that the X-ray luminosity L_x scales approximatively like the mass loss rate $\dot{M}$, the wind velocity v_∞ and the magnetic field B. The resulting scaling law for the X-ray luminosity is

$$L_x \simeq 2.6 \times 10^{30} \frac{erg}{s} \left(\frac{B_*}{1\ kG} \right)^{0.4} \xi \tag{4}$$

where ξ is described by

$$\xi = \left(\frac{\dot{M}}{10^{-10} M_\odot / yr} \right)^{\delta} \left(\frac{v_\infty}{10^3\ km\ s^{-1}} \right)^{\epsilon}. \tag{5}$$

Based on the calculations, δ and ϵ can be obtained as $\simeq 1$ and 1 - 1.3 respectively. The X-ray observations of IQ Aur can be understood with a wind velocity of IQ Aur of 500 - 900 km/s and mass loss rates of $4.5 \times 10^{-11} M_\odot / yr$. Czesla & Schmitt (2007) studied magnetic late B- and A-type stars that have been observed in X-rays with the *Chandra* telescope and found values ranging from 860 - 940 km/s for v_∞ and 1 - 4 $\times 10^{-11} M_\odot / yr$ for $\dot{M}$ to account for the observed X-ray emission within the framework of the MCWS model. We use these values to estimate the X-ray

emission from those of our stars with magnetic fields measured at a 3σ level, noting, however, that the uncertainties on the wind properties of up to one order of magnitude only allow a rough estimate of the expected X-ray emission.

The magnetically confined wind shock model predicts an X-ray luminosity of 5×10^{29} erg/s with values of 900 km/s for the wind velocity v_∞, $4 \times 10^{-11} M_\odot/yr$ for $\dot{M}$ and 240 G for B in the case of HD 159312 (see Fig. 5). Decreasing the mass loss rate to $1 \times 10^{-11} M_\odot/yr$ lowers the predicted X-ray luminosity to 1.3×10^{29} erg/s. The observed X-ray luminosity for HD 159312 in the PSPC pointing and the ROSAT All-Sky Survey observations is 9.1×10^{29} erg/s, hence of the same order of magnitude as the calculated value.

The magnetic field in HD 148898 is slightly weaker than in the previous object HD 159312, resulting in a lower calculated X-ray luminosity. Assessing the values derived by Czesla & Schmitt (2007) and Babel & Montmerle (1997), the wind shock model predicts an L_x of 1 - 4 $\times 10^{29}$ erg/s for mass loss rates of 2 - 4 $\times 10^{-11} M_\odot/yr$ and wind velocities of 500 - 900 km/s. The observed X-ray luminosity is 1×10^{29} erg/s, therefore in good accordance with the predicted values for low wind velocities and mass loss rates.

In the case of HD 147084, which is listed in the SIMBAD database as a (bright) giant A4 star, the situation is a bit more complicated (see section 3.3). HD 147084 might be a member of the group of Herbig Ae/Be stars (Herbig 1960), whose X-ray emission has been studied by various authors (Hamaguchi et al. 2005; Stelzer et al. 2006b; Zinnecker & Preibisch 1994; Damiani et al. 1994). Another possible explanation for the high luminosity of this star is that it is an evolved massive star in the Cepheid phase, whose radial pulsations might be able to explain the variations in the radial velocity. In both scenarios, the observed X-ray emission is not unexpected.

In our test for a correlation between the X-ray luminosity of the associated X-ray source and the measured magnetic field strength we found no clear dependence between the two values. The X-ray brightest star, HD 182761, has no detectable magnetic field. To reproduce the X-ray luminosity of 1.2×10^{30} with the magnetically confined wind shock model, this star would require an easily detectable magnetic field of 1.5 kG, assuming the wind velocity and mass loss rate given in section 3.2. Therefore, HD 182761 either has unusual values for wind velocity and mass loss rates, or an explanation for its X-ray emission must be sought outside the framework of the MCWS theory.

On the other hand, those stars with a detected magnetic field possess X-ray emission are in agreement with the predicted values from the MCWS model of Babel and Montmerle. In this context however, the question arises of why the standard star HD 201601, a chemically peculiar A9 star with a magnetic field above 1 kG, was not detected in X-rays. A possible explanation might be that the early A-type stars, IQ Aur is an A0p star, still possess a weak wind, which is necessary to produce the X-ray emission, but the later A-type star lack such a wind. In addition, the star HD 201601 is rather old and has already spent more than 60% of its life on the main sequence (Hubrig et al. 2000), which might explain the absence of X-ray activity in this star with a strong magnetic field.

The results in this paper agree with the conclusions Czesla & Schmitt (2007) presented in their analysis of A- and B-type stars with substantial magnetic fields. They too found that the presence of a (strong) magnetic field is not necessarily accompanied by a strong X-ray emission. Other parameters like the mass loss rate and the wind velocity may play an even more important role.

Thus 7 out of 13 studied stars show (weak) signs of magnetic fields, yet only in three of them these features were strong enough to be detected at a 3 σ level. Even in some of the undetected 6 stars, e.g. HD 163336 and HD 224361, there were increased signals in the Stokes V/I spectra near some of the Balmer lines. Since the Zeeman features can only be explained by the presence of a magnetic field, more accurate observations over the rotation periods of the studied stars are needed to confirm the existence of those fields.

References

Babel, J. & Montmerle, T. 1997, A&A, 323, 121
Bagnulo, S., Szeifert, T., Wade, G. A., Landstreet, J. D., & Mathys, G. 2002, A&A, 389, 191
Berghöfer, T. W. & Schmitt, J. H. M. M. 1994, A&A, 292, L5
Borra, E. F. & Landstreet, J. D. 1980, ApJS, 42, 421
Bychkov, V. D., Bychkova, L. V., & Madej, J. 2003, VizieR Online Data Catalog, 340, 70631
Czesla, S. & Schmitt, J. H. H. M. 2007, A&A, 465, 493
Damiani, F., Micela, G., Sciortino, S., & Harnden, Jr., F. R. 1994, ApJ, 436, 807
Donati, J.-F., Babel, J., Harries, T. J., et al. 2002, MNRAS, 333, 55
Eggen, O. J. 1998, AJ, 116, 1314
Feldmeier, A., Puls, J., & Pauldrach, A. W. A. 1997, A&A, 322, 878
Gagne, M., Caillault, J.-P., Stauffer, J. R., & Linsky, J. L. 1997, ApJ, 478, L87+
Gagné, M., Oksala, M. E., Cohen, D. H., et al. 2005, ApJ, 628, 986
Groote, D. & Schmitt, J. H. M. M. 2004, A&A, 418, 235
Hamaguchi, K., Yamauchi, S., & Koyama, K. 2005, ApJ, 618, 360
Harnden, Jr., F. R., Branduardi, G., Gorenstein, P., et al. 1979, ApJ, 234, L51
Herbig, G. H. 1960, ApJ, 131, 632
Houk, N. & Cowley, A. P. 1975, Michigan Catalogue of two-dimensional spectral types for the HD star (Ann Arbor: University of Michigan, Departement of Astronomy, 1975)
Hubrig, S., Bagnulo, S., Kurtz, D. W., et al. 2003, in Astronomical Society of the Pacific Conference Series, ed. L. A. Balona, H. F. Henrichs, & R. Medupe, 114–+
Hubrig, S., Kurtz, D. W., Bagnulo, S., et al. 2004a, A&A, 415, 661
Hubrig, S., Le Mignant, D., North, P., & Krautter, J. 2001, A&A, 372, 152
Hubrig, S., North, P., & Mathys, G. 2000, ApJ, 539, 352
Hubrig, S., North, P., & Schöller, M. 2007a, Astronomische Nachrichten, 328, 475
Hubrig, S., North, P., Schöller, M., & Mathys, G. 2006, Astronomische Nachrichten, 327, 289
Hubrig, S., Pogodin, M. A., Yudin, R. V., Schöller, M., & Schnerr, R. S. 2007b, A&A, 463, 1039
Hubrig, S., Schöller, M., & Yudin, R. V. 2004b, A&A, 428, L1
Kramer, R. H., Cohen, D. H., & Owocki, S. P. 2003, ApJ, 592, 532
Landstreet, J. D. 1982, ApJ, 258, 639
Levato, H., Malaroda, S., Morrell, N., & Solivella, G. 1987, ApJS, 64, 487
Lucy, L. B. 1982, ApJ, 255, 286
Lucy, L. B. & White, R. L. 1980, ApJ, 241, 300
Owocki, S. P. & Cohen, D. H. 1999, ApJ, 520, 833
Schmitt, J. H. M. M., Fleming, T. A., & Giampapa, M. S. 1995, ApJ, 450, 392
Schmitt, J. H. M. M., Groote, D., & Czesla, S. 2005, in ESA Special Publication, Vol. 560, 13th Cambridge Workshop on Cool Stars, Stellar Systems and the Sun, ed. F. Favata & et al., 943–+
Schmitt, J. H. M. M. & Kürster, M. 1993, Science, 262, 215
Schmitt, J. H. M. M. & Liefke, C. 2004, A&A, 417, 651
Schröder, C. & Schmitt, J. H. M. M. 2007, A&A, 475, 677
Seward, F. D., Forman, W. R., Giacconi, R., et al. 1979, ApJ, 234, L55
Stelzer, B., Huélamo, N., Micela, G., & Hubrig, S. 2006a, A&A, 452, 1001
Stelzer, B., Micela, G., Hamaguchi, K., & Schmitt, J. H. M. M. 2006b, A&A, 457, 223
Townsend, R. H. D., Owocki, S. P., & Ud-Doula, A. 2007, MNRAS, 978
ud-Doula, A. & Owocki, S. P. 2002, ApJ, 576, 413
ud-Doula, A., Townsend, R. H. D., & Owocki, S. P. 2006, ApJ, 640, L191
Zinnecker, H. & Preibisch, T. 1994, A&A, 292, 152

List of Objects

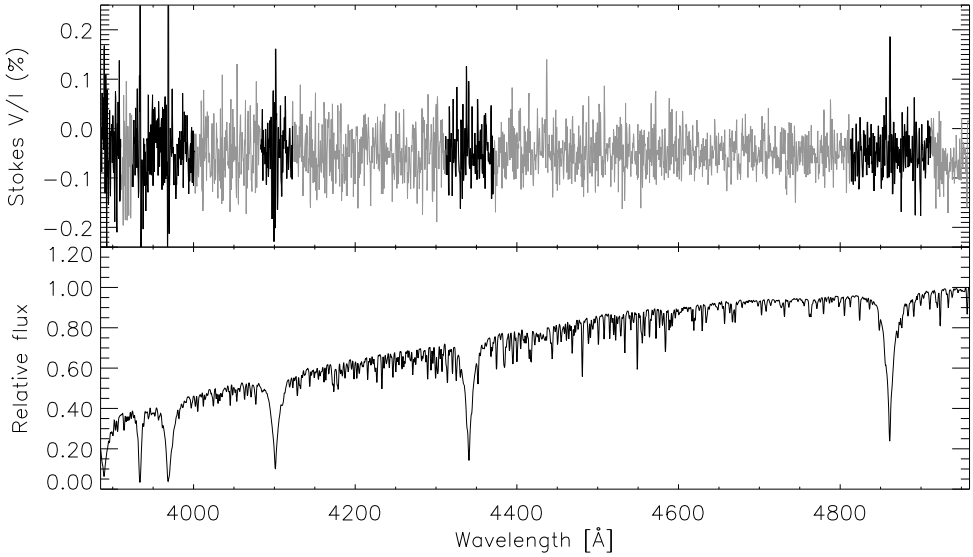

Fig. 2. Stokes V/I spectrum and relative flux of the A4 giant star HD 147084. The black areas in the Stokes V spectrum indicate the regions used for determination of the magnetic fields from Balmer lines. The data shown have been observed with the GRISM 1200B. For comparison see the Herbig Ae/Be star HD 31648 in Fig. 3.

‘ϵ Gru’ on page 3
‘η Tuc’ on page 3
‘o Sco’ on page 3
‘ω Oph’ on page 3
‘γ Equ’ on page 3
‘HD 147084’ on page 4
‘HD 148898’ on page 4
‘HD 159217’ on page 4
‘HD 159312’ on page 4
‘HD 163336’ on page 4
‘HD 172555’ on page 4
‘HD 174240’ on page 5
‘HD 182761’ on page 5
‘HD 186219’ on page 5
‘HD 215789’ on page 5
‘HD 217186’ on page 5
‘HD 224361’ on page 5
‘HD 224392’ on page 5
‘HD 201601’ on page 5

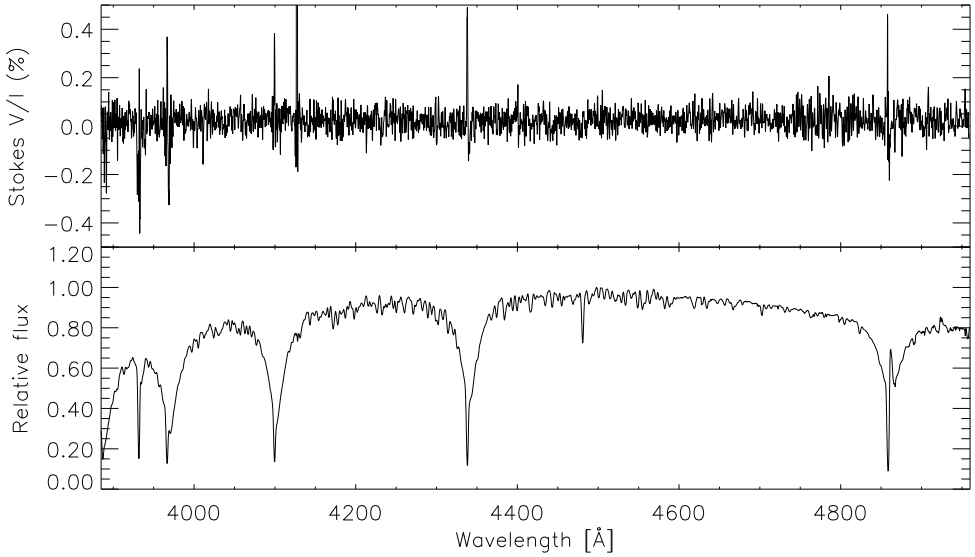

Fig. 3. For comparison with Fig. 2; the Stokes V/I spectrum and relative flux of the Herbig Ae/Be star star HD 31648 observed by Hubrig et al. (2007b). Strong Zeeman features can be found in all Balmer and the CaII K line.

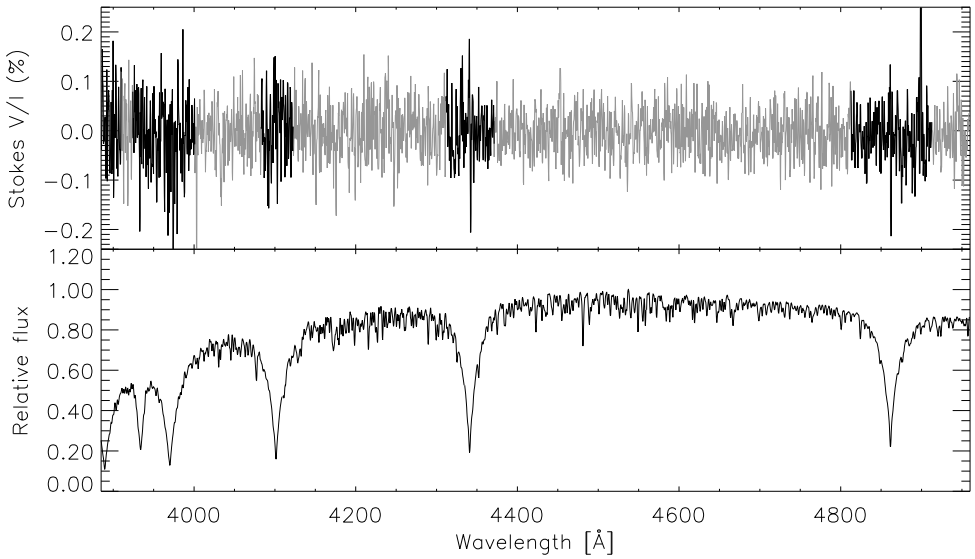

Fig. 4. Stokes V/I spectrum and relative flux of the A7p star HD 148898. The black areas in the Stokes V spectrum indicate the regions used for determination of the magnetic fields from Balmer lines.

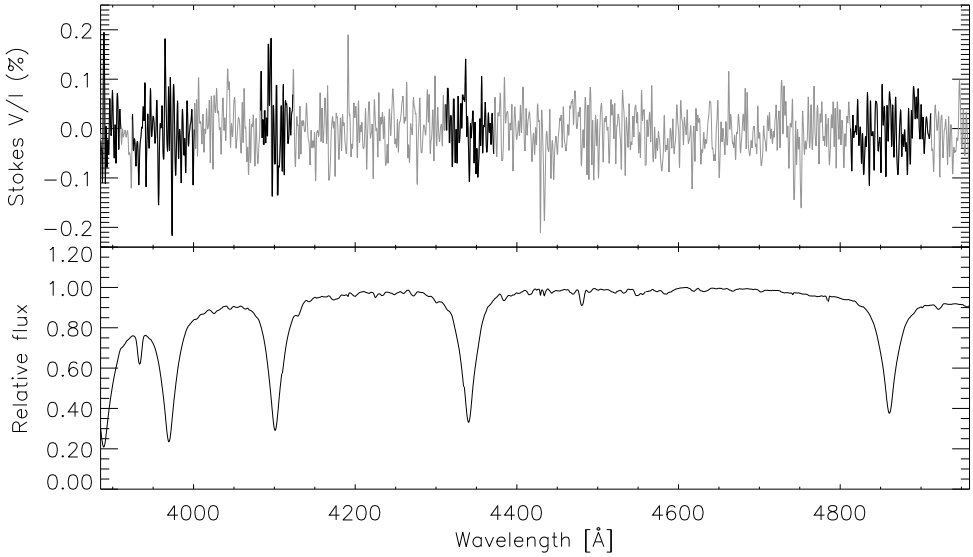

Fig. 5. Stokes V/I spectrum and relative flux of the A0V star HD 159312. The black areas in the Stokes V spectrum indicate the regions used for determination of the magnetic fields from Balmer lines.

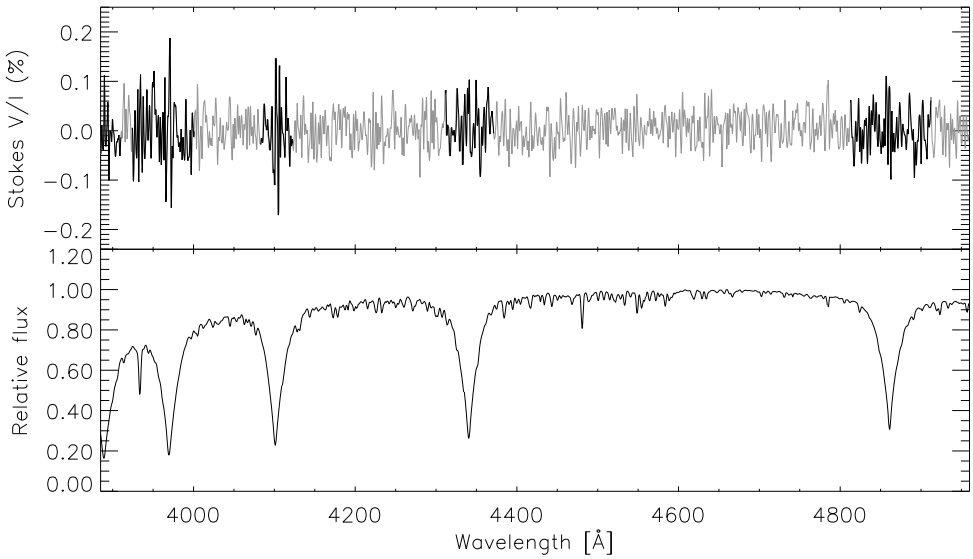

Fig. 6. Stokes V/I spectrum and relative flux of the A0V star HD 163336. The black areas in the Stokes V spectrum indicate the regions used for determination of the magnetic fields from Balmer lines.

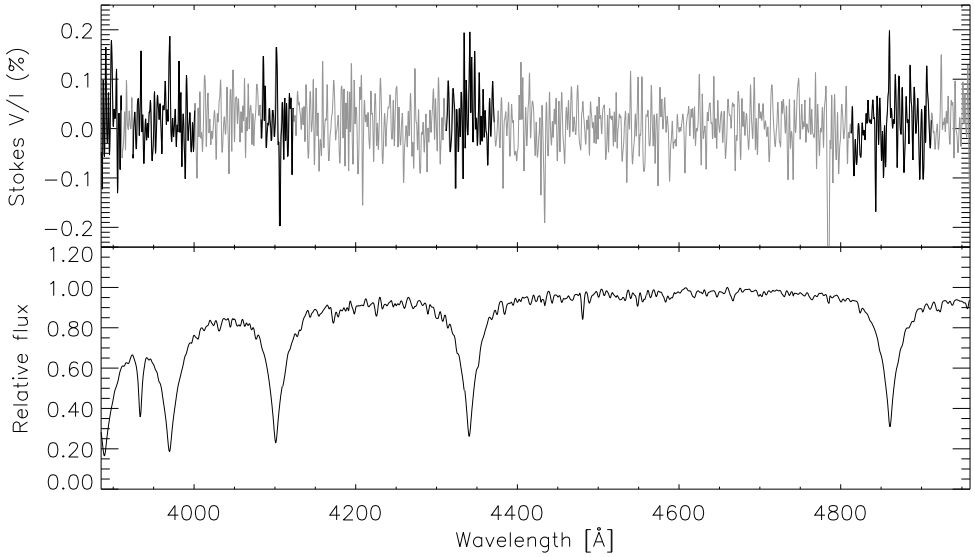

Fig. 7. Stokes V/I spectrum and relative flux of the A1IV star HD 224361. The black areas in the Stokes V spectrum indicate the regions used for determination of the magnetic fields from Balmer lines. The H_β and H_δ lines show a clear Zeeman feature.

Chapter 4

Ca II HK emission in rapidly rotating stars

C. Schröder, A. Reiners and J. H. M. M. Schmitt
submitted to Astronomy & Astrophysics

Astronomy & Astrophysics manuscript no. cameas6j
June 12, 2008

Ca II HK emission in rapidly rotating stars

Evidence for an onset of the solar-type dynamo

Christian Schröder[1], Ansgar Reiners[2], and Jürgen Schmitt[1]

[1] Hamburger Sternwarte, Gojenbergsweg 112, 21029 Hamburg, Germany
[2] Georg-August-Universitaet, Friedrich-Hund-Platz 1, 37077 Göttingen, Germany

Received ... / Accepted ...

ABSTRACT

We present measurements of chromospheric Ca II H&K activity for 481 solar-like stars. To determine the activity we used the Mount Wilson method and a newly developed method which allows to also measure Ca II H&K emission features in very rapidly rotating stars. The new technique determines the activity by comparing the line shapes from known inactive slowly rotating template stars that have been artificially broadened to spectra of rapid rotators. We have analyzed solar-like stars ranging from $T_{\rm eff}$ = 5000 to 7800 K with rotational velocities up to 190 km/s in our sample of FOCES and FEROS spectra. The effects of the rotational broadening on the two methods have been quantified. Our method has proven to produce consistent results where S-Index values are available and offers the possibility to measure the chromospheric activity at the onset of the solar-like dynamo.

Key words. stars: activity – stars: chromospheres – stars: rotation

1. Introduction

Since Olin C. Wilson began his research of stellar activity in 1966 (Wilson 1978), many activity-related projects have been carried out using the Mt. Wilson S-index as a measure for chromospheric activity (Vaughan et al. 1978; Duncan et al. 1991; Baliunas et al. 1998). From 1966 to 1977 the Mount Wilson HK program was carried out with the so-called HKP-1 photometer, which contained a photoelectric scanner at the Coudé focus of the 100 inch telescope. From 1977, the survey was continued with a specially designed photomultiplier, the HKP-2, mounted on the Cassegrain focus of the 60 inch telescope (Baliunas et al. 1995). The data collected during the 'HK Project' laid the groundwork for our current understanding of stellar chromospheric activity.

Further surveys contributed to the pool of activity measurements. Henry et al. (1996) surveyed over 800 southern Sun-like stars and identified four activity classes in their sample, ranging from *very inactive* to *very active*. Between the *inactive* and *active* regime they found a deficiency of stars at intermediate levels of activity, which was confirmed by Gray et al. (2003, 2006) in their NStars project. Another large survey was presented by Wright et al. (2004), who studied the S-index, $R'_{\rm HK}$, chromospheric ages and rotation rates for over 1200 F to M stars. Since 1994, long-term observations obtained with Solar-Stellar Spectrograph (SSS) at Lowell Observatory measured the S-index and absolute flux of the Sun and solar-like stars (Hall et al. 2007).

All of these surveys are based on the same method as used for the Mount Wilson observations. This technique measures the chromospheric activity by determining the flux in $\approx$ 1 Å wide filters in the centers of the Ca II H&K lines. The measured flux is then normalized to the flux in two continuum filters placed shortward and longward of the Ca II H&K lines. A known drawback of this method is the fact that it can only be applied to slowly rotating stars. For the rapid rotators the wings of the Ca II H&K lines wings fill up the center of the absorption line and mimic emission flux, and also emission line flux in the core is lost due to rotational line broadening. Since, first, according to the rotation-activity paradigm the fast rotators should be the stars with the largest activity, and second, fast rotators are often found among the late A and F-type stars, it is highly desirable to have a method producing an S-index value also for such objects. In addition, with the currently available high resolution échelle spectrographs, which often cover the whole visual wavelength range, many serendipitous observations of the Ca II H&K lines are frequently available, which can be utilized for surveys of chromospheric activity. In this paper we therefore present a new method to measure Ca II HK emission features in very rapidly rotating stars by comparing the line shapes from known inactive slowly rotating template stars that have been artificially broadened to those of fast rotators.

In Sect. 2, we present the observational data used to measure the Ca II activity and the methods applied to obtain the basic data for our stars. Sect. 3 contains the descriptions of the classical Mount Wilson method and our new template method. In Sect. 4 we analyze the influence of rotational broadening on the classical and the new template $R'_{\rm HK}$ values and present the results of our activity measurements. Sect. 5 contains a summary and the conclusions.

2. Observational data

The sample of spectra we used for our Ca II H&K measurements is comprised of three different subsamples of archived data originally acquired for different scientific purposes. The first collection of 74 spectra was observed in April 2002 with the FEROS instrument at the ESO 1.52 m telescope at La Silla. FEROS is

Send offprint requests to: Christian Schroeder e-mail: cschroeder@hs.uni-hamburg.de

an échelle spectrograph (Kaufer et al. 1999) with a resolution of R = 48000 providing an almost complete spectrum in the range of 3500 to 9200 Å. The second sample of 155 spectra was observed in December 2003 and April 2004, again with the FEROS instrument, which in the meantime had been moved to the MPG/ESO 2.2 m telescope to enhance performance. This collection of spectra was part of a radial velocity measurement program from J. Setiawan. Due to this scientific goal, this sample of stars is biased towards slower rotational velocities. Both FEROS spectra samples yield a signal-to-noise ratio of at least 200 in the continuum around 6000 Å. The last collection of 252 spectra was observed in February 2002, March 2004 and August 2004 with FOCES at the 2.2 m telescope on Calar Alto (Spain). FOCES is again an échelle spectrograph, that can be mounted at the Cassegrain focus on either the 2.2 m or 3.5 m telescope at the DSAZ (Calar Alto, Spain). Its spectral resolution reaches, depending on the setup, up to R = 40000. The signal-to-noise ratio in this sample is at least 100 in the continuum. We note a possible bias towards higher rotational velocities in the first FEROS and the FOCES sample, which have been observed in a campaign to study differential rotation. In this campaign stars with a rotational velocity of 30 km/s and more have been observed with high priority, while the slow rotators were added later during the campaign. Therefore, we cannot rule out a bias towards higher rotational velocities in two of our three subsamples. A detailed description of the observations can be found in Reiners & Schmitt (2003a).

Since our method uses spectra of inactive template stars to measure the Ca II H&K activity and the templates are selected based on $T_{\rm eff}$ and log g of the star, these fundamental parameters are required for all stars in our sample. We used literature data whenever available, and to determine the required values for those stars without literature data, we used tools based on uvbyβ photometry. Moon & Dworetsky (1985) compared the observed colours and indices for B, A and F stars of known $T_{\rm eff}$ and log g with synthetic colors, calculated by Relyea & Kurucz (1978) and Schmidt & Taylor (1979). Further improvements on the grids used in this method have been applied by Napiwotzki et al. (1992). The determined effective temperatures in our sample range from 5000 to 7800 K and are in good agreement with the values given by Nordström et al. (2004).

The v sin(i) values of our sample have been determined using a Least Square Deconvolution method (LSD), which is based in the analysis of the zeros of the Fourier transformed line profile; further details about the extraction of v sin(i) from high resolution spectra can be found in Reiners & Schmitt (2002, 2003b). For the slowest rotators (v sin(i) $\leq$ 4 km/s), the application of this method becomes difficult and the measurements represent upper limits. The v sin(i) values not listed by Reiners & Schmitt (2002, 2003b), were taken from the Glebocki & Stawikowski (2000). In Fig. 1 we shows the v sin(i) values vs. the $B-V$ color index in our sample; as is expected and obvious from Fig. 1, there exist many rapid rotators among the stars with $B-V < 0.6$, for which one would like to obtain a quantitative measurement of their chromospheric activity.

The classical Mount Wilson method to measure the log $R'_{\rm HK}$ values cannot be applied to evolved stars, since the photospheric contribution to the measured flux has not been determined for giants. In these objects the photospheric contribution is lower than in main-sequence stars. Since the depths of the absorption and therefore the photospheric correction depends on the surface gravity, the photospheric correction for giants has to be determined for different evolutionary stages, which has not been done so far. To identify the evolved stars in our sample, we determined their position in the Hertzsprung-Russell diagram (see Fig. 2). The absolute luminosities were taken from Nordström et al. (2004) or calculated based on the Hipparcos parallaxes for the stars not listed in Nordström et al. (2004). We plotted the luminosity classes according to Allen (1976) as solid lines. All stars brighter than luminosity class IV are treated as giant stars with respect to the classical method. For these stars, we only give the S values of the classical method and not the log $R'_{\rm HK}$. Stars with luminosity class V to IV are treated as main-sequence stars in terms of the application of the Mount Wilson method and are listed with both the S index and the log $R'_{\rm HK}$ values.

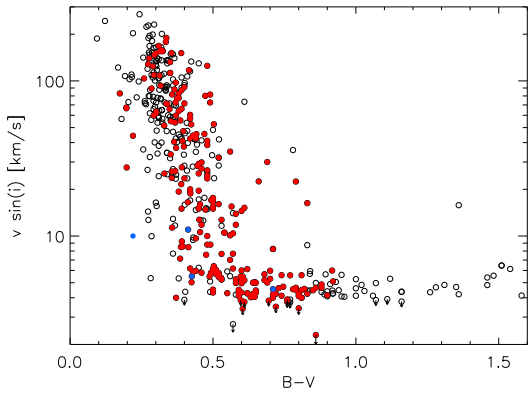

Fig. 1. Rotational velocity plotted over B-V color for the 481 stars in our data sample. The red colored symbols represent those 238 stars with activity measurements based on high-quality fits of the star spectrum on an inactive template star spectrum. Indicated by the filled blue circles are stars which have been chosen as template stars.

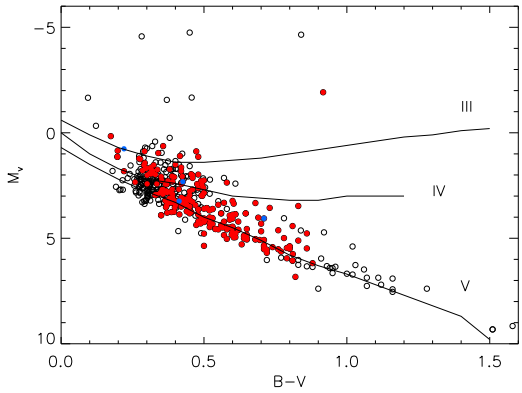

Fig. 2. Color-magnitude diagram for the 481 stars in our data sample. The black circles represent the 481 stars with activity measurements with the Mount Wilson method. The filled red circles are those stars with an additional template method measurement and stars chosen as templates are represented with filled blue circles. Indicated by the solid lines are the luminosity classes according to Allen (1976).

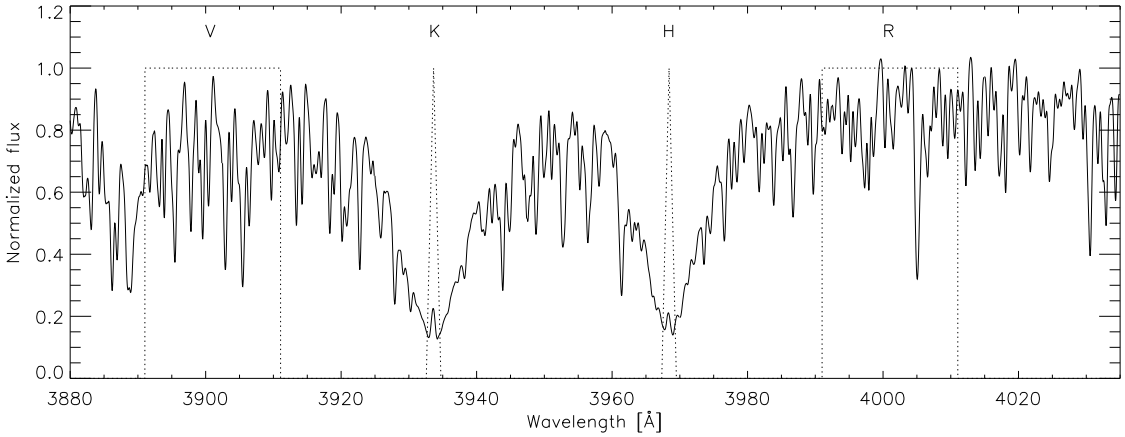

Fig. 3. The two triangle-shaped line filters and the continuum filters used to calculate the Mount Wilson S index shown in a normalized FEROS spectrum of the slowly rotating F7V stars HD 48676.

3. Method description

3.1. Classical S-Index, log R'_{HK} and the Rossby number

The S-index was introduced by Vaughan et al. (1978) as a dimensionless indicator for the Ca II activity measured by the Mount Wilson Observatory (MWO) HKP-1 and HKP-2 spectrometers. The HKP-2 instrument, which laid the groundwork for following Ca II surveys, measured the flux in two 1.09 Å wide H and K bandpasses and normalized it to the flux in two 20 Å wide continuum filters placed at 3901 and 4001 Å, referred to as V and R; in Fig. 3 we show the position and the size of the various filters for the case of the slow rotator HD 48676. The S-index values were constructed as

$$S = \alpha \frac{H+K}{R+V}, \quad (1)$$

where H, K, R, and V are the values for the flux measured in the according bandpasses (cf., Fig. 3) and α is an instrumental calibration factor. This calibration is necessary to adjust the measured activity indices from the two spectrometers HKP-1 and HKP-2. Values for α range from 1.3 (Cincunegui et al. 2007) to 5 (Gray et al. 2003).

Since the flux measured in the core of the Ca II lines is normalized to the continuum flux, the S-index is independent from the color of the star. Clearly, in the hypothetical case of a totally inactive star there is also a photospheric contribution to the H and K flux measurements and hence the S-index. To remove the color independence and the photospheric component, Middelkoop (1982) developed a transformation of the S index into a value R_{HK} as a function of $B-V$ based on 85 main sequence stars:

$$R_{HK} = 1.34 \times 10^{-4} C_{cf} S. \quad (2)$$

Rutten (1984) improved this relation for the conversion factor C_{cf} given by Middelkoop (1982) and extended the range of observed stars to $B-V = 0.3$. With the additionally observed 30 main-sequence and 27 giant stars, they found improved fits through

$$log\ C_{cf} = 0.25(B-V)^3 - 1.33(B-V)^2 + 0.43(B-V) + 0.24 \quad (3)$$

for main-sequence stars with $0.3 \leq B-V \leq 1.6$, and

$$log\ C_{cf} = -0.066(B-V)^3 - 0.25(B-V)^2 - 0.49(B-V) + 0.45 \quad (4)$$

for giants with $0.3 \leq B-V \leq 1.7$. The improvements in this new relation is based on the larger number of stars, especially on the blue side of the samples, and the underlying relations for $B-V$, T_{eff} and BC. A comparison between the conversion factors given by Rutten (1984) and Middelkoop (1982) is shown in Fig. 4. As the plot shows, the difference between the conversion factors is small, in particular for hotter stars. We used the relation given by Rutten (1984), since it was determined based on a broader color range.

To correct for the photospheric contribution to the flux in the Ca II line cores Hartmann et al. (1984) derived the expression

$$log\ R_{phot} = -4.898 + 1.918(B-V)^2 - 2.893(B-V)^3 \quad (5)$$

in the range of $0.44 < (B-V) > 0.82$, which provides the photospheric term for the correction

$$R'_{HK} = R_{HK} - R_{phot}\ . \quad (6)$$

For $B-V > 0.82$ the photospheric contribution is still in good agreement with equation 5 and, as reported by Noyes (1984), becomes negligible for $B-V \geq 1$. Noyes (1984) found an empirical fit between the Rossby number and the emission ratio R'_{HK} through

$$log\ (P/\tau_c) \equiv f(R'_{HK}) = 0.324 - 0.4\ log\ R_5 - 0.283(log\ R_5)^2 - 1.325(log\ R_5)^3 \quad (7)$$

where R_5 is defined as $R'_{HK} \times 10^5$ and τ_c is the convective turnover time based on the ratio of mixing length to scale height

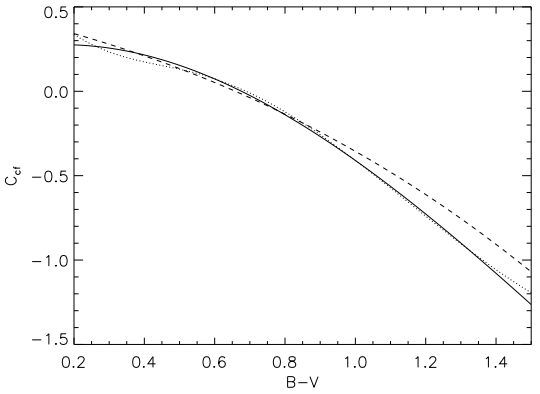

Fig. 4. Comparison of the different conversion factors as a function of B-V. The solid line shows the conversion factor for main-sequence stars (specified in the range of 0.3 ≥B-V≤1.6), the dashed line shows C_{cf} values for giants (0.3 ≥B-V≤1.7), both lines according Rutten (1984), and the dotted line the values according to Noyes (1984) for the main-sequence (0.45 ≥B-V≤1.5).

$\alpha = 2$. By placing a fit to a log $P_{obs} - f(R'_{\rm HK})$ over B-V plot, they derived a corrected convective turn-over time

$$log\ \tau_c^{(2)} = \begin{cases} 1.362 - 0.166x + 0.025x^2 - 5.323x^3 & , x > 0 \\ 1.362 - 0.14x & , x < 0. \end{cases} \quad (8)$$

In this case, x is defined as $x = 1-(B-V)$ and the ratio of mixing length to scale height is 1.9. With the convective turnover time $\tau_c^{(2)}$ and and a given rotational period P it is possible to define a dimensionless Rossby number $Ro = P_{obs}/\tau_c^{(2)}$, which was determined empirically by Noyes (1984) and allows a significantly better description of the chromospheric activity than rotational velocity or rotation period alone.

3.2. Template method

A known problem of the Mount Wilson S-index is the fact that for rapidly rotating stars the measured S-index is influenced by the broadening of the line wings and the core emission feature. This rotational effect limits the classical method to slowly rotating stars. Especially activity measurements of rapidly rotating late A- and early F-type stars, where the onset of the magnetic dynamo occurs, are susceptible to rotational broadening. Fig. 1 clearly shows the well-known increase of the rotational velocities for the stars with $B - V < 0.5$, so clearly one needs a way to obtain S-indices independent of rotation of a star.

The idea behind our method is the fact that even in highly broadened spectra the difference between active and inactive stars should be detectable, given a sufficiently high signal-to-noise ratio in both spectra and a reasonable agreement in $T_{\rm eff}$ and log g. The calibration of the spectra and the measurement of the activity are divided into several steps. First, both the target and template stellar spectra are normalized and wavelength calibrated in the usual way. In a second step, the template spectrum is normalized with a first order polynomial to the stars spectrum in the wings of the H line. Here we focused on the Ca II H line, because the K line is much more sensitive to differences between the template and target star in log g and $T_{\rm eff}$. We obtain this polynomial by calculating the ratio between the template and the star spectrum in a number of 0.5 Å wide areas. These areas are equally spread over two 4.5 Å wide regions, which are located on the red and blue side of the line and cover the wavelength range from 3961.25 to 3965.75 Å in the blue wing and from 3974.25 to 3978.75 Å in the red wing. Both fitting areas are indicated in Fig. 5 and 6. The right fitting region is positioned on the far wing of the K line to prevent any influence of the H I line at 3971.2 Å on the measurements of the hottest stars in our sample.

Table 1. List of template stars

HD	$T_{\rm eff}$	log g	v sin(i)	temperature range	Id
128620	5627	4.17	4.5	< 6200 K	1
143790	6270	3.93	5.5	6200 - 6900 K, log $g < 4$	2
104731	6572	4.26	11.0	6200 - 6900 K, log $g > 4$	3
36876	7567	3.67	10.0	> 6900 K	4

In the third step we identify the maxima for both the template and the star spectrum in each of the eighteen 0.5 Å wide fitting areas and calculate their ratio. Since the mean or the median are influenced by differences of the line depths caused by different metallicities of the template and the star, the maxima lead to better fit results. The polynomial is then obtained as a first order fit to this array of ratios. By dividing the template by this polynomial in the appropriate wavelength range, we correct for the last differences between the two spectra remaining after the normalization of the template and the target star's spectrum. The results of the fitting process is shown in Fig. 5 and 6. In Fig. 5 the slowly rotating G2V star HD 102365 is compared to the template star HD 128620. Since both stars are slow rotators, the fitting process does not include any artificial broadening. For the F3IV-V star HD 186005, which rotates with 150 km/s, the template spectrum has to be strongly broadened. Fig. 6 shows the spectra of the target star and the template before the fitting process in the top and center plot, as well as the result of the broadening and fitting process in the bottom plot.

To measure the Ca II H&K emission in the fourth step, the integral over a given area in center of the line was calculated for the target star and the template. The extraction area has to be large enough to cover even strongly broadened emission features. To reduce the effect of different metallicities, we chose a variable extraction width of at minimum 2 Å width around the center of the line for very slowly rotating stars, and broaden the extraction width according to the red- and blueshift of the rotational velocity. Since the wings of the Ca II H line is populated with various Fe I lines, the variable extraction width reduces the noise in the measured emission. To exclude any possibly remaining B-V dependent effects and stay consistent with the classical S values, the difference of the two integrals is then normalized to the equivalent width of the continuum in two continuum filters (see Fig. 3). These continuum filters are the same as in the S-index calculations presented by Vaughan et al. (1978). To stay as close as possible to the classical S index, we then multiplied our retrieved $S_{\rm template}$ value from the H line by a factor of two.

To convert our S-indices into the color dependend log $R'_{\rm HK}$ values in the last step, we used the conversion factor C_{cf} from Rutten (1984) given in equation 3, since a significant fraction of our sample is located in the range of $B - V \leq 0.4$. For these stars, the conversion factor presented by Rutten (1984) is based on more observational data and therefore better defined values for the hotter stars than the conversion factor presented

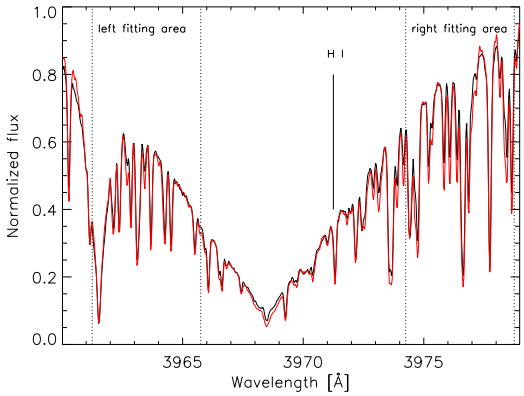

Fig. 5. An example of a fitting result for the slowly rotating G2V template star HD 128620 to the G2V star HD 102365. Shown in the plot are the areas for the foot points for the line wing fitting and the position of the H I line at 3971.2 Å. The difference in log g is 0.7 and there is no significant temperature difference.

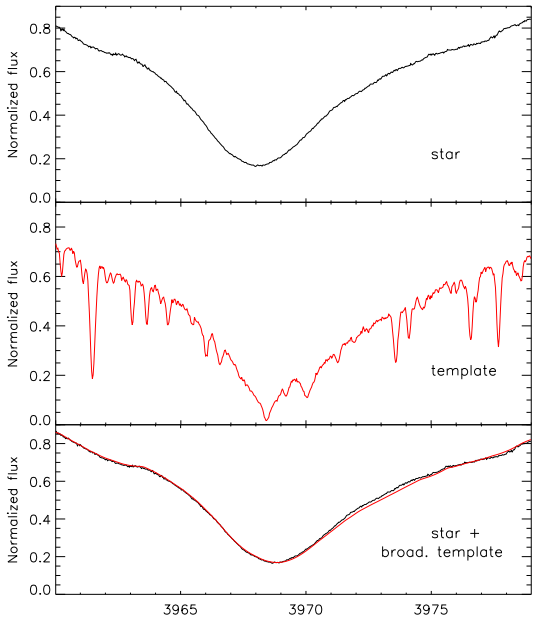

Fig. 6. An example of a fitting result for a rapidly rotating star. From top to bottom: the F3IV-V star HD 186005, the F0IV template star HD 36876 and the result of the fitting process. The differences are 580 K in $T_{\rm eff}$ and 0.14 in log g, and the rotational velocity of HD 186005 is 150 km/s.

by Middelkoop (1982) and Noyes (1984). For the giants in our sample we used equation 4. Since our method already substracts the photospheric contribution to the flux with the template, we do not need to correct for the photospheric flux.

The template stars and their $T_{\rm eff}$, log g and v sin(i) values are given in Table 1. The selection criteria for these stars were slow rotational velocity and that the stars should be as inactive as possible. Additionally, the log g values of the templates cover a large fraction of the log g values given in our sample. The application of these criteria resulted in the selection of the given four template stars. With this selection of template stars we are able to measure S-indices in about 50% of the stars in our sample. For the stars without template measurements the difference in log g and $T_{\rm eff}$ is too large to give an acceptable fit result. Additional templates covering the missing values of log g and $T_{\rm eff}$ would allow us to measure a large fraction of the missing stars. A possible source for template spectra are obviously synthetic spectra. We actually did compute the missing spectra with PHOENIX (Hauschildt & Baron 1999), however, we found systematic differences in the line wings between synthetic and observed spectra and therefore chose to only use observed template spectra.

3.2.1. Uncertainties

Based on visual inspection of the individual fit results we estimate an uncertainty of about 0.03 for our derived $S_{\rm template}$ values. This uncertainty is caused by noise in the spectra, especially in the line core, inaccuracies in the spectral fits and differences in log g and $T_{\rm eff}$ between the template and the target star. In the following we analyze the different contributions to the measurement errors.

We investigate the impact of the noise on the measured activity by adding a artificial noise to a high quality fit. The effect of the noise is that the template is fitted to the noise peaks in the line wings (see Sect. 3.2), which leads to a lower activity measured in the line core. If we lower the signal-to-noise ratio to a value of 10 for HD 102365, we find a decrease of the $S_{\rm template}$ value by 0.003 compared to the original spectrum, which leads to the conclusion that the noise is only a minor fraction of error.

To test the influence of the difference in log g and $T_{\rm eff}$ and therefore the effect of an inadequate template, we measured the activity for deliberately poorly fitting templates. For the stars presented in the Figures 5 and 6, HD 102365 and HD 186005, we found variations of the measured $S_{\rm template}$ of 0.01 if we choose the next hotter or cooler template respectively. Going one step further and using the hottest template star HD 36876 with $T_{\rm eff}$ = 7567 K to measure HD 102365 ($T_{\rm eff}$ = 5624 K) results in $S_{\rm template}$ = 0.036. Changing the template to a lower log g results in a variation of $S_{\rm template}$ of 0.01 for the highest difference of 0.95. Hence, the selection of the template and therefore the difference in temperature and surface gravity, is the largest contribution to the uncertainty.

According to the given contributions to the uncertainty, we make the conservative assessment that stars with an emission excess $S_{\rm template} \leq 0.03$ still count as inactive as the selected template star. The application of equation 3 and 4 results in log $R'_{\rm HK}$(template) values from -5.5 to -5.0 for our most inactive stars, depending on the color of the target star.

4. Results

In the following section, we present the results of the measurements with the Mount Wilson method, which were obtained to compare the classical method with the results of our new template method. The results of the MWO method a presented in Sect. 4.1. Additionally, the influence of the rotational broadening on the log $R'_{\rm HK}$ values and a comparison between the Mount Wilson S-index and the template S-index determinations are discussed in Sect. 4.2.

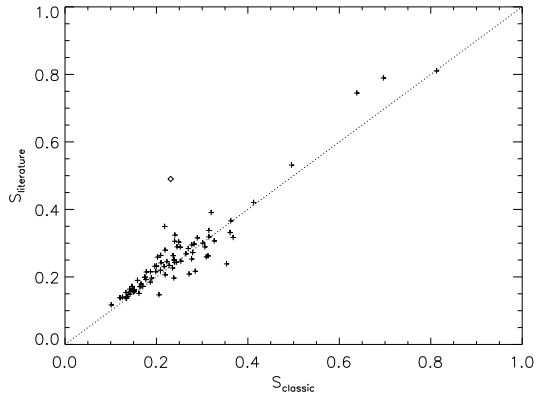

Fig. 7. S values for our sample determined with the Mt Wilson method plotted over the S values presented in the literature. The diamond symbol represents the BY Dra-type variable ϵ Eri.

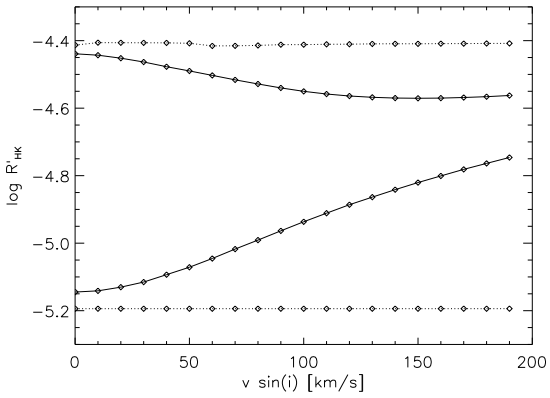

Fig. 8. Projected rotational velocity vs. chromospheric activity in log R'_{HK} measured with the classical Mt. Wilson method and the template method. The solid lines represent the data for the classical method and the dotted lines show the values for the template measurements. As the inactive star, we chose the template star HD 128620. To show the influence on an active star, we included an artificial Ca II H&K emission feature in the spectrum of HD 128620.

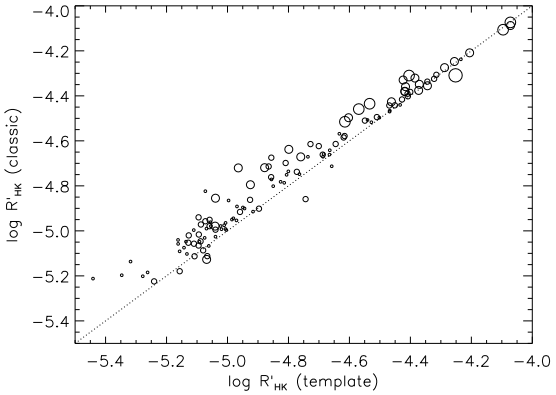

Fig. 9. Classical R'_{HK} values plotted over template R'_{HK} values for main-sequence stars with $B - V \geq 0.44$. The size of the symbols represents the v sin(i) values of the stars. With increasing v sin(i), the rotational effect shifts the classical R'_{HK} away from identity to higher values.

4.1. Comparison to previous measurements

To determine the reliability of our new activity measurements we calculated the S-indices via the Mt. Wilson method for all of our sample stars. The H and K filters were simulated by an appropriate triangular shaped function. After multiplying the spectrum with the filter function, we normalize the integral of the Ca II H and K lines with the integral over the continuum filters V and R. To determine the factor α in equation 1 for our data, we performed a linear least-squares fit between the S-indices of stars with previous measurements presented in Baliunas et al. (1995) and our newly calculated (classical) S-indices. For our sample stars we require an α-value of 1.07 to obtain S-indices consistent with the published literature data. The result of our calibration is presented in Fig. 7. As the plot shows, the classical measurements are in good agreement with the literature data. We attribute the remaining rms scatter of 14% to the intrinsic variability of the stars.

This interpretation is supported by a detailed analysis of the star with the largest discrepancy. Represented by the diamond symbol in Fig. 7 is the BY Dra-type variable ϵ *Eri*, which is known to be a highly variable object. From our data we obtained an S-index of 0.23, which is significantly lower than previously published values. Duncan et al. (1991) presented data from more than 1000 observations, in which the S-indices varied from 0.49 to 0.64, with the higher values towards the beginning of the observations around 1970 and the lower values concentrated around 1980. However, Henry et al. (1996) found S-indices of ∼0.35 in the spectra observed in 1992 and 1993 with the Cerro Tololo InterAmerican Observatory (CTIO), and Hall et al. (2007) presented observations from 1994 to 2006, which are in agreement with the data from Henry et al. (1996). With our measurement of $S = 0.23$ we seem to have measured ϵ *Eri* in an exceptionally low state of activity. Note in this context that the presented S-index is based on a single measurement, while the literature data represent on a large number of observations.

4.2. Influence of rotational broadening

The main advantage of our new method is the fact that it returns precise S-indices also for rapidly rotating stars. This is demonstrated in Fig. 8, where we compare the log R'_{HK} values obtained from two different methods. We chose the (template) star HD 128620 and determined its classic and new log R'_{HK} values by artificially spinning it up in steps of 10 km/s up to a maximum v sin(i) of 190 km/s, thus creating essentially a rapidly rotating inactive star and performing the analysis as described in Sect. 3.1 and 3.2. In order to study the effects of line smearing we also included an artificial emission feature in the spectrum of HD 128620 and carried out the same analysis as before. The resultant log R'_{HK} values are displayed in Fig. 8 as a function of v sin(i). The log R'_{HK} values derived from the MWO method are represented by the bold solid lines while the values derived from the template method are shown as dotted lines. As Fig. 8 demonstrates our new method yields the same log R'_{HK} values both for the active and inactive star independent of the rotation rate of the object. In contrast, the observed activity for a low activity star

derived with the MWO method increases with increasing rotational velocities due to the filling of the line with flux from the line wings, and decreases for a high activity star with increasing rotational velocities. Specifically, the measured log R'_{HK} for the unbroadened low activity spectrum is -5.15, which corresponds to a *very inactive* stars, given the four activity regions defined by Henry et al. (1996). Between 30 and 40 km/s, the increase of the activity due to the contribution of the line wings shifts this object into the regime of the *inactive* stars at log R'_{HK} = -5.1. At the rotational velocity of the most rapid rotator in our sample, which is about 180 km/s, we obtain a flux increase of around 0.25 dex, which would classify this star an *active* star with a log R'_{HK} value of -4.75. The log R'_{HK} value of -4.4 of our active star is seen to decrease with increasing rotational velocity due to the fact that the loss of flux from the broadenend emission core more than compensates the filling up of the lines with the flux from the line wings. Only at the very highest rotational velocities above 150 km/s, where the emission core extremely flattened, the decrease of log R'_{HK} is stopped and the measured activity stays constant. The overall change of log R'_{HK} from the unbroadened to highly broadened spectra is, compared to the influence on an inactive star, relatively small, with a Δ log $R'_{HK} \simeq 0.2$.

We now apply the two methods to real data and compare the difference between the classical log R'_{HK} values and the log R'_{HK} values obtained by the template method as shown in Fig. 9. In this plot the size of the symbols represents the rotational velocity of the the star, the step sizes of the symbols are v sin(i) < 5 km/s, 5 > v sin(i) < 12 km/s, 12 > v sin(i) < 30 km/s, 30 > v sin(i) < 65 km/s and v sin(i) > 65 km/s. The effects of rotational broadening are clearly visible in Fig. 9. For the classical method the measured log R'_{HK} values strongly depend on the rotational velocity. In the inactive regime the slowly rotating stars are found near the dotted line, which indicates identity. The faster a star rotates, the larger is the distance to the dotted line due to the rotational effect on the inactive stars. In the more active regime the difference becomes smaller even for rapidly rotating stars. This is the same phenomenon as in the measurements for an active star in Fig. 8.

The rotational influence on the log R'_{HK} values as described above does not cause a problem for most of the solar-like main-sequence stars with $B-V \geq 0.44$, which is the borderline of the previous Ca II H&K surveys. This is due to the fact that most stars in this color range do not rotate fast enough to suffer a significant change in the measured activity (see Fig. 1). Only the youngest stars, which have not yet lost their angular momentum due to magnetic breaking, rotate fast enough to show a rotational effect in the log R'_{HK} values. The fastest object in our sample in this color regime is HD 199143, which is an F8V star with v sin(i) of 125 km/s and a supposed member of the $\sim$ 12 Myr old β Pic moving group (Kaisler et al. 2004). Since HD 199143 is an highly active star, the effect on the measured activity caused by the rotational velocity is small, because the decrease of flux due to the broadening of the emission feature is compensated by the flux of the line wings (see the upper solid line in Fig. 8). However, for the early stars in the range of $B-V \leq 0.4$, the emission is supposed to decrease on the basis of decreasing dynamo efficiency, which leads to a higher impact of the rotational influence. For these stars, the expected effect is described by the lower solid line in Fig. 8.

4.3. Classical and template log R'_{HK} determinations

Noyes (1984) were the first to empirically show the correlation between Rossby number and activity (as measured through log R'_{HK}) and hence provide more or less direct evidence for dynamo related activity in late-type stars. It is clearly desirable to extend these studies to the earliest possible late-type stars. In Fig. 10 we therefore plot the classical and the template log R'_{HK} values over the Rossby number for those main-sequence stars with $B-V > 0.44$. The classical values are represented by black circles and the template value are shown in filled red circles. Evolved objects or stars outside the given color range are left aside for two reasons: First, the convective turnover time is unknown for the evolved stars and becomes very small, according to equation 8, for the earliest stars in our sample. The second reason is the fact that the photospheric contribution R_{phot} is unknown for these stars, too. We also indicated (by the dotted lines in Fig. 10) that area, where the stars in the Noyes (1984) sample are located. In our data we find a number objects at higher

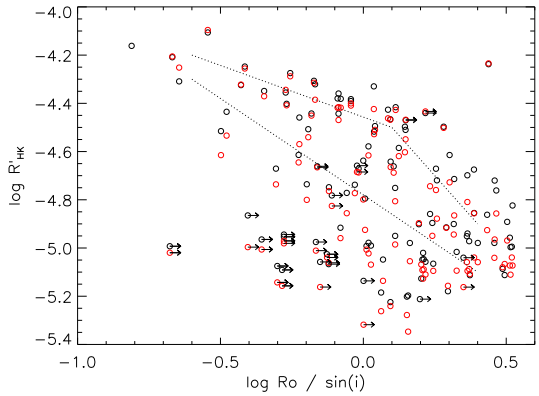

Fig. 10. Classical (black) and template (red) R'_{HK} values for main-sequence stars plotted over the Rossby number. The color range is limited to $B-V > 0.44$. Arrows indicate the upper limits for stars with v sin(i) $\leq$ 4 km/s. The dotted lines represent the upper and lower activity limit of the sample stars presented by Noyes et al.(1984).

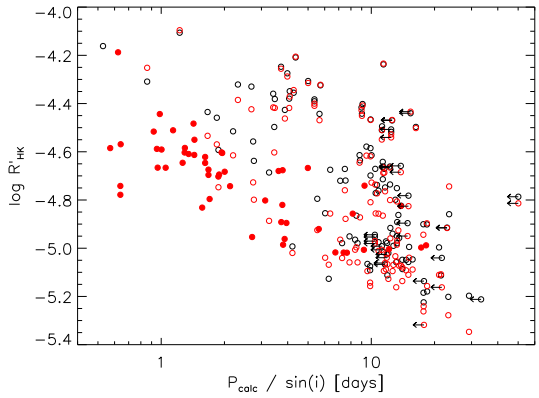

Fig. 11. Classical (black) and template (red) R'_{HK}values for main-sequence stars with plotted over the calculated period. For the classical measurement, the color range is limited to $B-V > 0.44$, while the template values are given for all measured main-sequence stars. The filled red circles are the template measurements for stars with $B-V < 0.44$. Arrows indicate the upper limits for stars with v sin(i) $\leq$ 4 km/s.

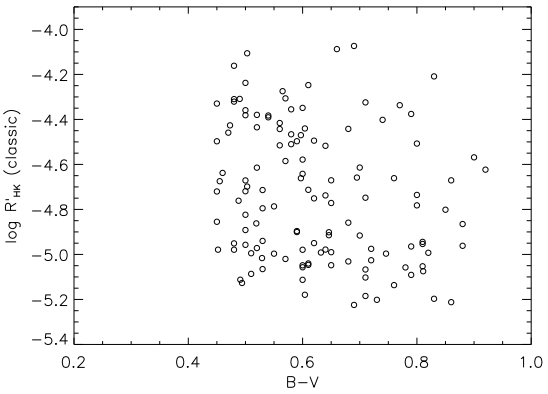

Fig. 12. Classical $R'_{\rm HK}$ values for main-sequence stars plotted over B-V for stars with $B-V \geq 0.44$.

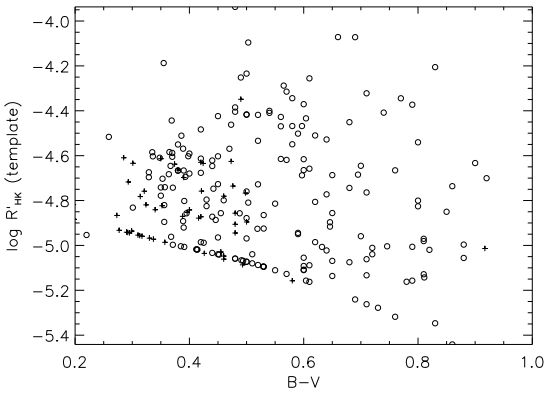

Fig. 13. Template $R'_{\rm HK}$ values plotted over B-V. Main-sequence stars are represented by circles, giant stars with '+' symbols. The B-V values range from 0.22 to 0.92. A clear decrease in Ca II H&K activity can be seen in the hottest stars of the sample.

Rossby numbers than the values in the Noyes sample. This can be explained by the effects of inclination. Since the periods we used to determine the Rossby number for our sample are calculated from the v sin(i) values and the inclinations of our sample stars are unknown, the calculated Rossby numbers are by necessity upper limits. In addition to the objects with high Rossby numbers, we see several inactive stars with relatively small log (Ro / v sin(i)) values. For these objects, the determined rotational velocity values in the range range of 4 km/s are in fact upper limits. Therefore, these late G to K dwarfs might have lower rotational velocities, which would shift them to higher Rossby numbers. The main point shown by Fig. 10 is the good agreement between the measured log $R'_{\rm HK}$ values derived with the classical and template method for the late F to K stars. The differences between the classic and the template values are caused by the rotational effect, as can be seen in Fig. 9. Stars located above the dotted identity line in Fig. 9 are stars with noticeable difference between the classical and the template values in Fig. 10. Given the limitations of our calculated periods we are able to reproduce the rotation-activity relation presented by e.g. Noyes (1984).

Having shown the consistency of our rotation-activity relations for stars with $B-V > 0.44$ with previous work we can now extend these relations to stars in the range of $B-V < 0.44$ we plot (in Fig. 11) the classical and the template log $R'_{\rm HK}$ values vs. the calculated period P_{calc}. We now choose the calculated periods as activity parameters since the small convective turn-over times for stars with $B-V < 0.44$ lead to very large uncertainties in the inferred Rossby numbers. In Fig. 11 the classical values for stars with $B-V > 0.44$ are plotted in black circles, the values for the template method in the same color range in red circles and the template values for the stars with $B-V < 0.44$ in filled red circles. As is clear from Fig. 11, the increase in activity towards smaller rotational periods is less steep than in the late F-K stars. For periods longer than 10 days, the early F stars are located in the lower half of the activity distribution. On the other hand, for the rapidly rotating stars with periods of about 1 day, nearly all of these objects are significantly less active than the corresponding later type stars with the same rotation period.

In order to illustrate the color dependence of the derived log $R'_{\rm HK}$ measurements we show (in Fig. 12) the log $R'_{\rm HK}$ values (derived from the MWO method) vs. $B-V$ color index. Only stars with $B-V > 0.44$ are shown, because for bluer stars the photospheric contribution to the S-index is undefined. Using our new template method we can extend this study to bluer stars as shown in Fig. 13, where we plot the log $R'_{\rm HK}$ values derived from the template method vs. $B-V$ color index. For the stars with $B-V \geq 0.5$ we find a similar distribution of the measured activity as with the Mount Wilson method, however, for the stars with $B-V \leq 0.5$, there is a clear decrease in maximum activity. This decrease in Ca II H&K activity occurs in the same temperature range as the ratio between X-ray luminosity and bolometric luminosity L_X/L_{bol} (Schmitt et al. 1985) and the fraction of X-ray detection (Schröder & Schmitt 2007). The onset of the chromospheric activity is located in the range of $0.1 \leq B-V \leq 0.2$, which corresponds to spectral type A7-8V. We attribute this rise in maximum activity from spectral type A7-8V towards cooler stars to the growing efficiency of the solar-type convective dynamo. To our knowledge this is the first time that this "onset of convection" is directly seen in Ca II H&K activity, which nicely demonstrates the power of our new template method.

5. Summary

In the present paper we measured the chromospheric Ca II H&K activity from 481 stars. The observations were carried out with the FEROS and FOCES instruments and include objects from late A- to late K-type stars. From these spectra we extracted the S values according to the Mount Wilson method and calibrated them to the Mount Wilson S-index based on a subsample with given S-indices from the literature. For main-sequence stars with $B-V > 0.44$ we calculated the chromospheric emission ratio log $R'_{\rm HK}$ and find our measurements to agree with the literature data. Also, the activity distribution in our sample is in agreement with previous studies, with a slightly higher fraction of active stars possibly being caused by a bias towards higher rotational velocities in one of the FEROS and the FOCES sample.

Our analysis of the influence of the rotational broadening on the measured log $R'_{\rm HK}$ shows a minor impact for active stars and a strong impact for rapidly rotating late A to early F stars, which are supposed to be inactive or little active. This is due to the fact that in the active stars there are two effects caused by rotational broadening, the loss of emission flux in the line core and the filling of the line with flux from the broadened line wings. In active

stars both effects approximately cancel out each other, while in the absence of an emission feature in the inactive stars leaves the filling-up of the line as the remaining effect, therefore resulting in high $\log R'_{\rm HK}$ values for these inactive stars.

In order to measure the Ca II H&K activity in $\log R'_{\rm HK}$ for stars with $B-V < 0.44$, which are often rapidly rotating and relatively inactive, we developed a new method, which is based on the comparison of the target star with a slowly rotating template star. The template spectrum is artificially broadened to the rotational velocity of the star and fitted to the star's spectrum in the line wings. The difference between the template and the star in the line core represents the emission feature and can be converted into $\log R'_{\rm HK}$ values. We selected four stars as template stars, which cover a broad range in $T_{\rm eff}$ and $\log g$. With these templates, we are able to measure the activity in $\log R'_{\rm HK}$ for 238 sample stars. The fraction of stars in our sample with template measurements can be increased by finding additional template stars. Those stars without a template measurement are stars which differ significantly from our templates in $T_{\rm eff}$ and/or $\log g$. In two areas of our sample the coverage can be improved: the main-sequence stars in the range of $B-V < 0.3$ and $B-V > 0.9$. For the first group the main problem is the fact that the number of stars with v sin(i) < 10 km/s is very small. Those objects are most likely observed at high inclination angles, which limits the number of template candidates. For the second group the limiting factor is the fact that the template star must be inactive. Considering the fact that the Mount Wilson method does not suffer from the problems, which are present in the early solar-like stars when applied to the late solar-like stars, the main field of application of our template method are clearly the rapidly rotating late A- to F-type stars. For these objects our new method produces results contributing consistent measurements to existing chromospheric emission measurements. Specifically, our measurements of the chromospheric emission ratio showed, for the first time to our knowledge, the onset of the solar-type dynamo at late A- and early F-type stars in $\log R'_{\rm HK}$ values.

Table 2. Basic data and the results of the activity measurements of all 481 stars.

HD	B-V	template	v sin(i)	$T_{\rm eff}$	log g	class	$S_{\rm classic}$	$logR'_{\rm HK}$(classic)	$S_{\rm template}$	$logR'_{\rm HK}$(template)
105	0.60	1	14.5	5866	4.60	ms	0.375	-4.349	0.269	-4.371
377	0.58	1	13.9	5768	4.57	ms	0.359	-4.355	0.274	-4.344
432	0.34	2	71.0	6763	3.31	g	0.210	-	0.060	-4.841
693	0.49	-	5.1	6131	4.10	ms	0.142	-4.962	-	-
739	0.40	-	4.4	6405	4.32	ms	0.144	-	-	-
905	0.31	-	24.3	6929	4.12	ms	0.267	-	-	-
984	0.48	1	38.6	6194	4.58	ms	0.334	-4.310	0.200	-4.404
1237	0.50	1	4.5	5321	-	ms	0.390	-4.238	0.305	-4.234
1671	0.42	2	42.5	6344	3.63	g	0.240	-	0.112	-4.630
2025	0.95	-	4.1	4864	-	ms	0.388	-	-	-
3196	0.56	-	5.5	5982	4.36	ms	0.322	-4.402	-	-
3196	0.56	1	35.0	5982	4.36	ms	0.269	-4.515	0.141	-4.615
3395	0.89	-	4.2	-	-	ms	1.315	-4.026	-	-
4378	1.26	-	4.3	-	-	ms	0.751	-	-	-
4391	0.64	1	5.0	5662	4.63	ms	0.218	-4.738	0.116	-4.772
4628	0.88	-	4.4	4910	4.83	ms	0.235	-4.855	-	-
4757	0.40	-	93.8	6706	3.48	g	0.241	-	-	-
4813	0.50	1	4.3	6139	4.50	ms	0.166	-4.824	0.044	-5.073
5133	0.94	-	4.5	4943	-	ms	0.411	-	-	-
6130	0.46	-	12.6	6925	2.37	g	0.162	-	-	-
6210	0.52	-	42.0	5944	3.58	g	0.285	-	-	-
6434	0.60	1	4.3	5718	4.73	ms	0.159	-4.979	0.056	-5.055
6706	0.40	-	46.0	6551	4.11	ms	0.253	-	-	-
7661	0.74	1	5.6	5296	-	ms	0.430	-4.402	0.342	-4.408
8556	0.37	-	24.8	6565	4.34	ms	0.235	-	-	-
8723	0.34	-	60.1	6670	4.39	ms	0.277	-	-	-
8799	0.42	3	57.1	6581	4.32	ms	0.277	-	0.153	-4.483
9540	0.76	1	3.9	5323	4.93	ms	0.281	-4.661	0.199	-4.665
9919	0.31	-	103.8	6767	3.94	ms	0.306	-	-	-
10647	0.53	1	5.2	6047	4.60	ms	0.196	-4.714	0.075	-4.865
10700	0.72	1	3.5	5447	5.01	ms	0.165	-5.026	0.076	-5.039
11151	0.40	-	33.4	6526	4.13	ms	0.219	-	-	-
11257	0.27	-	12.7	6969	4.06	ms	0.280	-	-	-
11443	0.49	2	81.6	6213	3.76	g	0.306	-	0.241	-4.349
11937	0.85	1	4.5	5050	2.90	ms	0.249	-4.801	0.168	-4.850
11977	0.92	-	4.2	-	-	ms	0.104	-	-	-
12039	0.61	1	15.2	5508	-	ms	0.457	-4.247	0.357	-4.256
13174	0.32	-	164.8	6860	3.14	g	0.207	-	-	-
13445	0.77	-	3.9	5263	4.91	ms	0.260	-4.716	-	-
13480	0.78	-	35.8	-	-	ms	0.413	-4.462	-	-
13612	0.55	-	5.9	5975	4.02	ms	0.180	-4.805	-	-
13872	0.47	-	12.6	6253	4.12	ms	0.214	-4.580	-	-
14690	0.29	-	230.9	6908	3.21	g	0.270	-	-	-
15257	0.28	-	79.8	7250	3.88	ms	0.211	-	-	-
15524	0.37	2	59.8	6592	3.97	ms	0.219	-	0.109	-4.605
16157	1.36	-	15.8	-	-	ms	5.089	-	-	-
16176	0.48	-	25.6	6254	4.03	ms	0.238	-4.521	-	-
16327	0.44	-	41.9	6244	3.67	g	0.223	-	-	-
16765	0.52	-	32.0	6390	4.83	ms	0.313	-4.383	-	-
16765	0.52	3	32.0	6390	4.83	ms	0.288	-4.435	0.158	-4.534
17051	0.57	1	6.2	6109	4.58	ms	0.246	-4.585	0.143	-4.619
17094	0.38	-	45.1	7141	3.84	g	0.193	-	-	-
17163	0.28	-	109.1	7168	4.01	ms	0.219	-	-	-
17206	0.45	3	25.3	6371	4.48	ms	0.216	-4.557	0.091	-4.727
17904	0.37	-	54.2	6491	3.70	g	0.220	-	-	-
17925	0.91	-	4.9	5186	4.88	ms	0.638	-	-	-
18404	0.41	-	23.5	6658	4.37	ms	0.217	-	-	-
18907	0.83	1	4.2	5311	5.19	ms	0.137	-5.197	0.050	-5.347
19994	0.57	1	7.7	6093	4.16	ms	0.149	-5.020	0.044	-5.127
20630	0.68	1	5.7	5629	4.73	ms	0.363	-4.442	0.267	-4.451

continued

HD	B-V	template	v sin(i)	$T_{\rm eff}$	log g	class	$S_{\rm classic}$	$logR'_{\rm HK}$(classic)	$S_{\rm template}$	$logR'_{\rm HK}$(template)
20675	0.41	3	16.5	6396	4.03	ms	0.165	-	0.044	-5.018
20794	0.71	1	4.0	5543	4.78	ms	0.157	-5.067	0.070	-5.061
21411	0.71	1	4.2	5382	-	ms	0.232	-4.748	0.139	-4.764
22001	0.39	3	15.0	6714	4.21	ms	0.183	-	0.054	-4.920
22049	0.88	1	4.6	5127	4.55	ms	0.231	-4.865	0.131	-4.996
22484	0.58	-	4.2	5938	4.19	ms	0.140	-5.104	-	-
22701	0.35	3	55.0	6610	4.09	ms	0.216	-	0.086	-4.703
22879	0.49	-	4.4	5826	4.70	ms	0.156	-4.867	-	-
23249	0.92	-	4.3	4865	3.73	ms	0.122	-	-	-
23754	0.45	3	15.0	6637	4.19	ms	0.150	-4.855	0.044	-5.039
24164	0.29	-	65.7	7148	4.32	ms	0.296	-	-	-
24357	0.35	3	65.8	6895	4.11	ms	0.238	-	0.106	-4.609
25202	0.30	-	164.7	6952	3.85	ms	0.285	-	-	-
25291	0.45	-	6.2	7877	1.78	g	0.066	-	-	-
25457	0.50	3	17.3	6333	4.68	ms	0.305	-4.381	0.200	-4.418
25457	0.50	3	17.6	6333	4.68	ms	0.316	-4.359	0.201	-4.416
25570	0.34	-	34.4	6686	4.08	ms	0.240	-	-	-
25621	0.50	1	16.6	6091	3.74	g	0.171	-	0.070	-4.896
25983	0.50	3	1.1	6353	-	g	0.203	-	0.093	-4.767
25998	0.47	-	17.6	6195	4.53	ms	0.326	-4.314	-	-
26574	0.31	4	108.1	6964	3.53	g	0.177	-	0.044	-4.956
26990	0.60	1	5.0	5664	4.91	ms	0.237	-4.642	0.137	-4.664
27256	0.89	-	5.7	-	-	ms	0.108	-5.372	-	-
27459	0.23	-	78.3	7642	3.95	ms	0.176	-	-	-
27466	0.65	1	4.5	5597	-	ms	0.242	-4.671	0.145	-4.687
27749	0.28	-	10.0	7449	4.22	ms	0.373	-	-	-
27901	0.39	3	151.2	6817	4.07	ms	0.264	-	0.121	-4.569
28204	0.27	-	26.7	7361	3.77	g	0.186	-	-	-
28255	0.59	1	4.3	5698	4.52	ms	0.170	-4.901	0.070	-4.944
28271	0.50	-	33.2	6045	3.61	g	0.264	-	-	-
28294	0.34	-	86.4	7134	4.05	ms	0.232	-	-	-
28485	0.34	4	178.2	7082	3.92	ms	0.259	-	0.111	-4.585
28677	0.34	-	134.9	6981	4.03	ms	0.291	-	-	-
28704	0.36	2	88.1	6672	3.93	ms	0.224	-	0.114	-4.584
29231	0.80	1	3.4	5308	-	ms	0.242	-4.782	0.154	-4.826
29316	0.31	4	168.2	6926	3.71	g	0.228	-	0.044	-4.954
29375	0.29	-	144.9	7190	3.95	ms	0.254	-	-	-
29391	0.26	-	71.8	7259	4.13	ms	0.227	-	-	-
29875	0.30	-	47.8	7080	4.27	ms	0.231	-	-	-
29992	0.37	3	97.5	6742	4.06	ms	0.232	-	0.114	-4.588
30034	0.26	4	103.7	7484	3.99	ms	0.211	-	0.123	-4.516
30495	0.64	1	4.2	5745	4.60	ms	0.301	-4.517	0.204	-4.528
30652	0.45	-	17.2	6408	4.45	ms	0.209	-4.582	-	-
31662	0.39	3	27.7	6501	4.27	ms	0.190	-	0.071	-4.802
32147	1.06	-	4.1	6051	6.64	ms	0.282	-	-	-
32450	1.46	-	5.4	-	-	ms	1.345	-	-	-
32537	0.30	-	16.4	6970	4.07	ms	0.222	-	-	-
32743	0.39	3	21.6	6541	4.23	ms	0.172	-	0.058	-4.892
33167	0.40	2	47.5	6493	3.80	g	0.190	-	0.064	-4.853
33204	0.26	-	36.1	7530	4.06	ms	0.189	-	-	-
33262	0.47	1	14.8	6082	4.71	ms	0.272	-4.426	0.173	-4.462
33276	0.29	4	59.8	7020	3.14	g	0.132	-	0.044	-4.942
33564	0.45	3	12.7	6233	4.17	ms	0.133	-4.979	0.044	-5.041
33793	1.54	-	6.1	3524	4.87	ms	0.333	-	-	-
33959	0.20	4	27.6	7498	3.46	g	0.132	-	0.044	-4.884
34180	0.36	-	58.4	6485	3.96	ms	0.221	-	-	-
35296	0.52	1	16.0	6060	4.54	ms	0.315	-4.380	0.207	-4.418
35850	0.50	1	52.6	6036	4.70	ms	0.499	-4.106	0.422	-4.096
37147	0.22	-	109.9	7621	3.99	ms	0.213	-	-	-
37495	0.46	2	27.2	6316	3.91	g	0.205	-	0.084	-4.781

continued

HD	B-V	template	v sin(i)	$T_{\rm eff}$	log g	class	$S_{\rm classic}$	$logR'_{\rm HK}$(classic)	$S_{\rm template}$	$logR'_{\rm HK}$(template)
37572	0.83	-	8.7	5035	-	ms	0.763	-4.206	-	-
37788	0.28	-	32.3	7020	3.83	ms	0.205	-	-	-
37962	0.65	1	5.0	5610	-	ms	0.211	-4.771	0.098	-4.856
38309	0.30	-	100.5	7118	3.97	ms	0.243	-	-	-
38529	0.75	1	4.7	5452	3.34	ms	0.172	-4.997	0.088	-5.004
38858	0.64	1	4.2	5706	4.86	ms	0.165	-4.978	0.065	-5.023
38949	0.70	1	6.0	5960	4.74	ms	0.281	-4.614	0.179	-4.645
39060	0.17	-	122.0	8084	4.23	ms	0.231	-	-	-
40136	0.30	-	15.6	6943	4.11	ms	0.340	-	-	-
40292	0.31	-	38.1	7110	3.83	g	0.198	-	-	-
41074	0.31	-	87.8	6912	3.92	ms	0.229	-	-	-
42581	1.51	-	6.4	-	-	ms	1.805	-	-	-
42581	1.51	-	6.4	-	-	ms	1.672	-	-	-
43042	0.44	3	6.0	6487	4.38	ms	0.157	-4.799	0.044	-5.033
43386	0.42	3	19.4	6512	4.44	ms	0.239	-	0.098	-4.677
43587	0.61	1	5.2	5803	4.29	ms	0.151	-5.047	0.053	-5.088
43587	0.61	0	3.8	5803	4.29	ms	0.152	-5.040	0.044	-5.162
44497	0.28	4	89.4	7010	3.66	g	0.208	-	0.094	-4.609
44573	0.92	1	5.1	-	-	ms	0.395	-	0.294	-4.701
44594	0.65	1	4.4	5709	4.12	ms	0.155	-5.048	0.051	-5.136
46273	0.41	-	106.9	6674	3.82	ms	0.241	-	-	-
48189	0.57	1	15.5	5772	4.65	ms	0.404	-4.275	0.303	-4.288
48682	0.53	3	5.4	6300	4.65	ms	0.142	-5.016	0.044	-5.094
48737	0.39	2	66.1	6496	3.90	g	0.209	-	0.091	-4.697
50018	0.35	-	148.9	6705	3.31	g	0.192	-	-	-
50277	0.24	-	268.9	7309	3.65	g	0.333	-	-	-
50281	1.07	-	3.9	5896	6.57	ms	0.652	-	-	-
50635	0.28	-	152.6	7134	3.98	ms	0.285	-	-	-
51199	0.33	-	91.7	6730	3.80	ms	0.226	-	-	-
51733	0.36	-	102.3	6729	3.97	ms	0.245	-	-	-
52698	0.90	1	4.2	-	-	ms	0.422	-	0.322	-4.633
52711	0.60	1	5.4	5780	4.41	ms	0.148	-5.057	0.049	-5.110
53143	0.80	1	4.1	5223	-	ms	0.392	-4.507	0.296	-4.541
55052	0.36	2	81.8	6668	3.19	g	0.173	-	0.044	-4.986
55057	0.28	4	139.9	7167	3.49	g	0.180	-	0.044	-4.933
56963	0.31	-	77.8	6893	4.09	ms	0.249	-	-	-
56986	0.34	-	129.7	6837	3.72	g	0.256	-	-	-
57006	0.49	1	5.8	6071	3.75	g	0.120	-	0.044	-5.087
57927	0.33	-	89.5	6772	3.47	g	0.190	-	-	-
58579	0.30	4	147.1	7053	3.49	g	0.218	-	0.044	-4.944
58855	0.41	3	8.5	6378	4.58	ms	0.151	-	0.044	-5.019
58946	0.31	-	59.0	6892	4.08	ms	0.249	-	-	-
58954	0.29	-	199.1	7030	3.42	g	0.236	-	-	-
59967	0.60	1	3.4	5662	-	ms	0.324	-4.440	0.234	-4.434
60111	0.30	-	117.6	7181	3.99	ms	0.212	-	-	-
61005	0.71	1	8.2	5345	-	ms	0.471	-4.324	0.386	-4.322
61035	0.30	-	124.3	6986	4.20	ms	0.269	-	-	-
61110	0.40	2	91.1	6575	3.56	g	0.200	-	0.066	-4.842
61421	0.40	-	3.9	6528	4.01	ms	0.158	-	-	-
61606	0.95	-	5.6	4624	4.74	ms	0.580	-	-	-
62952	0.30	-	127.5	6933	3.55	g	0.232	-	-	-
64235	0.37	-	42.6	6748	4.40	ms	0.239	-	-	-
64379	0.44	3	42.6	6399	4.58	ms	0.241	-	0.114	-4.621
64379	0.44	3	42.6	6399	4.58	ms	0.241	-	0.108	-4.646
64685	0.41	-	47.6	6838	4.22	ms	0.210	-	-	-
65301	0.37	-	11.7	6586	4.23	ms	0.227	-	-	-
65925	0.35	-	71.6	6515	3.48	g	0.205	-	-	-
67228	0.60	1	5.5	5837	4.03	ms	0.135	-5.179	0.044	-5.157
67483	0.42	2	52.4	6209	3.67	g	0.239	-	0.111	-4.635
67767	0.81	1	5.6	-	-	ms	0.164	-5.053	0.079	-5.129

continued

HD	B-V	template	v sin(i)	$T_{\rm eff}$	log g	class	$S_{\rm classic}$	$logR'_{\rm HK}$(classic)	$S_{\rm template}$	$logR'_{\rm HK}$(template)
68456	0.43	-	9.4	6353	4.20	ms	0.226	-	-	-
69548	0.37	3	53.9	6705	4.48	ms	0.216	-	0.099	-4.646
69830	0.79	1	4.5	5520	5.09	ms	0.156	-5.091	0.070	-5.157
70958	0.47	3	45.5	6230	4.30	ms	0.258	-4.459	0.135	-4.569
72041	0.29	4	109.2	6969	3.51	g	0.201	-	0.074	-4.717
72617	0.29	-	74.5	6857	3.61	g	0.202	-	-	-
72673	0.79	1	4.6	5341	4.94	ms	0.183	-4.965	0.099	-5.006
72943	0.18	-	56.8	6897	3.66	ms	0.195	-	-	-
72945	0.51	1	5.7	6174	4.37	ms	0.131	-5.087	0.044	-5.080
73667	0.83	-	4.4	5090	4.86	ms	0.166	-5.048	-	-
73668	0.59	1	4.1	5794	-	ms	0.171	-4.896	0.069	-4.950
73752	0.73	1	4.6	5508	-	ms	0.139	-5.202	0.045	-5.278
74228	0.38	-	5.3	6955	3.04	g	0.323	-	-	-
74576	0.93	-	5.1	4920	-	ms	0.700	-	-	-
75302	0.70	1	3.8	5520	-	ms	0.260	-4.659	0.161	-4.685
75393	0.48	1	26.5	6109	-	ms	0.327	-4.321	0.209	-4.385
75486	0.27	4	128.1	6993	3.32	g	0.213	-	0.051	-4.866
76143	0.38	2	83.0	6579	3.59	g	0.212	-	0.096	-4.664
77093	0.28	-	195.4	7091	3.86	ms	0.306	-	-	-
77370	0.42	3	60.4	6609	4.21	ms	0.226	-	0.114	-4.613
79028	0.51	1	6.1	5837	4.12	ms	0.142	-4.995	0.049	-5.039
79940	0.42	2	117.2	6397	3.25	g	0.213	-	0.063	-4.878
80586	0.92	1	6.0	-	-	g	0.205	-	0.132	-5.014
80671	0.37	3	26.2	6571	4.31	ms	0.174	-	0.048	-4.962
81797	1.48	-	5.6	4252	1.81	ms	0.175	-	-	-
81858	0.60	1	5.1	5772	3.91	ms	0.141	-5.113	0.049	-5.108
81937	0.31	4	155.3	7009	3.73	g	0.226	-	0.066	-4.782
81997	0.46	3	29.8	6471	4.32	ms	0.196	-4.638	0.078	-4.799
82106	1.00	-	4.1	4419	4.72	ms	0.696	-	-	-
82189	0.48	1	7.6	6168	3.82	g	0.186	-	0.096	-4.735
82434	0.32	-	156.0	6826	4.01	ms	0.277	-	-	-
82554	0.45	-	129.7	6272	3.37	g	0.243	-	-	-
83287	0.21	-	102.6	7815	4.21	ms	0.197	-	-	-
83962	0.36	-	140.3	6507	3.56	g	0.237	-	-	-
84117	0.53	1	5.2	6084	4.35	ms	0.153	-4.940	0.044	-5.095
84607	0.32	4	93.1	7000	3.57	g	0.168	-	0.044	-4.959
84999	0.29	4	124.2	7002	3.45	g	0.195	-	0.044	-4.941
85512	0.90	-	4.1	-	-	ms	0.405	-4.589	-	-
86146	0.43	3	5.0	6401	4.21	ms	0.162	-	0.048	-4.988
87500	0.34	4	189.4	6923	3.60	g	0.235	-	0.044	-4.972
88201	0.56	1	10.1	6054	4.59	ms	0.301	-4.443	0.198	-4.469
88742	0.62	1	4.3	5860	4.46	ms	0.167	-4.950	0.068	-4.985
88742	0.62	1	4.3	5860	4.46	ms	0.210	-4.751	0.103	-4.806
89125	0.52	1	5.8	6087	4.41	ms	0.146	-4.972	0.044	-5.087
89254	0.30	4	63.5	7173	3.71	ms	0.161	-	0.061	-4.832
89449	0.44	-	14.7	6398	4.19	ms	0.177	-	-	-
89744	0.49	1	8.8	6178	4.08	ms	0.126	-5.112	0.044	-5.066
90589	0.33	3	51.6	6794	4.19	ms	0.207	-	0.085	-4.696
90589	0.33	3	51.6	6794	4.19	ms	0.214	-	0.090	-4.674
90712	0.54	1	10.5	5913	4.68	ms	0.318	-4.391	0.219	-4.409
90712	0.54	1	10.5	5913	4.68	ms	0.323	-4.383	0.223	-4.400
90839	0.49	1	5.5	6081	4.69	ms	0.175	-4.761	0.071	-4.857
91962	0.62	1	6.1	5818	4.85	ms	0.303	-4.494	0.203	-4.510
92168	0.57	-	14.1	5844	3.41	g	0.120	-	-	-
92588	0.87	-	1.0	-	-	ms	0.099	-5.472	-	-
92787	0.31	-	58.2	6904	3.85	ms	0.216	-	-	-
92788	0.50	1	4.5	5559	-	ms	0.154	-4.892	0.056	-4.969
93372	0.45	3	10.6	6405	4.53	ms	0.186	-4.675	0.068	-4.856
95542	0.55	1	1.1	5942	-	ms	0.184	-4.786	0.088	-4.814
96064	0.77	1	5.6	-	-	ms	0.514	-4.337	0.428	-4.344

continued

HD	B-V	template	v sin(i)	$T_{\rm eff}$	log g	class	$S_{\rm classic}$	$logR'_{\rm HK}$(classic)	$S_{\rm template}$	$logR'_{\rm HK}$(template)
96202	0.36	-	93.4	6747	3.92	g	0.234	-	-	-
96220	0.27	-	223.2	7159	3.80	ms	0.333	-	-	-
98712	1.36	-	4.2	-	-	ms	2.457	-	-	-
98991	0.42	-	17.0	6463	3.92	g	0.212	-	-	-
99285	0.34	-	34.4	6568	3.79	g	0.233	-	-	-
99329	0.31	-	137.9	6990	3.98	ms	0.253	-	-	-
99564	0.44	-	38.8	6255	3.68	g	0.200	-	-	-
99565	1.36	1	4.1	-	-	ms	0.237	-	0.136	-5.746
100203	0.50	1	6.1	6040	4.21	ms	0.145	-4.957	0.044	-5.073
100563	0.53	3	12.7	6489	4.48	ms	0.178	-4.795	0.066	-4.925
100623	0.81	1	4.0	5128	-	ms	0.188	-4.954	0.113	-4.970
100623	0.81	1	4.0	5128	-	ms	0.191	-4.944	0.111	-4.981
101107	0.31	-	93.9	6983	4.24	ms	0.253	-	-	-
101581	1.07	-	5.0	-	-	ms	0.512	-	-	-
102365	0.68	1	0.5	5624	4.88	ms	0.160	-5.031	0.063	-5.075
102590	0.26	-	74.0	7376	4.13	ms	0.230	-	-	-
102870	0.55	1	4.3	6065	4.15	ms	0.148	-4.997	0.044	-5.111
103313	0.20	4	67.4	7718	3.66	g	0.153	-	0.044	-4.883
103313	0.20	4	66.6	7718	3.66	g	0.140	-	0.051	-4.818
103928	0.29	-	79.0	7047	4.25	ms	0.239	-	-	-
103932	1.16	-	4.4	-	-	ms	0.552	-	-	-
104304	0.78	1	4.5	5366	4.57	ms	0.162	-5.058	0.067	-5.162
104731	0.41	3	11.0	6572	4.26	ms	0.157	-	0.044	-5.018
104827	0.22	4	44.3	7535	3.81	ms	0.133	-	0.044	-4.954
105452	0.34	-	25.0	7161	4.16	ms	0.214	-	-	-
106022	0.37	2	77.2	6651	3.90	g	0.214	-	0.102	-4.638
106112	0.31	-	64.1	7122	3.98	ms	0.285	-	-	-
107054	0.28	-	167.7	6866	3.62	g	0.277	-	-	-
107192	0.30	-	68.1	7010	4.24	ms	0.234	-	-	-
107326	0.35	4	132.3	7107	3.79	g	0.227	-	0.103	-4.613
107904	0.33	-	111.3	6726	3.10	g	0.148	-	-	-
108722	0.40	-	97.0	6490	3.63	g	0.230	-	-	-
108799	0.56	1	7.0	5844	4.60	ms	0.315	-4.416	0.218	-4.427
109141	0.34	-	135.8	6881	4.12	ms	0.259	-	-	-
109799	0.31	-	34.0	6943	4.04	ms	0.216	-	-	-
109931	0.27	-	227.8	7016	3.50	g	0.307	-	-	-
110317	0.42	2	6.2	6547	3.61	g	0.180	-	0.064	-4.872
110379	0.36	-	27.0	6934	4.32	ms	0.244	-	-	-
110379	0.36	-	25.5	6934	4.32	ms	0.256	-	-	-
110385	0.39	-	105.3	6717	3.64	g	0.222	-	-	-
110646	0.84	-	5.7	5158	4.03	ms	0.121	-5.301	-	-
110834	0.42	-	133.3	6244	3.22	g	0.241	-	-	-
111170	0.77	-	0.0	4977	-	ms	0.686	-4.193	-	-
111456	0.43	-	42.2	6313	4.70	ms	0.368	-	-	-
112429	0.27	-	119.6	7126	4.15	ms	0.268	-	-	-
113415	0.52	1	5.8	6119	4.35	ms	0.163	-4.862	0.064	-4.926
113848	0.36	3	26.0	6581	4.13	ms	0.198	-	0.066	-4.820
114378	0.45	3	19.6	6324	4.53	ms	0.236	-4.497	0.121	-4.603
114435	0.47	2	80.1	6370	3.40	g	0.222	-	0.124	-4.626
114642	0.46	2	11.8	6255	3.96	g	0.159	-	0.046	-5.048
114837	0.48	3	8.8	6253	4.33	ms	0.138	-4.979	0.044	-5.059
115383	0.59	1	4.5	5986	4.25	ms	0.289	-4.497	0.195	-4.502
115617	0.71	1	0.4	5509	4.51	ms	0.151	-5.103	0.060	-5.133
115810	0.24	-	99.2	7185	3.76	ms	0.233	-	-	-
116568	0.37	3	37.0	6485	4.29	ms	0.207	-	0.080	-4.743
117176	0.69	1	5.0	5459	4.01	ms	0.136	-5.224	0.044	-5.241
117360	0.37	3	4.0	6301	4.46	ms	0.137	-	0.044	-4.997
117361	0.36	-	70.1	6701	3.78	g	0.223	-	-	-
117436	0.29	-	163.1	7003	3.82	ms	0.252	-	-	-
117524	0.69	1	30.0	-	-	ms	0.741	-4.074	0.653	-4.072

continued

HD	B-V	template	v sin(i)	$T_{\rm eff}$	log g	class	$S_{\rm classic}$	$logR'_{\rm HK}$(classic)	$S_{\rm template}$	$logR'_{\rm HK}$(template)
118889	0.30	-	140.6	6951	3.91	ms	0.248	-	-	-
119269	0.66	1	22.5	-	-	ms	0.679	-4.088	0.610	-4.072
119288	0.42	3	20.0	6546	4.10	ms	0.174	-	0.048	-4.986
119756	0.38	3	63.9	6809	4.24	ms	0.236	-	0.125	-4.550
120136	0.48	-	14.9	6437	4.36	ms	0.189	-4.688	-	-
120467	1.28	-	4.7	4197	5.57	ms	0.588	-	-	-
120987	0.39	3	8.5	6413	4.16	g	0.180	-	0.061	-4.870
121370	0.58	1	11.8	6024	3.75	g	0.125	-	0.044	-5.158
121504	0.70	1	5.3	5834	-	ms	0.185	-4.916	0.087	-4.959
121932	0.32	2	155.4	6890	3.60	g	0.222	-	0.062	-4.819
122066	0.48	2	41.1	6395	3.81	g	0.185	-	0.060	-4.945
122106	0.45	3	16.0	6338	4.03	g	0.161	-	0.047	-5.029
122430	1.35	-	4.7	-	-	ms	0.130	-	-	-
122797	0.35	3	33.6	6587	4.18	g	0.189	-	0.064	-4.823
123255	0.32	4	157.9	6918	3.63	g	0.220	-	0.071	-4.758
123999	0.49	1	17.0	6118	4.02	ms	0.125	-5.127	0.044	-5.068
124115	0.45	3	28.3	6367	-	ms	0.181	-4.686	0.063	-4.887
124425	0.48	2	23.5	6334	3.97	g	0.197	-	0.074	-4.857
124780	0.27	-	70.7	7204	3.87	ms	0.206	-	-	-
124850	0.50	1	15.5	6075	3.92	ms	0.199	-4.671	0.091	-4.760
124850	0.50	1	15.0	6139	3.98	ms	0.187	-4.719	0.069	-4.878
125072	1.03	-	4.4	5015	4.50	ms	0.323	-	-	-
125442	0.28	-	148.0	7149	3.77	g	0.208	-	-	-
125451	0.36	3	40.5	6615	4.31	ms	0.220	-	0.091	-4.683
126660	0.45	3	29.2	6321	4.36	ms	0.309	-4.330	0.183	-4.424
127486	0.48	2	24.5	6395	3.95	g	0.180	-	0.066	-4.906
127739	0.35	-	55.8	6787	3.85	g	0.204	-	-	-
127821	0.39	3	55.6	6601	4.59	ms	0.240	-	0.138	-4.511
128167	0.36	-	7.7	6649	4.37	ms	0.228	-	-	-
128620	0.71	1	4.5	5627	4.17	ms	0.140	-5.185	0.044	-5.262
128621	0.88	1	4.9	5283	4.62	ms	0.196	-4.962	0.114	-5.056
129153	0.22	-	105.7	7693	4.16	ms	0.220	-	-	-
129502	0.36	-	47.0	6695	4.20	ms	0.219	-	-	-
129926	0.35	1	112.5	6048	4.61	ms	0.203	-	0.072	-4.778
129926	0.35	1	112.5	6048	4.61	ms	0.214	-	0.078	-4.742
130945	0.43	-	9.8	6443	4.11	ms	0.201	-	-	-
131976	1.58	-	4.1	4732	5.27	ms	0.463	-	-	-
131977	1.11	-	3.9	4661	5.28	ms	0.485	-	-	-
132052	0.29	-	113.3	6964	3.82	ms	0.240	-	-	-
132254	0.53	3	7.7	6348	4.43	ms	0.137	-5.065	0.044	-5.095
132772	0.30	-	72.5	6835	3.64	g	0.203	-	-	-
133002	0.68	1	5.2	5461	3.86	ms	0.195	-4.859	0.136	-4.744
134083	0.43	3	44.4	6528	4.41	ms	0.200	-	0.076	-4.796
136352	0.65	1	4.3	5675	4.63	ms	0.164	-4.990	0.060	-5.069
136407	0.34	-	91.5	6675	3.89	ms	0.262	-	-	-
136751	0.33	-	72.7	6810	3.89	ms	0.212	-	-	-
137628	1.00	-	5.3	-	-	ms	0.332	-	-	-
139084	0.83	1	16.3	4965	-	ms	0.758	-4.209	0.698	-4.206
139225	0.31	-	104.4	6960	3.92	ms	0.234	-	-	-
139498	0.73	-	0.0	-	-	ms	0.693	-4.146	-	-
139664	0.40	3	71.6	6681	4.49	ms	0.234	-	0.117	-4.591
139798	0.32	-	64.8	6733	4.09	ms	0.238	-	-	-
139798	0.32	-	64.8	6733	4.09	ms	0.242	-	-	-
140374	0.72	-	0.0	5140	-	ms	0.471	-4.335	-	-
140538	0.65	1	5.1	5557	4.34	ms	0.180	-4.901	0.088	-4.897
140538	0.65	1	4.1	5557	-	ms	0.177	-4.915	0.084	-4.916
141004	0.60	1	5.0	5831	4.22	ms	0.149	-5.048	0.051	-5.092
141521	0.71	-	8.2	5199	-	ms	0.616	-4.186	-	-
142229	0.58	1	5.0	5714	-	ms	0.299	-4.466	0.206	-4.468
142709	1.12	-	5.3	-	-	ms	0.414	-	-	-

continued

HD	B-V	template	v sin(i)	$T_{\rm eff}$	log g	class	$S_{\rm classic}$	$logR'_{\rm HK}$(classic)	$S_{\rm template}$	$logR'_{\rm HK}$(template)
142860	0.48	1	10.0	6146	4.07	ms	0.142	-4.951	0.044	-5.059
143466	0.26	-	141.3	7235	3.88	ms	0.244	-	-	-
143790	0.43	2	5.5	6270	3.93	g	0.156	-	0.044	-5.036
143928	0.36	3	23.7	6606	4.18	ms	0.179	-	0.055	-4.895
144069	0.53	-	11.6	-	-	ms	0.179	-4.790	-	-
144284	0.52	-	28.5	6184	4.04	ms	0.271	-4.472	-	-
144628	0.86	-	5.0	5093	-	ms	0.197	-4.948	-	-
145417	0.82	1	4.6	5986	5.64	ms	0.179	-4.993	0.104	-5.020
146514	0.29	-	152.9	7031	4.00	ms	0.292	-	-	-
146836	0.42	3	18.8	6355	4.00	g	0.202	-	0.083	-4.758
147365	0.37	3	72.5	6657	4.44	ms	0.252	-	0.158	-4.444
147449	0.32	-	76.4	6973	4.03	ms	0.229	-	-	-
147449	0.32	-	77.1	6973	4.03	ms	0.226	-	-	-
147513	0.60	1	3.9	5974	4.91	ms	0.305	-4.470	0.213	-4.468
147787	0.36	-	12.9	6992	4.25	g	0.199	-	-	-
148048	0.37	-	84.8	6731	3.97	ms	0.230	-	-	-
150557	0.30	4	61.8	6959	3.70	g	0.194	-	0.091	-4.634
150689	1.02	-	4.8	4698	-	ms	0.643	-	-	-
151613	0.34	-	47.5	6630	4.13	ms	0.216	-	-	-
151798	0.57	1	10.4	5785	4.80	ms	0.385	-4.307	0.288	-4.315
152303	0.40	3	23.5	6426	4.28	ms	0.221	-	0.095	-4.680
152751	0.57	-	2.7	5789	4.80	ms	0.544	-4.119	-	-
153221	0.90	-	4.4	-	-	ms	0.138	-	-	-
153458	0.61	1	0.0	5648	4.29	ms	0.218	-4.713	0.141	-4.658
153580	0.44	3	45.4	6516	4.31	ms	0.204	-4.592	0.086	-4.747
154363	1.16	-	3.8	4530	5.28	ms	0.527	-	-	-
154417	0.58	1	5.3	5888	4.55	ms	0.279	-4.510	0.171	-4.549
155103	0.31	-	57.9	7150	3.99	ms	0.281	-	-	-
155154	0.27	-	188.9	7077	3.98	ms	0.326	-	-	-
155885	0.77	-	3.7	5127	4.60	ms	0.361	-4.525	-	-
156026	1.16	-	4.4	4448	4.70	ms	0.813	-	-	-
156098	0.46	2	5.8	6273	3.73	g	0.156	-	0.044	-5.061
156274	0.81	1	4.5	5268	4.91	ms	0.159	-5.075	0.076	-5.143
156295	0.19	-	107.4	7818	4.16	ms	0.241	-	-	-
157728	0.20	-	73.0	7678	4.16	ms	0.202	-	-	-
159877	0.37	-	23.4	7515	2.74	g	0.152	-	-	-
160346	0.96	-	4.1	4713	4.81	ms	0.249	-	-	-
160910	0.35	-	31.7	6615	4.07	ms	0.232	-	-	-
160922	0.43	3	5.9	6506	4.33	ms	0.191	-	0.071	-4.825
161296	1.00	-	4.6	-	-	ms	0.582	-	-	-
162917	0.40	-	28.4	6498	4.31	ms	0.215	-	-	-
163151	0.42	-	115.2	6316	3.70	g	0.281	-	-	-
163929	0.29	-	105.2	7206	3.89	ms	0.221	-	-	-
165341	0.86	1	4.6	5333	5.50	ms	0.320	-4.671	0.225	-4.736
165373	0.28	-	79.9	6976	3.78	ms	0.220	-	-	-
166233	0.34	-	93.7	7002	4.08	ms	0.282	-	-	-
166348	1.31	-	4.8	-	-	ms	1.186	-	-	-
170657	0.84	-	4.5	-	-	ms	0.323	-4.648	-	-
171834	0.34	3	71.3	6622	4.00	ms	0.221	-	0.106	-4.603
172051	0.63	1	4.0	5647	5.38	ms	0.162	-4.992	0.066	-5.007
172748	0.33	4	25.3	7073	3.61	g	0.135	-	0.044	-4.968
173417	0.32	-	53.8	6780	3.67	g	0.202	-	-	-
173667	0.45	3	15.1	6363	4.06	ms	0.174	-4.720	0.053	-4.965
175317	0.40	-	15.9	6563	4.26	ms	0.204	-	-	-
175813	0.36	-	148.5	6659	3.77	ms	0.294	-	-	-
175824	0.41	-	53.7	6232	3.51	g	0.201	-	-	-
176303	0.50	-	23.6	5959	3.70	g	0.187	-	-	-
178449	0.32	-	135.7	6733	3.57	g	0.291	-	-	-
178596	0.32	-	57.0	6935	3.98	ms	0.268	-	-	-
179949	0.50	1	6.4	6162	4.46	ms	0.193	-4.698	0.082	-4.809

continued

HD	B-V	template	v sin(i)	$T_{\rm eff}$	log g	class	$S_{\rm classic}$	$logR'_{\rm HK}$(classic)	$S_{\rm template}$	$logR'_{\rm HK}$(template)
180777	0.28	-	56.1	7170	4.30	ms	0.280	-	-	-
180868	0.17	4	83.0	7756	3.37	g	0.154	-	0.055	-4.780
182640	0.28	-	87.3	7016	3.87	ms	0.218	-	-	-
182900	0.43	-	28.0	6396	3.82	g	0.228	-	-	-
183216	0.60	1	6.0	6012	3.02	ms	0.259	-4.579	0.153	-4.616
185124	0.39	3	87.0	6680	4.22	ms	0.217	-	0.097	-4.666
186005	0.30	4	149.9	6988	3.53	g	0.210	-	0.045	-4.936
186155	0.38	-	43.6	6819	3.65	g	0.204	-	-	-
187532	0.38	3	77.5	6788	4.33	ms	0.216	-	0.096	-4.666
187642	0.22	-	203.0	7718	4.01	ms	0.378	-	-	-
187897	0.60	1	5.5	5701	-	ms	0.229	-4.661	0.129	-4.688
188088	1.02	-	0.0	-	-	ms	0.528	-	-	-
188512	0.86	1	2.3	5100	4.37	ms	0.134	-5.212	0.044	-5.441
189245	0.49	3	72.6	6259	4.59	ms	0.339	-4.309	0.289	-4.252
190004	0.34	-	136.2	6974	3.90	ms	0.250	-	-	-
190248	0.76	1	3.8	5473	4.05	ms	0.148	-5.136	0.044	-5.318
191089	0.40	2	37.7	6473	3.53	ms	0.247	-	0.113	-4.603
191329	0.12	-	243.5	7695	3.20	g	0.471	-	-	-
192455	0.48	-	15.1	6137	3.95	g	0.262	-	-	-
192514	0.09	-	187.5	7722	2.84	g	0.352	-	-	-
192985	0.39	3	9.2	6566	4.28	ms	0.170	-	0.044	-5.007
193017	0.52	1	5.4	6090	4.70	ms	0.220	-4.614	0.101	-4.728
194943	0.33	-	87.7	6763	3.86	g	0.245	-	-	-
195068	0.30	-	40.2	7198	4.26	ms	0.230	-	-	-
196524	0.41	-	39.8	6395	3.51	g	0.253	-	-	-
196761	0.72	1	4.2	5382	-	ms	0.174	-4.975	0.081	-5.011
197461	0.27	-	14.4	7010	3.39	g	0.202	-	-	-
197692	0.39	3	41.0	6622	4.37	ms	0.224	-	0.091	-4.694
198743	0.31	-	53.7	7181	3.99	ms	0.301	-	-	-
199143	0.48	3	125.0	6311	4.66	ms	0.435	-4.162	0.586	-3.937
199611	0.30	-	133.9	6984	3.85	ms	0.290	-	-	-
199766	0.46	-	41.4	6361	4.04	ms	0.261	-4.442	-	-
201636	0.35	-	58.8	6700	3.86	g	0.259	-	-	-
202444	0.39	-	90.4	6612	3.80	g	0.270	-	-	-
203803	0.30	-	135.3	7186	3.97	ms	0.258	-	-	-
204153	0.32	-	108.8	6978	4.14	ms	0.296	-	-	-
205289	0.37	-	57.5	6525	4.31	ms	0.242	-	-	-
205852	0.29	-	181.0	6946	3.19	g	0.240	-	-	-
206043	0.28	-	134.1	7092	4.01	ms	0.303	-	-	-
206088	0.32	-	40.0	7396	3.92	g	0.184	-	-	-
206901	0.39	-	42.3	6493	3.95	g	0.233	-	-	-
207652	0.36	3	151.3	6696	4.15	ms	0.339	-	0.281	-4.187
207958	0.37	-	69.3	6747	4.21	ms	0.353	-	-	-
207978	0.39	3	7.2	6270	4.25	ms	0.170	-	0.044	-5.004
209369	0.41	-	26.4	6238	3.87	ms	0.261	-	-	-
213051	0.50	-	48.4	-	-	ms	0.246	-4.516	-	-
213845	0.44	-	34.9	6551	4.37	ms	0.228	-4.512	-	-
215664	0.32	-	201.0	6878	3.65	g	0.303	-	-	-
216756	0.36	3	11.3	6555	4.08	ms	0.220	-	0.079	-4.741
218470	0.44	3	9.7	6575	4.28	ms	0.191	-4.635	0.064	-4.872
218753	0.28	-	5.3	7383	1.76	g	0.119	-	-	-
218804	0.38	3	19.3	6258	4.14	ms	0.244	-	0.096	-4.667
219080	0.28	-	61.8	7108	3.95	ms	0.251	-	-	-
220657	0.61	-	73.4	5801	3.44	g	0.313	-	-	-
221275	0.80	1	4.2	5272	-	ms	0.261	-4.736	0.163	-4.800
221950	0.39	3	8.6	6324	4.41	ms	0.189	-	0.063	-4.857
223460	0.79	1	22.5	-	-	ms	0.495	-4.376	0.424	-4.373
224533	0.92	-	4.4	4960	3.19	ms	0.101	-	-	-
224617	0.37	-	40.3	6434	3.47	g	0.239	-	-	-

continued

HD	B-V	template	v sin(i)	$T_{\rm eff}$	log g	class	$S_{\rm classic}$	$logR'_{\rm HK}$(classic)	$S_{\rm template}$	$logR'_{\rm HK}$(template)
225213	1.46	-	4.8	-	-	ms	0.389	-	-	-

References

Allen, C. W. 1976, Astrophysical Quantities (Astrophysical Quantities, London: Athlone (3rd edition), 1976)
Baliunas, S. L., Donahue, R. A., Soon, W., & Henry, G. W. 1998, in Astronomical Society of the Pacific Conference Series, Vol. 154, Cool Stars, Stellar Systems, and the Sun, ed. R. A. Donahue & J. A. Bookbinder, 153–+
Baliunas, S. L., Donahue, R. A., Soon, W. H., et al. 1995, ApJ, 438, 269
Cincunegui, C., Díaz, R. F., & Mauas, P. J. D. 2007, A&A, 469, 309
Duncan, D. K., Vaughan, A. H., Wilson, O. C., et al. 1991, ApJS, 76, 383
Glebocki, R. & Stawikowski, A. 2000, Acta Astronomica, 50, 509
Gray, R. O., Corbally, C. J., Garrison, R. F., et al. 2006, AJ, 132, 161
Gray, R. O., Corbally, C. J., Garrison, R. F., McFadden, M. T., & Robinson, P. E. 2003, AJ, 126, 2048
Hall, J. C., Lockwood, G. W., & Skiff, B. A. 2007, AJ, 133, 862
Hartmann, L., Soderblom, D. R., Noyes, R. W., Burnham, N., & Vaughan, A. H. 1984, ApJ, 276, 254
Hauschildt, P. H. & Baron, E. 1999, Journal of Computational and Applied Mathematics, 109, 41
Henry, T. J., Soderblom, D. R., Donahue, R. A., & Baliunas, S. L. 1996, AJ, 111, 439
Kaisler, D., Zuckerman, B., Song, I., et al. 2004, A&A, 414, 175
Kaufer, A., Stahl, O., Tubbesing, S., et al. 1999, The Messenger, 95, 8
Middelkoop, F. 1982, A&A, 107, 31
Moon, T. T. & Dworetsky, M. M. 1985, MNRAS, 217, 305
Napiwotzki, R., Schönberner, D., & Wenske, V. 1992, in Lecture Notes in Physics, Berlin Springer Verlag, Vol. 401, The Atmospheres of Early-Type Stars, ed. U. Heber & C. S. Jeffery, 18–20
Nordström, B., Mayor, M., Andersen, J., et al. 2004, A&A, 418, 989
Noyes, R. W. 1984, Advances in Space Research, 4, 151
Reiners, A. & Schmitt, J. H. M. M. 2002, A&A, 384, 155
Reiners, A. & Schmitt, J. H. M. M. 2003a, A&A, 412, 813
Reiners, A. & Schmitt, J. H. M. M. 2003b, A&A, 398, 647
Relyea, L. J. & Kurucz, R. L. 1978, ApJS, 37, 45
Rutten, R. G. M. 1984, A&A, 130, 353
Schmidt, E. G. & Taylor, D. J. 1979, AJ, 84, 1193
Schmitt, J. H. M. M., Golub, L., Harnden, Jr., F. R., et al. 1985, ApJ, 290, 307
Schröder, C. & Schmitt, J. H. M. M. 2007, A&A, 475, 677
Vaughan, A. H., Preston, G. W., & Wilson, O. C. 1978, PASP, 90, 267
Wilson, O. C. 1978, ApJ, 226, 379
Wright, J. T., Marcy, G. W., Butler, R. P., & Vogt, S. S. 2004, ApJS, 152, 261

Chapter 5

Summary and outlook

5.1 Summary

In this thesis activity phenomena of A-type stars and solar-like stars have been studied. For the A-type stars, which ought to be devoid of X-ray emission, a list of stars with a nearby X-ray source was compiled. Follow-up observations with the objective of searching for magnetic fields have been carried out for 13 stars on this list. For the solar-like stars, a new method to measure the chromospheric activity in rapidly rotating stars has been developed and was tested in comparison to the classical Mount Wilson method.

X-ray activity in A-type stars

The correlation between the 1966 A-type stars listed in the Bright Star Catalogue (Hoffleit & Warren 1995) and the X-ray sources from the ROSAT catalogs yielded in 312 A-type stars which can be associated with X-ray sources.

To check the companion hypothesis, various parameters have been searched for signatures of late-type companions. Indicators of an unknown companion are the variability of radial velocity and proper motion, flare-like variations in the X-ray light curve and differences in the X-ray luminosity between two or more observations for those stars which have been observed in more than one observation mode. This search led to the conclusion that out of these 312 objects, 84 are bona fide single or resolved binary stars.

The X-ray detection rate over the whole sample is about 10-15%, with a steep increase of the detection rate beginning at spectral types A7-9V. For a complete sample of 220 A-type stars up to a distance of 50 pc, the detection rate is about 37%. This is still in agreement with the assumed binary frequency of A-type stars. With respect to the peculiar or metallic-lined A stars, there is no difference in the X-ray detection rates of these spectral subgroups. The absence of an increase of the detection rate for individual spectral subgroups supports the companion hypothesis.

Magnetic fields in A-type stars

Observations of 13 A-type stars associated with X-ray sources were carried out with the FORS1 instrument at the VLT Kuyen. These stars were selected from the list of X-ray emitting A-type stars presented in Chapter 2. In these observations, the longitudinal magnetic field was measured in two ways: first, only in the hydrogen lines and second in all metall lines. Within the error bars, the measurements for both line samples are in agreement.

For three of these stars, HD 147084, HD 148898 and HD 159312, the measurements of the weak magnetic fields are at a significance level of about 3 σ. Two additional stars, HD 174240 and HD 224392, are detected at a significance level $\geq 2\sigma$. The strength of the measured fields is about 100-200 G. In another seven stars, the measurements are below the 2 σ level or only weak signs of possible magnetic fields can be seen in individual lines. These stars are promissing candidates for further observations.

Based on the theoretical framework presented by Babel & Montmerle (1997), the predictions of the magnetically confined wind-shock model were tested for the stars with 3 σ detections of the magnetic fields. Values for the wind velocity and the mass-loss rate were estimated based on the observations of Babel & Montmerle (1997) and Czesla & Schmitt (2007). The predicted X-ray luminosities are within the same order of magnitude as the observed values, but a correlation between the X-ray luminosity and the strength of the magnetic field could not be measured.

Ca II H&K measurements in rapidly rotating stars

In order to be able to follow the chromospheric activity in the late A- and early F-type stars, a new method to measure the activity in rapidly rotating stars was developed. The chromospheric activity measurements are based on spectra obtained with the FEROS and the FOCES instrument. For 481 solar-like stars with spectral types ranging from late A to late K the activity has been determined with the Mount Wilson method and the new template method. For all of these stars the dimensionless S index has been calculated and, where determined, the chromospheric emission ratio log $R'_{\rm HK}$. The template method could be applied to 238 stars in the color range from $0.2 < B-V > 1.4$, including giant stars.

To study the rotational effect on the measured activity for different rotational velocities, the log $R'_{\rm HK}$ values of an artificially broadened stars with given v sin(i) values have been determined. For rapidly rotating active stars, the effect is small. In these objects, the loss of emission flux is compensated by the filling of the line core with flux from the broadened line wings. For the inactive stars, the absence of an emission leads to an increase of the measured flux due to the broadened line wings.

The activity distribution for the solar-like stars in the presented sample is in agreement with previous studies. Around 90% of the stars are located in the range of -5.1 $<$ log $R'_{\rm HK}$ $>$ -4.2, while 8% are very inactive and 3 % are very active. Within the stars in the intermediate active group there is a shift towards higher activity compared to studies from Henry et al. (1996) and Gray et al. (2003, 2006). This might be caused by a bias towards higher rotational velocities for some of the observed stars.

The rotation-activity relation found in this sample is in agreement with the data presented by Noyes (1984). For those stars with $B-V < 0.44$, the increase in the measured activity for faster rotation and the maximum activity are smaller than in the late F- and K-type stars. This effect is caused by the decreasing dynamo efficiency due to the disappearance of the outer convection zone.

The measurement of the chromospheric activity with the template method allowed for the first time to study the growing efficiency of the solar-type dynamo in the late A-type stars.

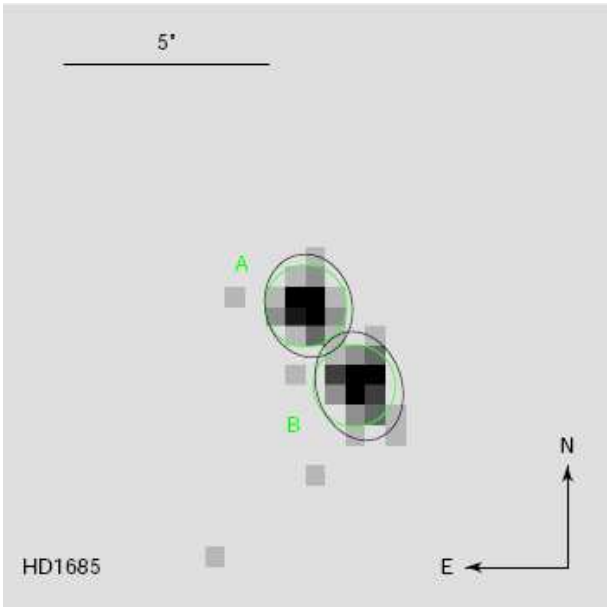

Figure 5.1: Chandra ACIS image of HD 1685 (Stelzer et al. 2005). A is the B-type stars and B is the late-type companion.

5.2 Outlook

Two different approaches have been followed to study the activity of stars in the range from A- to K-type stars. The presented results give insight in the activity phenomena near the onset of the solar-type dynamo, but there are a number of additional ways to further investigate this topic. In the following suggestions are given how the presented studies can be continued.

X-ray observations

The Chandra X-ray Observatory offers the possibility to identify hidden companions at the sample of X-ray emitting A-type stars. With the high spatial resolution provided by Chandra, binary systems with a separation of 1 arcsecond can be resolved. At a distance of 100 - 200 pc where most of the X-ray emitting A-type stars are located, this corresponds to a separation of less than 200 AU. According to studies by Close et al. (1990), the maximum separation of visual binaries in the solar neighborhood is larger. This leads to the conclusion that such systems are not unlikely to be bound.

Stelzer et al. (2003, 2005) observed late B- and early A-type binary stars to search for X-ray emission from the separated components. They found that allmost all late-type companions are X-ray emitters, but additionally 7 out of 11 B-type stars

have been detected in X-ray, too. An example of a binary system in which both stars are X-ray sources is shown in Figure 5.1. Therefore, these stars must either have an additional unresolved companion or be the observed X-ray source themself.

As the data presented by Stelzer et al. (2003, 2005) showed, follow-up observations of the ROSAT sources with Chandra offer the possibility to identify those sources which are positionally related to a hidden companion and those which can be associated with the A-type star. Further insight can be gained from the lightcurves of the sources, which might indicate the presence of a companion through flare-like variations.

Infrared observations

An additional wavelength range to search for hidden companions is the infrared. In this spectral region the difference in luminosity between the A-type stars and the companion is smaller than in the optical, leading to an increased chance to detect the late-type star.

Stelzer et al. (2005) showed observations of a known binary system containing a B9 and a K stars. The infrared spectrum of the B9 star HD 32964 in the H band does not only show the expected hydrogen features, but also includes various lines which are seen in spectra from mid K-type stars. With a slit width of $\sim$2 arcseconds and a separation of 1.6 arcseconds, these lines can possibly be contributed to the known companion. On the other hand, a hidden companion would contribute to the spectrum of the more massive star in a similar way, leading to the conclusion that this technique works in principle.

Speckle interferometry

With a spatial resolution down to the subarcsecond range, the speckle interferometry is a powerfull tool to identify close binary systems. At the distance of the most of the A-type stars a separation of 0.1 arcseconds corresponds to $\sim$20 AU, which would separate even close binary systems. The drawback of speckle interferometry is because it is difficult to observe faint objects. This technique depends on short integral times to reduce the effects of atmospheric motions. To decrease the difference in luminosity, the referred spectral range for this kind of observations would be the near infrared.

Long term observations of magnetic fields

The search for magnetic fields in X-ray emitting A-type stars was limited to 13 stars. On the list of promising targets, there are around 70 additional stars which can be tested for the presence of a magnetic field. Since the FORS1 instrument is mounted on one of the VLT telescopes and the pressure factor is obviously very high on this telescope, it is reasonable to sort out the unresolved binary system by studies based on the methods described above before continuing the magnetic field measurements.

The measurements for the stars presented in Chapter 3 can be improved by several observations over the rotation period of the stars. Since the magnetic field may be tilted towards the rotational axis, the measured strength of the longitudinal field varies according to the rotational phase. Therefore, the significance of a magnetic field detection can be improved by repeated observations.

Chromospheric activity

The measurement of the Ca II H&K activity in rapidly rotating stars showed the decrease of chromospheric activity in the early F- and late A-type stars. Due to the limited number of template stars, which have to be inactive and slow rotators, the fraction of stars measured with the template method was about 50%. This number can be increased significantly if additional templates can be found. As Figure 2 in Chapter 4 shows, the main-sequence stars in the range of $B - V < 0.3$ are are sparsely covered with template measurements. The reason for this is the fact that slow rotators in this color range are rare. In contrast to the solar-like late F to G stars, these objects are not slowed down by magnetic braking. This problem can be solved by finding a rapidly rotating star which is seen pole-on. With an increased number of templates in the range of late A- to early F-type stars, it would be possible to observe the onset of the dynamo in greater detail.

Another interesting aspect of the template method is the possibility to study the Vaughan-Preston gap (Vaughan & Preston 1980), which describes an deficit in the intermediate active solar-like stars. Several theories have been proposed to explain this phenomenon. Since the chromospheric activity is related to the stellar age, a gap in the activity distribution for a given sample could be caused by a fluctuation in the stellar birth rate

(Hartmann et al. 1984). Durney et al. (1981) suggested that the Vaughan-Preston gap can be due either to a rapid spindown at some point of stellar evolution, in such a way that there is a certain range of rotation period which is rarer than the rest, or to an abrupt change of the efficiency of the dynamo for a given rotation period.

With the new template method, it is possible to measure the activity with a different approach than the Mount Wilson method, yet the results are consistent with those obtained in previous surveys. Measurements of the activity of a sample from a previous study using the template method offer the opportunity to test wether the Vaughan-Preston gap is caused by rotational effects.

References

Babel, J. & Montmerle, T. 1997, A&A, 323, 121

Close, L. M., Richer, H. B., & Crabtree, D. R. 1990, AJ, 100, 1968

Czesla, S. & Schmitt, J. H. H. M. 2007, A&A, 465, 493

Durney, B. R., Mihalas, D., & Robinson, R. D. 1981, PASP, 93, 537

Gray, R. O., Corbally, C. J., Garrison, R. F., et al. 2006, AJ, 132, 161

Gray, R. O., Corbally, C. J., Garrison, R. F., et al. 2003, in Bulletin of the American Astronomical Society, Vol. 35, Bulletin of the American Astronomical Society, 1273–+

Hartmann, L., Soderblom, D. R., Noyes, R. W., Burnham, N., & Vaughan, A. H. 1984, ApJ, 276, 254

Henry, T. J., Soderblom, D. R., Donahue, R. A., & Baliunas, S. L. 1996, AJ, 111, 439

Hoffleit, D. & Warren, Jr., W. H. 1995, VizieR Online Data Catalog, 5050, 0

Noyes, R. W. 1984, Advances in Space Research, 4, 151

Stelzer, B., Huélamo, N., Hubrig, S., et al. 2005, in ESA Special Publication, Vol. 560, 13th Cambridge Workshop on Cool Stars, Stellar Systems and the Sun, ed. F. Favata & et al., 213–+

Stelzer, B., Huélamo, N., Hubrig, S., Zinnecker, H., & Micela, G. 2003, A&A, 407, 1067

Vaughan, A. H. & Preston, G. W. 1980, PASP, 92, 385

Acknowledgements

I would like to thank a number of people for their contributions to this work and for making the time of my PhD unforgettable. Since the people I would like to thank are german native speakers, I switch back to german.

An dem Gelingen dieser im Laufe der letzten Jahre entstandenen Arbeit sind viele Personen bewusst oder unbewusst beteiligt gewesen. Für ihre Hilfsbereitschaft und ihr Entgegenkommen möchte ich mich an dieser Stelle bedanken.

Ich beginne mit Prof. Jürgen Schmitt, der sich für Fragen und klärende Gespräche immer viel Zeit genommen hat. Durch die Auswahl dieses interessanten Themas und seinen wissenschaftlichen Rat ermöglicht er es mir, mich zu entfalten und von seinen Erfahrungen zu profitieren. Dafür möchte ich ihm besonders danken.

Ein spezieller Dank geht an Swetlana Hubrig und Ansgar Reiners, die mir nicht nur bei meinen Verffentlichungen wertvolle Untersttzung gewhrt haben, sondern auch die Reisen im Rahmen meiner Arbeit mit Rat und Tat untersttzten.

Desweiteren danke ich Birgit Fuhrmeister und Jan Robrade für die vielen Hilfestellungen, Anregungen und kritischen Kommentare, die sie mir gegeben haben.

Ein herzliches Dankeschön geht an die gesamte Arbeitsgruppe, namentlich Christoph Alexander Wawrzyn, Sascha Gehrke, Stefan Czesla, Klaus Huber, Moritz Günther, Caroline Liefke, Jan-Uwe Ness, Christian Schneider und Uwe Wolter, die mit Rat, Tat und einer wundervollen Arbeitsatmosphäre ihren Teil zu dieser Arbeit beigetragen hat.

Und natürlich gilt mein Dank meiner Familie für ihre die uneingeschränkte Unterstützung, die es mir ermöglichte, meinen Weg zu finden.

Zu guter Letzt danke ich der Deutschen Forschungsgemeinschaft für ihre Förderung unter der Nummer DFG SCHM 1032/22.